Fostering Tropical Cyclone research and applications with Synthetic Aperture Radar

Alexis Mouche[a], Arthur Avenas[b], Paul Chang[f], Bertrand Chapron[a], Théo Cévaër[h], Clément Combot[l], Joseph Courtney[q], Quentin Febvre[a], Ralph C. Foster[m], Antoine Grouazel[a], Masahiro Hayashi[h], Takeshi Horinouchi[l,r], Yasutaka Ikuta[h], Osamu Isoguchi[p], Christopher Jackson[k], Zorana Jelenak[n], John A. Knaff[g], Sébastien Langlade[o], Jean-Renaud Miadana[h], Frédéric Nouguier[a], Masato Ohki[i], Clément Pouplin[s], Tyler W. Ruff[e], Charles R. Sampson[d], Joseph Sapp[e,f], Udai Shimada[h,r], Takeo Tadono[i], Taiga Tsukada[j], Léo Vinour[l]

[a]IFREMER, Univ. Brest, CNRS, IRD, Laboratoire d'Oceanographie Physique et Spatiale (LOPS), Brest, France.
[b]European Space Research Institute (ESA-ESRIN), Frascati, Italy.
[c]OceanScope, 38, Rue Jim Sevellec, 29200 Brest, France.
[d]Navy Research Laboratory, Monterey, USA.
[e]Global Science & Technology (GST), Inc., Greenbelt, MD 20770 USA.
[f]National Oceanic and Atmospheric Administration (NOAA)/National Environmental Satellite, Data, and Information Service (NESDIS) Center for Satellite Applications and Research (STAR), College Park, MD 20740 USA.
[g]National Oceanic and Atmospheric Administration (NOAA) Center for Satellite Applications and Research, Fort Collins, CO, USA.
[h]Meteorological Research Institute, Japan Meteorological Agency, Tsukuba, Japan.
[i]Earth Observation Research Center (EORC), Japan Aerospace Exploration Agency (JAXA), Japan.
[j]Cooperative Institute for Research in the Atmosphere (CIRA), Colorado State University, Fort Collins, CO. USA.
[k]Global Ocean Associates, Alexandria, VA, USA.
[l]Faculty of Environmental Earth Science, Hokkaido University, Sapporo, Hokkaido, Japan.
[m]Applied Physics Laboratory, University of Washington, Seattle, WA.
[n]University Corporation for Atmospheric Research (UCAR) / Cooperative Programs for the Advancement of Earth System Science (CPAESS), 5830 University Research Ct, College Park, MD 20740, USA.
[o]Tropical Cyclone/Regional Specialized Meteorological Center, Météo France, La Réunion, France.
[p]Remote Sensing Technology Center of Japan, JAXA Tsukuba Space Center, Tsukuba, Japan.
[q]Bureau of Meteorology (BoM), Perth Australia.
[r]Typhoon Science and Technology Research Center, Yokohama National University, Yokohama, Kanagawa, Japan.
[s]France Energies Marines (FEM), Plouzané, France.

Abstract

In the past decade, the Sentinel-1 (S1) mission has proven to be invaluable for monitoring tropical cyclones (TCs) and conducting associated research. C-band S1 dual-polarization Synthetic Aperture Radar (SAR) have been instrumental in refining wind retrieval algorithms, especially for major category TCs. Systematic comparisons with airborne multi-frequency radiometer measurements confirm the unique ability of SAR to provide synoptic high-resolution TC characteristics, including key parameters such as such as the wind radii including the radius of maximum wind. Now integrated into operational forecasting centers, access to near real-time SAR data availability shall help improve forecasts. S1 data have also been shown to be a reference for interpreting and calibrating other satellite, in-situ measurements and algorithms. High-resolution synoptic SAR observations further enable significant advances in revealing links between the TC structure and its dynamics, inviting to more precisely infer tropical cyclone (TC) boundary layer properties, TC-generated waves, and interactions with the upper ocean. The recent increase in SAR acquisitions from multiple C-band SAR missions, combined with other observational data and numerical models, opens exciting opportunities to develop robust data-driven approaches. These advances shall support a better representation of TCs in digital twin frameworks by integrating future SAR missions, ultimately leading to more accurate predictions and a deeper understanding of these complex weather systems.

Keywords: Synthetic Aperture Radar, tropical cyclones, research, operational applications

---

Highlights

- Sentinel-1 acquisition strategy contributes significantly to the algorithm developments and improved TC monitoring.
- SAR wind products now contribute to the analysis and forecasting of TCs in operational centers.
- The growing SAR databases contribute to reveal links between the TC structure and its dynamics within the coupled ocean-atmosphere boundary layer.
- More robust data-driven approaches can be explored to support digital twin developments targeting TC events

1. Introduction

The first 10 years of the Sentinel-1 mission coincided with the successful launch of the Sentinel-1 C, the third satellite of the Copernicus series designed to provide consistent, high-resolution data for environmental monitoring. Each Sentinel-1 mission carries a synthetic aperture radar (SAR) sensor that uses C-band radar electromagnetic waves to produce detailed observations of the Earth's surface, regardless of weather conditions or time of day (Torres et al., 2012). Since the first C-band SAR images were acquired over tropical cyclones (TCs) (Vachon et al., 1999), these observations attracted the attention of the TC community (Katsaros et al., 2000b). SAR is recognized by many to be the only satellite sensor capable of quantitatively providing fine-scale, wide-swath information of the sea surface and ocean-atmosphere boundary layer processes under extreme conditions. SAR information provides "views from below" that complement more conventional “views from above” obtained with geostationary (GEO) observations. SAR data further enter a general context for both observational and numerical capabilities. Operational TC ocean surface wind field characteristics are continuously evolving in quality with improvements in the temporal coverage of medium-resolution low Earth orbiting satellite measurements (Knaff et al., 2021). Large-eddy numerical simulations are now reaching SAR spatial scales and new-hybrid machine learning physics-based modeling framework are emerging. An added benefit is that starting with Sentinel-1A (launched in 2014), all European SAR instruments of the Sentinel-1 series will continue to operate C-band co- and cross-polarized radars, and will stay freely and easily available. Prior to the Sentinel effort, SAR datasets were both expensive and costly to analyze.

Accordingly, the first 10 years of the Sentinel-1 mission opened a new era in how SAR data are used for monitoring extreme events. The long-term perspective motivates targeted science programs, including a specific campaign dedicated to TC monitoring with Sentinel-1 (Mouche et al., 2017). This initiative, still ongoing at European Space Angency (ESA), has certainly been a turning point, fostering many activities to more systematically exploit SAR observations acquired over TCs. ESA demonstration service and NOAA operational service also allowed the near-real-time availability of SAR-based TC wind speed imagery and TC fixes (Jackson et al., 2021). In late 2020, the SAR products were then implemented and evaluated at operational centers, becoming an element used by forecasters. Today, SAR observations are part of the mix of available satellite medium to low resolution passive and active microwave sensors to enhance TC monitoring for both scientific and operational applications. When developing algorithms to infer geophysical parameters from the signal, a key aspect is to exploit dual channel co- and cross-polarized high-resolution SAR scenes due to their differing sensitivities to very intense surface wind conditions (Zhang and Perrie, 2012a; Mouche et al., 2019). Freely available Level 1 data from Sentinel-1 have not only spurred new developments, they also enabled comparisons with in situ observations to test, revise, and compare retrieval algorithms. All this effort leads to significant improvements in the quality of both Level-1 and Level-2 SAR data.

In this paper, our objective is to present and review some of the state-of-the-art developments presently achieved. Most will apply to future sensors such as Sentinel-1C and the soon-to-follow Sentinel-1D. Developments have also been transferred to the Radarsat Constellation Mission (RCM), triggering a game-changing perspective to sample the dynamical evolution of

TCs. Retrieval algorithms will serve to prepare for the coming next-generation SAR satellites (ROSE-L, ALOS-4, Harmony). Accompanying promising data-driven methodologies, and more specifically targeting the improved realism of TC intensification in numerical simulations, SAR observations appear unique for providing high-quality validation and training data sets, with quantitative synoptic ocean-atmosphere high-resolution information available in the different ocean basins.

2. Paper structure

The paper is structured into three distinct parts on SAR measurements (section 3), SAR applications (section 4), and SAR observations perspectives (section 5), before concluding (section 6).

The first part, mostly dedicated to non-SAR experts, provides background on the SAR principle (section 3.1.1), the C-band SAR missions (section 3.2), and a presentation of the method to derive ocean surface wind speed estimates (section 3.3.1). This part includes technical consideration and recommendations regarding modes, polarization and acquisition for TC monitoring with SAR for space agencies (section 3.1.2). Products taylored to the TC community are also described (section 3.3.2). A presentation of the TC database gathered over the past decade concludes this part (section 3.4).

The second part focuses on two components of SAR-based applications. Section 4.1 presents how SAR has been used by the forecaster community in the TC centers for operational applications, such as the issuance of warning bulletins during storm events (sections 4.1.1-4.1.4). Benefits and limitations of SAR observations and products are then discussed. This provides useful insights into the strategy and workflow employed in the TC centers, as well as feedbacks that can be used as guidance for future algorithm developments to improve the different products. Section 4.2 highlights various scientific studies. It emphasizes how high-resolution SAR data refines our understanding of tropical cyclone wind structures and aids algorithm development for other sensors(section 4.2.1). The studies explore key vortex parameters, such as the wind radius in the inner core, to examine vortex-ocean interactions. SAR data is shown to enhance the understanding of TC wave generation (section 4.2.2), TC-induced ocean wakes (section 4.2.3), and boundary layer properties (section 4.2.4). Finally, it demonstrates the use of high-frequency SAR observations to analyze TC dynamics (section 4.2.5).

The third part (section 5) mostly discusses new perspectives. Based on the state of the art developments and feedback collected from users (both scientific and operational), this section proposes several paths to strengthen, improve, and extend the product quality, section 5.1. This shall be of particular interest to SAR experts involved in algorithm development. And finally, section 5.2 reviews forthcoming SAR missions that will contribute significantly to TC monitoring in the future, section 5.2.

3. Synthetic Aperture Radar and Tropical Cyclones

SAR observations have a long history of observing TCs. However, we first present SAR measurement principles, observation strategy, and requirements for TC monitoring for the reader's benefit. Then, we recall the key elements that led to the systematic retrieval of TC winds and associated parameters now used in operational centers. This section concludes with a review of the existing products and the current status of the database.

3.1. General background

3.1.1. SAR measurement principles

A static radar system operates by emitting electromagnetic waves that propagate through the atmosphere, interact with the surface or objects, and then are reflected back to the radar receiver. Received signals depend on the emitted and received wave's electric field properties such as incident angle, polarization and wavelength. Space agencies generally process the recorded data (Level-0) up to two different Level-1: SLC (Single Look Complex, including phase and amplitude of the signal without any projection) and GRD (Ground Range Detetected, including the amplitude of the signal and projection on the ground). Operating in the microwave domain, SAR systems can measure the backscattered signal at day and night and, depending on the emitted wavelength, are expected to be insensitive to clouds and rain (light to moderate). Three decades ago, focusing on four different C-band Radarsat-1 acquisitions over TC, Katsaros et al. (2000a) reported spectacular distinctive signatures. Today, most of the SAR observations of TCs over ocean are obtained with C-band (about 5.35 GHz, corresponding to about 5 cm wavelength) systems from Sentinel-1, Radarsat-2, or Radarsat Constellation missions, acquiring data in wide-swath mode with incidence angles ranging from about 19 to 55 degrees, in both co- and cross- polarization. When signals are received in the same orientation than the emitted wave it is termed co-polarization: VV or HH. When they are received in the orthogonal orientation with respect to the emitted, it is termed cross-polarization: VH or HV. TCs are characterized by extreme and strongly varying wind speeds and severe sea state conditions. The backscatter signals are then expected to reach high values. Heavy rain and intense vertical displacements of air parcels are also expected to occur, making the task of disentangling the various contributing factors significantly more challenging than in typical

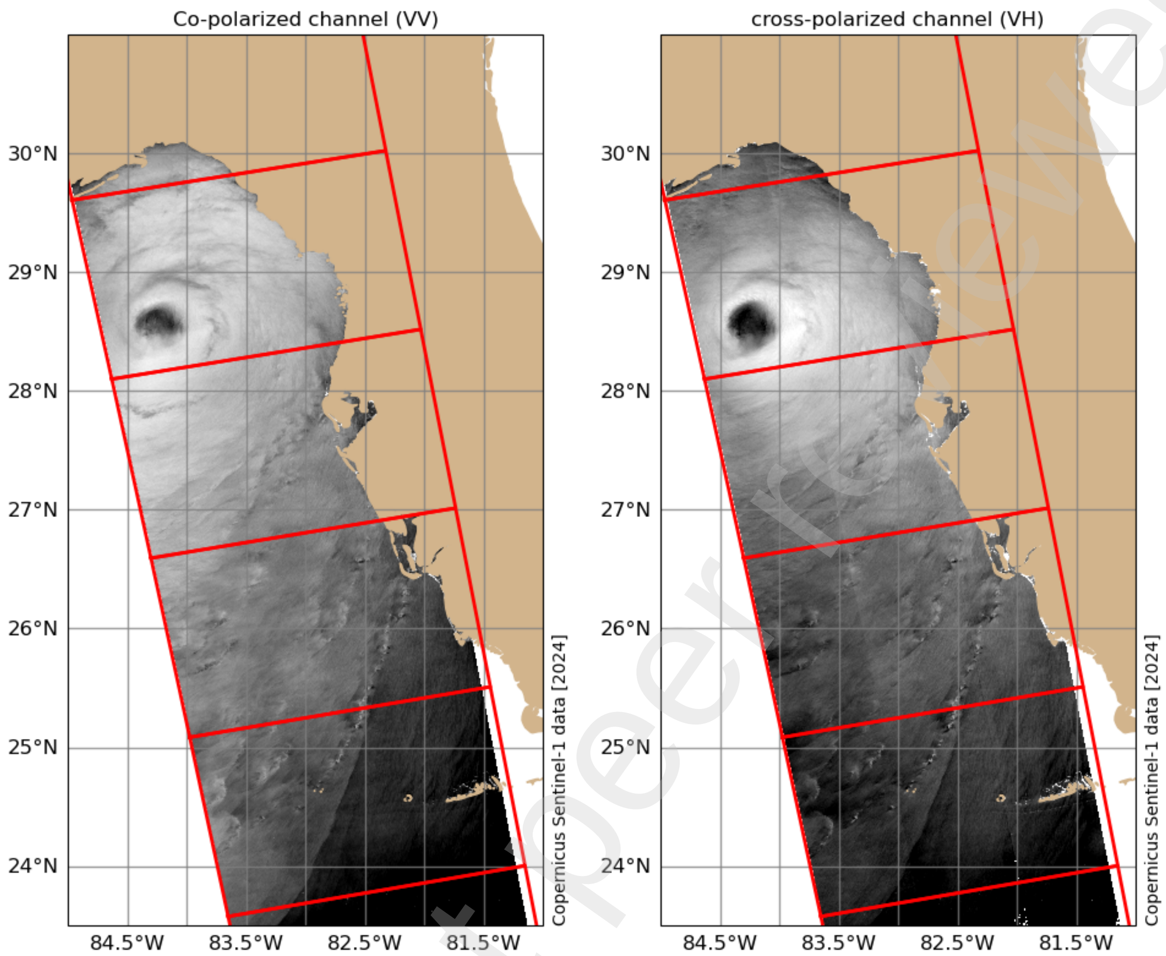

Fig. 1. Two views of Hurricane Helene acquired on September 26, 2024 with Sentinel-1 co- (VV, left panel) and cross- (VH, right panel) polarized channels from 23:35:52 to 23:37:57 UTC. The cyclone was a Category 4 hurricane on the Saffir-Simpson scale at this time according to the National Hurricane Center. Red polygons delineate the slice limits of concatenated Level-1 GRD products used to generate this synoptic view of the storm.

homogeneous conditions. Because localized events are often well above background conditions, they all have a signature in the Normalized Radar Cross Section (NRCS) but possibly detected at different resolutions. Fig. 1 is an example of Sentinel-1 acquisitions over Hurricane Helene on September 26, 2024 to illustrate the typical signature of a mature TC obtained at C-band in VV (left) and VH (right) polarization channels. Usually, the wind signature is analyzed at the kilometer scale (500 m to 3 km) through the mean value of the NRCS. The signature of the ocean waves and the secondary circulation in the atmospheric boundary layer is encoded in the radar backscattered modulation and observed at higher resolution (resp. tens of meters and hundreds of meters). The rain is very specific, as the area of intense rain can be large (more than 3x3km) with an irregular fine-scale outline. In addition, at C-band, the rain signature in the NRCS is complex as it arises from multiple contributions: scattering and attenuation by hydrometeors in the atmosphere, as well as modification of the roughness of the sea surface through interactions between the impinging rain droplets and the surface (Melsheimer et al., 1998; Alpers et al., 2016). Figure 2 illustrates the impact of rain on the NRCS in the case of Hurricane Helene (same acquisition as Fig. 1) when compared to the differential base reflectivity measured by a ground-based radar from the NEXRAD network. The maximum base reflectivity is strongly correlated with local variations in NRCS. In this case, the most intense rainfall (differential base reflectivity greater than 35 dBZ corresponding to orange contours on roughness maps) mostly corresponds to local signal attenuation in both VV and VH channels. Notably, the signature is different between the two polarization channels. Here, the closest rainband to the shore seems to impact the VV polarization more than the VH polarization.

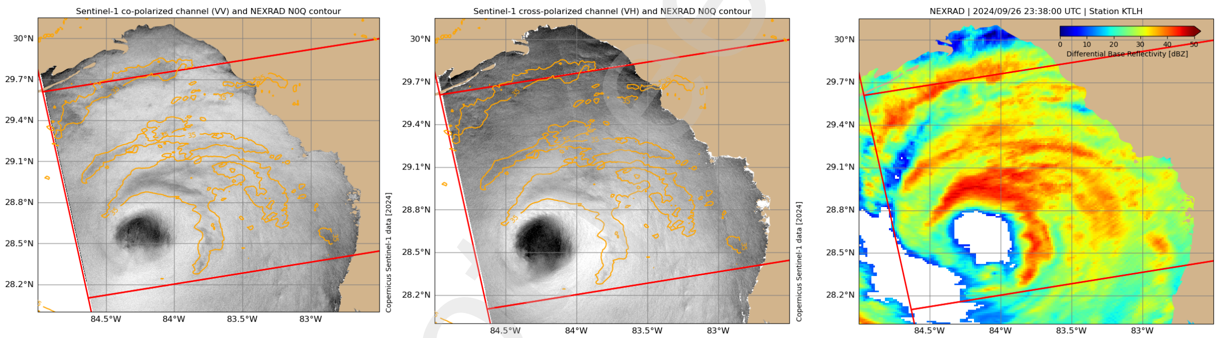

Fig. 2. Left and center panels: Same as Fig. 1, but zoomed over the TC eye. Overplotted are contours (orange) of differential base reflectivity corresponding to 35 dBZ. Right : Differential base reflectivity from NEXRAD station KTLH (Tallahassee International Airport).

3.1.2. SAR Observation strategy and requirements for Tropical Cyclone monitoring

SAR systems are deployed on low Earth orbit, sun-synchronous satellites. In the case of the Sentinel-1 constellation, the two platforms operate at a mean altitude of 693 km and have a 12-day repeat cycle. Because Sentinel-1A and Sentinel-1B have been placed on the same orbit but with a phase shift of 180°, the repeat cycle of the constellation is 6 days. When using the wide swath mode without any constraints on the incidence angle used for the observations, the revisit time is improved. For example, a point located at 35°N in the mediterranean sea where Sentinel-1 acquisitions in wide swath mode are maximized, there will have 2 to 4 acquisitions in 12 days (repeat cycle).

In contrast to other spaceborne microwave sensors such as scatterometers, radiometers or altimeters, SAR systems have a duty cycle preventing continuous acquisitions along the orbit. Duty cycle refers to the ratio of time during which the radar actively transmits signals to the total operational time of a cycle. The prescribed duty cycle is critical for spaceborne SAR systems as it regulates energy consumption, thermal dissipation, and adaptation to orbital constraints with respect to the targeted applications. Managing the duty cycle is key to the durability and efficiency of radar systems in the space environment, where energy and thermal resources are strictly limited. Sentinel-1 duty cycle is about 25 min/orbit (about 1/4 of the orbit period), depending on the season.

Also in contrast to other microwave sensors, SAR systems operate through distinct acquisition modes, each offering different coverage and resolution suited to a broad range of applications. These modes are mutually exclusive and have varying impacts on the satellite's duty cycle, requiring careful management of observation strategies. Typically, this is done using a baseline mission acquisition plan, with specific additional requests handled by a mission acquisition team. In the case of Sentinel-1, the baseline mission follows a seasonal schedule to support critical applications, such as sea-ice monitoring, and has been adjusted to accommodate periods when only one of the two sensors was available. In practice, Sentinel-1 acquisition plans, covering 20-day periods, are regularly issued about two repeat cycles in advance.

For TC monitoring, the targeted system is dynamic, but both its trajectory and intensity can be tentatively forecasted. This additional constraint requires dedicated management of the acquisition plan to assess the impact of each new TC observation on the system. Since TC genesis and evolution cannot be predicted well in advance, a tailored acquisition strategy has been developed. The current methodology builds upon the approach first implemented in the Radarsat mission's Hurricane Watch program (Banal et al., 2007), following pioneering tests in 1998 (Vachon et al., 1999). The overall strategy remains similar across the three main SAR missions and relies on TC track forecasts issued post-genesis to optimally plan SAR acquisitions, with a focus on modes best suited for wind speed estimation while accommodating system constraints and other scientific applications. In the case of Sentinel-1, the mission planning team updates the Sentinel-1 acquisition plan for TC observation during their working hours (Monday to Friday, 08:00-17:00 CEST/MEZ). The preferred Sentinel-1 acquisition mode is EW (for extended Wide) to maximize the coverage but IW (for Interferometric Wide Swath) is also used to allow for merging with an existing IW acquisition resulting from other Sentinel-1 requirements or in coastal areas. Targeted Sentinel-1 data takes are 80 sec in duration, centered over forecast tracks and flagged to allow a fast processing

(< 3 hours). Sentinel-1 mission planning relies on 5-day TC forecasts from the European Centre for Medium-Range Weather Forecasts (ECMWF).

For optimal results, the wide-swath acquisitions are conducted in dual polarization (co- and cross- polarization channels) VV polarization is preferred over HH due to its improved sensitivity in these applications. The wide-swath mode is essential to capture the TC center and broader storm structure, as winds reaching 34 knots (kt; 1 kt = 0.51444 m/s) may extend 400-500 km from the storm center. To date, high resolution is not used for ocean surface wind retrieval as the NRCS is typically calculated at approximately 1 km resolution. For example, Sentinel-1 Level-1 GRDH (here H stands for the high resolution version of S1 Level-1 GRD product) products in IW and EW modes offer a resolution of about 20x22m and 50x50m, respectively, while RCM (designed as a medium resolution mission, primarily dedicated to regular monitoring of broad geographic areas.) Level-1 products provide a resolution of about 100x100m (low resolution mode), both adequate for TC wind monitoring. However, for wave retrieval, resolution constraints may need to be stricter. A critical parameter here is the Noise Equivalent Sigma Zero (NESZ). Precise calibration of NESZ variations along range and azimuth is necessary for an accurate NRCS correction, prior to wind speed estimation. In 2018 (2018/03/13) , ESA updated the processor version (2.90) and enhanced the accuracy of the NESZ annotated in the Level-1 products, leading to a significant improvement in data quality. However for all SAR missions quality issues persist with jump between subswaths, evident in a "stair-step" effect. Other effects within each subswath can also impact data analysis. For example, in TOPS (for Terrain Observation by Progressive Scans) mode acquisitions, noise variations in the azimuth direction during the antenna sweep can also reduce data quality.

Figure 3 illustrates for each constellation contributing to the TC monitoring the diversity in sensors, acquisition modes, and polarization configurations used to observe TCs with C-band SAR. This diversity results in varying signal quality (for example, NESZ differs between sensors and modes) and presents challenges to deliver a consistent homogeneous data set. However, as shown on Fig. 5 and discussed later in section 3.3, when observed almost simultaneously by three different C-band sensors, the wind estimates remain very consistent, illustrating the potential of a multi-platform approach to monitor TC, and at the same time provide homogeneous data for research and development.

3.2. Contributing C-band SAR missions for TC observations

SAR observations of TCs began with SEASAT, the first spaceborne SAR aboard the first satellite designed for remote sensing of Earth's oceans. Notably, during Hurricane Iva in 1978,

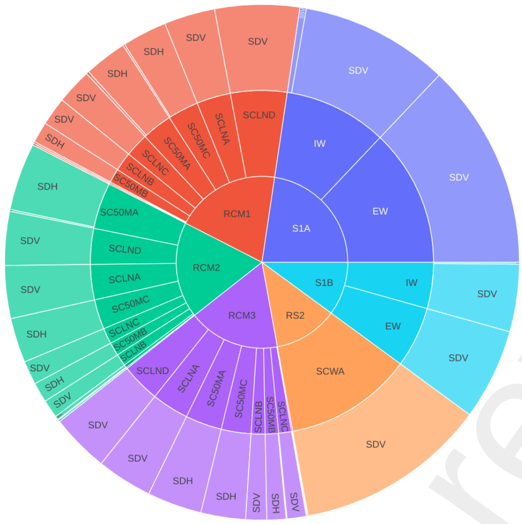

Fig. 3. SAR constellation contributing to the TC monitoring with sensor names (inner circle), acquisition modes (middle circle. Refer to missions product format description for details of each mode) and polarization configurations (outer circle. SDV means VV and VH, SDH means HH and HV, SSH means HH and SSV means VV) available.

SEASAT captured small-scale surface roughness caused by wind variability and signal attenuation due to intense rainfall, revealing two of the storm's spiral arms and its center (Fu and Holt, 1982). When analyzed at high resolution, Gonzalez et al. (1979) demonstrated that the modulations in the backscattered signal also traced ocean waves, potentially providing information on their wavelength and origin, applicable to TCs Gonzalez et al. (1982). After SEASAT, the development of C-band SAR systems has been continuously supported by the Canadian Space Agency (CSA) and the ESA. Today, these agencies provide the primary contributions to TC monitoring with SAR.

More systematic acquisitions began in 1999 with the Radarsat-1 C-band SAR mission, when the CSA initiated the "Hurricane Watch" project in collaboration with the U.S. National Oceanic and Atmospheric Administration (NOAA) and the Canadian Department of Fisheries and Oceans (DFO). Over time, this project evolved from archival data searches to real-time storm monitoring and dedicated observation planning, significantly reducing the reliance on serendipity in data collection. To a lesser extent, ESA also contributed with limited SAR acquisitions onboard Envisat satellite between 2002 and 2012. One of the key contributions of SAR/Envisat was its ability to provide co-located measurements from multiple sensors, enabling more comprehensive analyses. In addition, it allowed for the first examination of the Doppler signature of the sea surface associated with TC. Fig. 4 shows an example of simultaneous acquisitions made using the ASAR and MERIS sensors onboard Envisat.

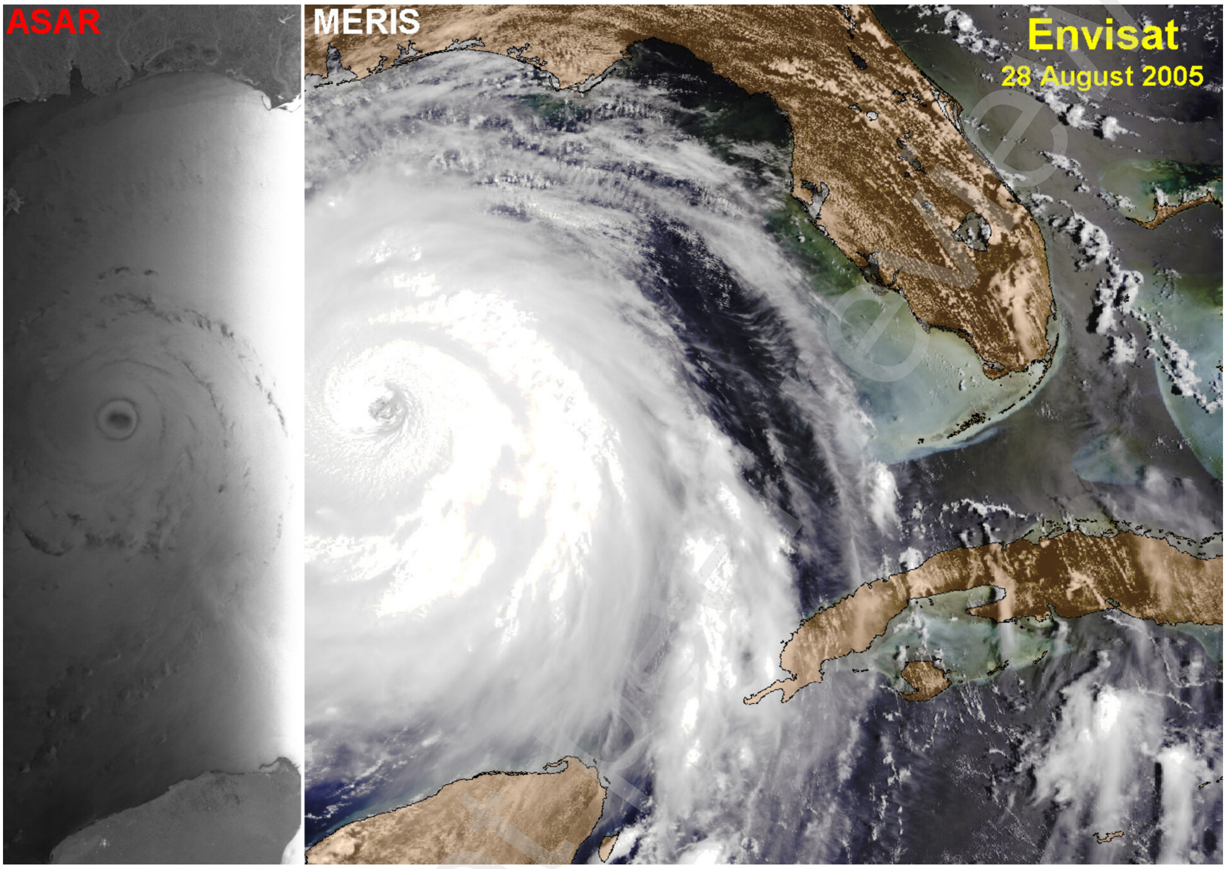

Fig. 4. Two separate views of Hurricane Katrina acquired 28 August 2005 from instruments aboard Envisat. The ASAR (for Advanced SAR) Wide Swath mode radar image of the sea surface shows how Katrina's wind fields are rippling the ocean. Beside it is the MERIS Reduced Resolution mode optical images showing characteristic swirling cloud patterns around the central eye, with the eye walls visible (ESA, 2005).

The launch of Radarsat-2 (RS2, a CSA and MDA collaboration) on December 14, 2007, marked a turning point in providing high-resolution estimates of ocean surface wind speeds during extreme events. CSA strategy to allow for systematic acquisitions in quad-polarization mode over buoys, with a very low noise-equivalent sigma zero (better than -32 dB), enabled detailed documentation of the cross-polarization channel's sensitivity to wind-induced surface roughness. This demonstrated its complementarity with the co-polarization channel. Although the signal-to-noise ratio is lower in cross-polarization compared to co-polarization, the backscattered signal in cross-polarization is less affected by incidence angle and wind direction, and more sensitive to wind speeds exceeding 15 m/s (Vachon and Wolfe, 2011). Although their study primarily focused on storms with intensities below hurricane level, Zhang and Perrie (2012b) highlighted the potential of the cross-polarization channel to estimate ocean surface wind speeds in TCs. They provided the first wind maps using this channel from wide-swath acquisitions for TCs. In general, monitoring TCs with SAR has greatly benefited from the Radarsat-2 mission, which continues to be a key contributor to the TC SAR data archive.

Sentinel-1A (S1A) and Sentinel-1B (S1B), launched in 2014 and 2016 respectively, are also equipped with the capability to measure in dual-polarization wide swath mode using both co- and cross-polarization channels. Following the Hurricane Watch initiative, ESA launched the Satellite Hurricane Observation Campaign (SHOC) in 2016. An example of Sentinel-1 acquisition over Hurricane Helene is illustrated in Figures 1 and 2. After the first edition of SHOC, a new algorithm to estimate wind speed using a combination of both co- and cross-polarization channels was introduced (Mouche et al., 2017) and ESA secured the SHOC activity up to now. Copernicus' free-of-charge data sharing policy represents a complete paradigm shift compared to RADARSAT-2 commercial data policy and significantly contributed to fostering new developments. This policy also includes systematic processing of data up to level-1 GRD and SLC products. Although SLC data is heavier than GRD, it enables exploration of new approaches that leverage both the intensity and phase of the signal, paving the way for future algorithm developments (see Section 5.1). While not yet operational, there have been ongoing efforts to retrieve ocean wave parameters from Sentinel-1 acquisitions over wide swaths Pleskachevsky et al. (2022). Additionally, a unique feature of Sentinel-1 is its dedicated Wave Mode, specifically designed to measure ocean surface wave spectra in the open ocean. These observations have been instrumental in characterizing swell generated within tropical storms intense wind zones and propagating across the ocean (Pouplin et al., 2024).

Since the launch of the Radar Constellation Mission (RCM) in June 2019, the constellation of C-band SAR missions available for TC monitoring has significantly expanded. Indeed, while it is the most recent, RCM has quickly become a major contributor to this TC monitoring system. Algorithms developed for Radarsat-2 and Sentinel-1 missions have been successfully adapted to RCM to provide ocean surface wind products.

In the last decade, there have been sporadic acquisitions over TCs with other C-band missions (e.g. Gaofen-3) directed at science applications. To date, they remain anecdotal (small number, limited availability). The recent launch of Sentinel-1C in December 2024, along with the forthcoming launch of Sentinel-1D in 2025, should also contribute to TC monitoring over the ocean using SAR. Several SAR missions are now in commissioning phase or in preparation and may reinforce this constellation (see section 5.2).

3.3. Tropical cyclones geophysical parameters retrieval and products

The wide swath acquisitions from the C-band SAR systems onboard RS2, S1, and the RCM missions are systematically obtained by Ifremer (system, product and database collectively referred to as CyclObs) and NOAA and then processed into harmonized (format and variables consistent regardless of the mission) Level-2 wind products. The Level-2 product portfolio includes a Level-2 wind speed product with wind speed estimates at kilometer scales (1km pixel spacing and 3 km resolution for CyclObs, 0.5 km and 3 km for NOAA) within the swath, and a dedicated analysis of the TC vortex to provide key parameters on the wind structure. Unlike the current operational Copernicus Level-2 products, when a datatake covering a storm has been sliced by the Level-1 SAR processor, the slices are concatenated to capture the entire storm in the Level-2 product. CyclObs aims to build an archive for scientific applications (algorithms and data-driven TC studies) without any operational purpose or commitment for near-real-time delivery. The database can be accessed and browsed at cyclobs.ifremer.fr. NOAA's efforts focus on near real-time processing and dissemination of TC wind speeds and profiles to support the TC forecasting community. The ESA counterpart for demonstrating the capabilities to process Sentinel-1 data in near-real time is CYMS (Cyclone Monitoring Service based on Sentinel-1).

Fig. 5 presents S1, RS2, and RCM wind estimates over Hurricane Lee on 08 Sept 2023 at 21 UTC obtained by NOAA processing chain. Each observed the storm over a span of about 2 minutes. The storm was estimated to be a Category-3 hurricane with sustained winds of > 120 mph (194 km/h). As observed, there is a great consistency between the three sensors demonstrating the potential of SAR constellations from different agencies to provide homogeneous wind products to the TC community. The bottom left panel displays the SAR wind values in the south-western quadrant as a function of distance from the center of the storm, with markers indicating $V_{\max}$, and the maximum radial extent of 34-, 50-, and 64-kt winds ($R34$, $R50$, $R64$). The wind values exhibit the classical shape of the wind profile within a TC with a sharp increase of wind speed in the TC eyewall followed by a smoother decrease in the outer core region.

3.3.1. Ocean surface wind estimates

To a first approximation, when atmospheric effects (e.g. rain) are neglected, over the ocean, the backscattered signal is driven by sea surface roughness. At kilometer scales, this roughness is driven by wind stress, with its variations interpreted as changes in ocean surface wind speed and direction. This principle forms the basis of algorithms that process radar cross-sections measured

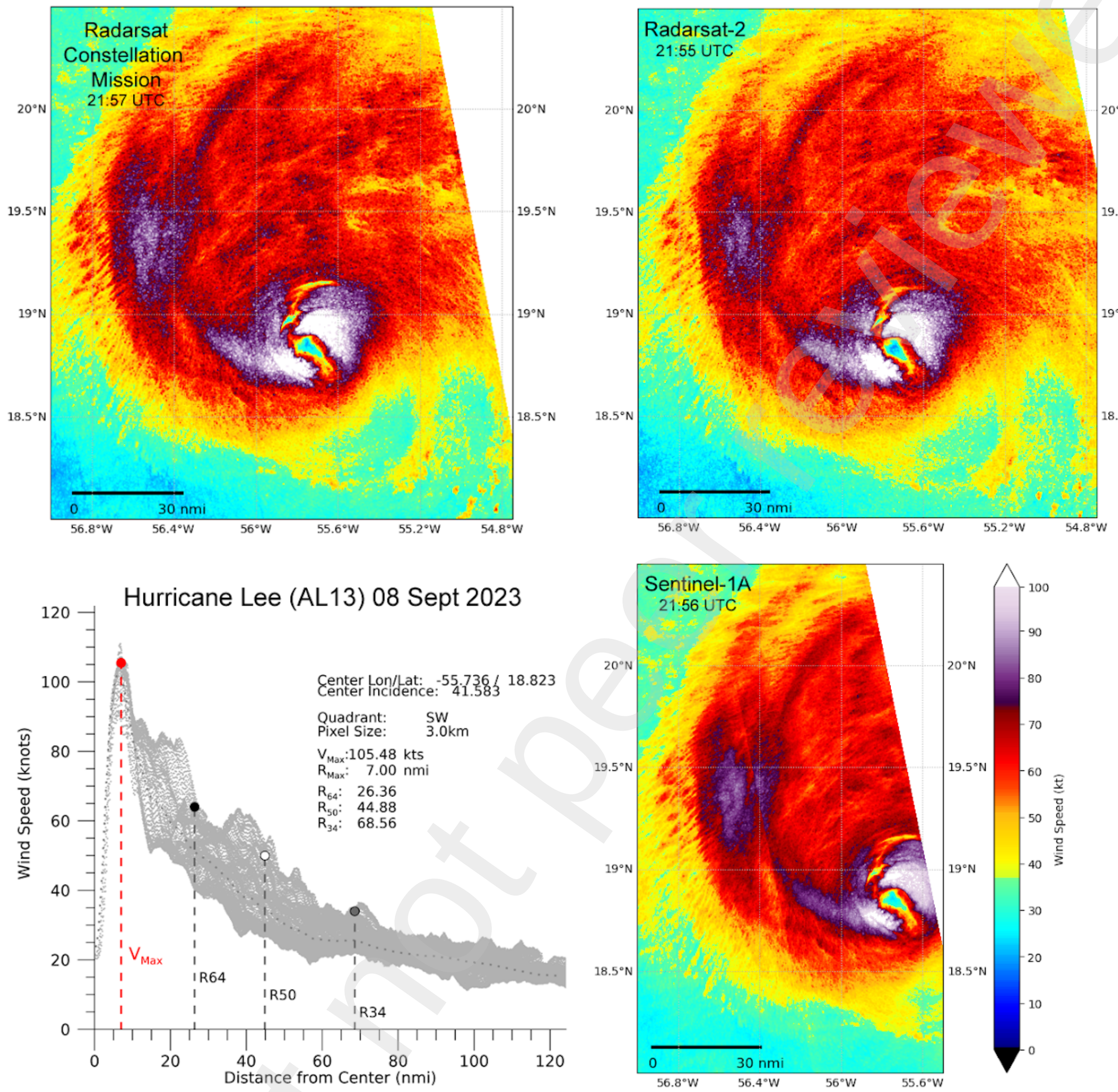

Fig. 5. Example of near-simultaneous acquisitions over Hurricane Lee (2023) with the three C-band SAR missions, RCM-2 (top left), RS2 (top right) and S1A (bottom left). Acquisitions are almost simultaneous with less than 3 minutes between them. Bottom left : wind values with respect to TC center location obtained in the south-western quadrant and associated TC parameters. Processings from NOAA.

by scatterometers (Stoffelen and Anderson, 1997) to derive ocean surface wind vectors. A key component of these methods is the Geophysical Model Function (GMF), which links the NRCS to ocean wind vectors relative to radar viewing angles. Over time, scatterometer measurements colocated with reference wind data have facilitated the development of various GMFs for radars operating in Ku- and C-Bands and in co-polarization. Still, a single NRCS measurement provides insufficient information to uniquely resolve both wind speed and direction. The inverse problem is under-determined. For scatterometer missions, this limitation is mitigated by solving the wind vector estimation problem within so-called wind vector cells that aggregate multiple radar measurements from different viewing angles and possibly additional non-local constraints on the wind flow based on atmospheric models. To date, the main limitation of scatterometers is the weak sensitivity of the signal in co-polarization to extreme winds.

For SAR systems, defining wind vector cells with a diverse set of viewing angles is not feasible due to the unique and fixed antenna on the satellite. One single viewing angle limits the capability to resolve both wind speed and direction from the NRCS. This limitation is generally addressed by estimating the wind direction before retrieving the wind speed and, in particular, by analyzing the high-resolution texture of the radar backscatter to infer wind orientation (Koch, 2004; Horstmann et al., 2013). Fan et al. (2020) showed the benefit of the cross-polarization channel to derive the wind orientation from the image texture in the case of intense tropical wind speeds. Another practical solution is to get the wind direction from an a priori solution given by an atmospheric model. To further constrain the inverse problem, one can also add other radar parameters available in the SAR measurements but this is on-going research (see discussion in section 5.1). Finally, the NRCS dependency to the wind direction is much weaker in cross-polarization than in co-polarization for strong winds (Horstmann et al., 2015). When neglected, the relationship between wind speed and NRCS is direct and the problem fully constrained. In addition, as shown by Mouche et al. (2019) the sensitivity to the wind speed in the extreme regimes is higher in cross-polarization. The dynamic range of this backscattered signal in cross-polarization, combined with its minimal dependence on wind direction, provides valuable new information.

However, Vachon and Wolfe (2011) also document that, over the ocean, cross-polarized radar backscatter is significantly lower— several orders of magnitude less than co-polarization backscatter. This makes cross-polarization highly sensitive to Noise Equivalent Sigma Zero. For example, at a wind speed of 10 m/s, the NRCS is about -30 dB in cross-polarization, whereas it is around -10 dB in VV and -11 dB in HH. This weak signal is thus challenging when it comes to geophysical parameter retrieval with this polarization channel. In the case of Sentinel-1, a typical NESZ value in IW mode is about -30 dB with discontinuity at sub-swath limits. If the noise is not properly removed, this is translated into the NRCS and then in the wind speed with possible artefacts when evaluating TC parameters. The quality of the annotated noise and value of the NESZ are two critical points to consider when designing future SAR missions targeting TC monitoring and more generally ocean applications. During extreme storm conditions, the NRCS in cross-polarization can increase up to -17 dB, enabling it to be used for wind speed retrieval. To harness the advantages of both channels, Mouche et al. (2017) proposed an approach merging the two.

The NOAA SAR service relies on the cross-polarization channel alone to provide near-real-time wind estimates, while the CyclObs database uses a combination of co- and cross-polarization channels to derive TC wind products. At the highest wind speeds, the two methods produce consistent results, as the cross-polarization channel predominantly influences the cost function during wind inversion. For CyclObs inversion scheme, the cost function is

$$\begin{aligned} J(u,v) &= \left[\frac{\sigma^0_{\rm co}(\theta) - \hat{\sigma^0}_{\rm co}(\theta, U, \Phi)}{\Delta\sigma^0_{\rm co}}\right]^2 \\ &+ \left[\frac{\sigma^0_{\rm cr}(\theta) - \hat{\sigma^0}_{\rm cr}(\theta, U, \Phi)}{\Delta\sigma^0_{\rm cr}}\right]^2 \\ &+ \left[\frac{u-\hat{u}}{\Delta u}\right]^2 + \left[\frac{v-\hat{v}}{\Delta v}\right]^2, \end{aligned} \tag{1}$$

where u and v are the ocean surface wind components in the radar image azimuth and range directions. U and Φ are the wind speed and direction. $\hat{\sigma^0}$ are NRCS simulated by a GMF given the wind direction and radar viewing angles. $\hat{u}$ and $\hat{v}$ are given by a background atmospheric model wind component (u_B and v_B) and expressed in the satellite image coordinate system. $\Delta v = \Delta u = 2$ and $\Delta\sigma^0$ depends on the signal to noise ratio.

SAR winds are validated primarily against wind speed measurements from the airborne Stepped Frequency Microwave Radiometer (SFMR) as it provides high resolution estimates of the ocean surface wind speed (Sapp et al., 2019). Figure 6 presents an example of colocation along the aircraft transects obtained on September 7, 2021 during Hurricane Larry. After taking into account for TC displacement during airplane flight, we observe a very high correlation between the radar backscattered signal (especially in VH; blue line on top left panel) and the SFMR wind speed (black line on bottom left panel) measurements. When radar signal is translated into wind speed (dark blue line on bottom left panel) it can be directly compared to SFMR measurement. An alternative is to rely on other satellite data such as L-band radiometers. However, if they provide much more collocated data than airplanes, they suffer from low resolution limitations (40 and 50 km resolution, respectively for SMOS and SMAP) for direct comparisons against SAR, in the inner-and near-core regions of the system (Avenas et al., 2023). Several promising avenues exist for

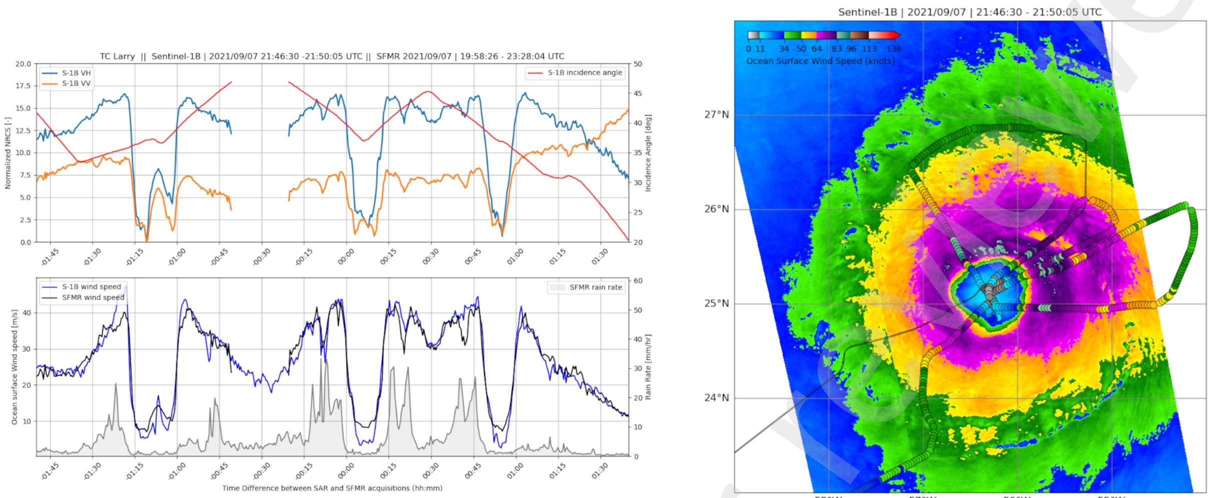

Fig. 6. Example of colocation and comparison between SFMR (ocean surface and rain rate) measurements and SAR wind speeds estimated from Sentinel-1B on September 7, 2021 during TC Larry.

improving the ocean surface wind speed algorithm and the presented wind products. Section 5.1 provides a brief review of existing efforts in the community and outlines potential avenues for future improvement.

3.3.2. TC wind structure parameters

To characterize TCs more effectively, most forecast centers maintain post-season quality controlled databases of location, intensity and structure for all TCs within their areas of responsibilty. These are commonly called "best tracks." The forecast centers then provide their best track data to NOAA's National Center for Environmental Information for inclusion in the International Best Track Archive for Climate Stewardship (IBTrACS; Knapp et al. (2010).), and from there the best tracks are made publicly available in a convenient spreadsheet. The best track wind structure in these databases is typically described in terms of the maximum radial extent of winds reaching some treshold (e.g. 34, 50, and 64 kt, and many times in four compass direction quadrants NE, SE, SW and NW). Intensity is defined in the U.S. as the maximum 1-minute (can be 10-minute in other TC forecast center. See section 4.1) sustained wind speed measured at 10 meters above the surface. This value serves as the basis for categorizing TC. To complement the wind radii and more precisely define the region of maximum wind intensity, the radius of maximum wind $R_{\max}$ is also included in the best track files. As reported by Rappaport et al. (2009), analysis of 34 kt wind radii relies on scatterometer measurements, satellite estimates (e.g., AMSU), aircraft observations, as well as occasional ship, buoy, and land-based measurements. Since then, other satellite missions, including L-band (SMOS, SMAP) and dual-frequency C-band radiometers (AMSR-2), have demonstrated their ability in describing the wind structure of the outer core (Reul et al., 2017; Meissner et al., 2017), including 34-, 50- and 64-kt wind radii (see section 4.1).

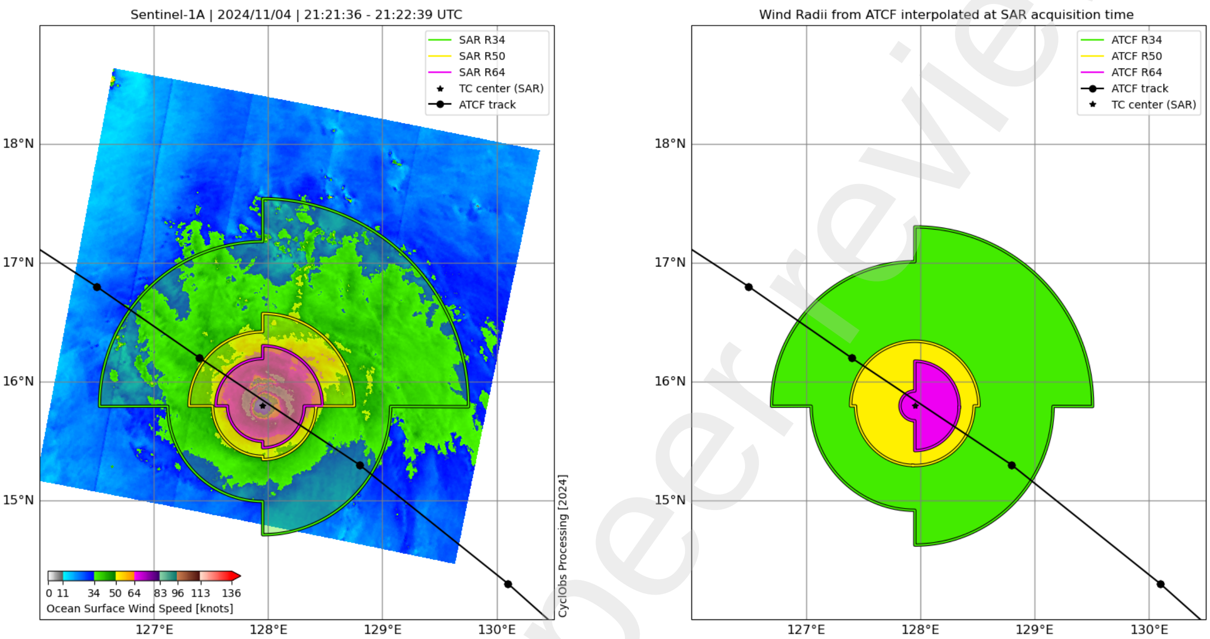

Fig. 7. Example of TC wind radii estimated for TC Yinxing on November 4, 2024, from Sentinel-1A Level-2 CyclObs wind products (left) and available in the ATCF tracks (right). For comparison purposes, ATCF values obtained at 18:00 and 00:00 are interpolated at the SAR acquisition time and plotted with respect to the TC center obtained from SAR.

Because the SAR instrument has the unique capability to probe large areas of the ocean surface at very high resolution O(150 m) , the SAR wind product can further help to provide independent estimates of the TC wind structure. In particular, SAR complement medium-resolution sensors such as scatterometers and radiometers to estimate radii. SAR is particularly useful in estimating R_{max} and both $R50$ and $R64$, all of which are commonly smaller than the resolution of the other sensors (scatterometer and radiometer) or fall within the range of wind speeds where saturation can occur.

The location of the TC center marks the initial step to estimate strucutre, as other variables are defined relative to the TC center. If the TC center cannot be identified within the image, the vortex structure parameters are not derived from the SAR acquisition. A summary of the algorithms developed for estimating TC wind structure parameters included in the CylcObs database is provided below and has been derived from Combot et al. (2020a) and Vinour et al. (2021) work.

- TC center : The center-finding procedure involves recursively computing the centroids of low-wind areas and identifying a stable (i.e., consistent across iterations) low-wind region near the maximum wind area. This approach assumes that the TC eye consistently exhibits significantly lower wind speeds compared to its surroundings, resulting in a distinctly identifiable eye. A first guess from the available storm track is used. A final step is to place the center in the middle of the eye by retrieving the eyewall shape and computing its centroid. Existing center-finding algorithms can suffer from inaccuracies of the initial center location guess by up to 50 km, in addition to asymmetries in the storm structure that can introduce additional complexities. These factors highlight the need for further improvements in these algorithms, possibly via machine learning. The four remaining parameters are computed across all quadrants and algorithms are performed within a TC-centered reference frame.

- $V_{\max}$ and $R_{\max}$: The algorithm operates iteratively beginning with an initial solution derived from the azimuthally averaged wind profile and refining it by analyzing the wind profile variations with respect to the azimuth angle.

- Wind Radii : The algorithm identifies the wind areas corresponding to 34, 50, and 64 kt. The radii are then placed along the outer boundary of these areas for each of the four quadrants. A critical aspect is the criteria to define those boundaries.

Several factors can influence the retrieval of TC wind structure parameters from SAR images. These include the cyclone's size relative to the satellite acquisition footprint, its position within the satellite acquisition frame, the distance to coast, the accuracy of the wind field retrieval algorithm, and the quality of the radar signal itself. In particular, these algorithms rely on an analysis of the radar signal heterogeneities (a method developed by Koch (2004) and optimized for rain by Zhao et al. (2021)) to filter out wind speed spikes caused by hydrometeors within the rainbands, thereby reducing the potential impact of rain. In the CyclObs database, together with the wind structure parameters, a quality flag is included as an output of the analysis to help non-SAR experts use the data.

Combot et al. (2020a) conducted the first in-depth analysis of these SAR-derived parameters including comparisons against the IBTrACS database. When compared to the best track, the correlation obtained for each of the three wind radii exceeds 0.85 and the normalized bias is minimal, approximately -3% for R_{34} and R_{50}, but rises to around 10% for R_{64}. Overall, the agreement is weaker for R_{64}, with its values typically below 100 km. This limitation likely reflects constraints in best track analysis when relying on low- to medium-resolution data. Such constraints also affect the R_{max} parameter with its values even lower (10-100 km), which exhibits the poorest agreement in comparisons. Supporting this idea, it is worth noting that when aircraft measurements are available the agreement between SAR and best track increases. To date, SAR is still a unique sensor in that it is able to provide R_{max} estimates from space for the entire globe.

3.4. *Status of the database*

The status of the SAR TC database has significantly evolved in time due to the life cycle of contributing missions, improvements processes to trigger data acquisition, and manage conflict with other applications than TC monitoring. Here we focus on CyclObs status as of January 2025.

Fig. 8 provides a high-level overview of the CyclObs database. It shows the distribution of observations relative to (left) cyclone intensity (by the Saffir-Simpson scale), (middle) ocean basin, and (right) missions. Tropical depressions and tropical storms contribute to about 40% of the database, while systems observed as hurricane strength or higher represent about 60% of the database. Major hurricanes (category 3 or higher) account for about 30% of the observations, the same proportion as lower intensity hurricanes. The database includes worldwide observations across all basins. In fact, SAR is the only sensor capable of providing high-resolution observations of the ocean surface, both day and night, worldwide. Observations in the Northwest Pacific and North Atlantic oceans dominate the database, each contributing about 30% of the data. Observations in the South Indian and Northeast Pacific oceans each contribute about 20% of the data, while observations in the South Pacific and North Indian oceans account for less than 10% of the available data. Finally, the distribution of the missions contributing to this database is rather balanced, with about 20% coming from S1A and each of the three RCM missions, while RS2 and S1B each contribute only 10%. S1B small contribution is due to its short period of activity (from April 25, 2016 to August 3, 2022) while RS2 short contribution is underestimated because CyclObs is not up-to-date regarding RS2 (missing data in recent years).

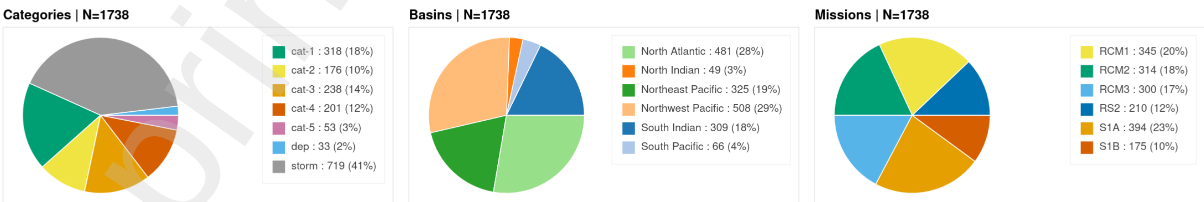

Fig. 8. High level overview of the CyclObs database. Distribution of observations relative to (left) TC intensity (by the Saffir-Simpson scale), (middle) ocean basin and (right) missions.

Top panel of Figure 9 presents the distribution of TC observations as a function of storm year with respect to mission and database. Overall, we note that the number of observations available in the two databases is about the same magnitude, with more data in recent years for the NOAA database, while the CyclObs database starts earlier. The two main reasons for the difference are related to the criteria defined by the two teams to identify data over a TC, and the quota limitations for purchased data. Apart from 2025 (since the year is not yet finished), this distribution shows a remarkable increase in coverage over time. In 2024, more than 500 observations were available, compared to fewer than 100 in 2016 when SHOC was initiated. Notably, 2023 is the turning point when CSA started to optimize their contribution to TC monitoring with the RCM mission. Beyond this date, RCM dominates the monitoring, providing an unprecedented amount of data. The period from 2016 to 2020 is dominated by the S1A/B contribution, while 2021-2022 is rather balanced between all contributing constellations. Remarkably, RS2 covers the whole period and is still active.

Middle panel of Figure 9 gives the distribution of significant named TCs observed at least one time as a function of time (storm year). After the launch of S1B, from 2018 to 2022, the CyclObs database provided at least one observation for approximately 40 TCs each year. This number increased post-2022, reaching 77 in 2024. In 2024, there were around 500 acquisitions for 77 observed TCs, compared to about 150 acquisitions for 42 TCs in 2018. This shows a significant increase in the frequency of acquisitions over time, from 3.5 observations per TC in 2018 to 6.5 observations per TC in 2024. The bottom panel further illustrates the number of observations available for characterizing TC lifecyle (green bars). This number has increased in 2016 when SHOC started with 2-3 observations per TC observed until 2022. After, C-band SAR provide an average of 6-8 observations per TC observed. In addition, the number of missed TCs by the SAR constellation (orange bars) has continuously decreased with time with a clear step in 2023. We moved from about 90% of TC not observed in 2024 when Sentinel-1 was launched to less than 20% in 2024.

Finally, Figure 10 illustrates the opportunity to acquire the TC eye when working with CyclObs data. This score is based on the ability of each SAR acquisition to cover 100% of a TC, where a TC is defined as a circle with its center at the cyclone's eye and a radius of 350 km. The TC eye center is given by an interpolation of the TC track at the time of acquisition. If the coverage is less than 40% and the TC eye center is located outside the acquisition swath, the coverage score is "likely good". For the same coverage but with the TC eye center inside the acquisition swath, the coverage score is "good". If the coverage is between 40% and 70% and the TC eye center is

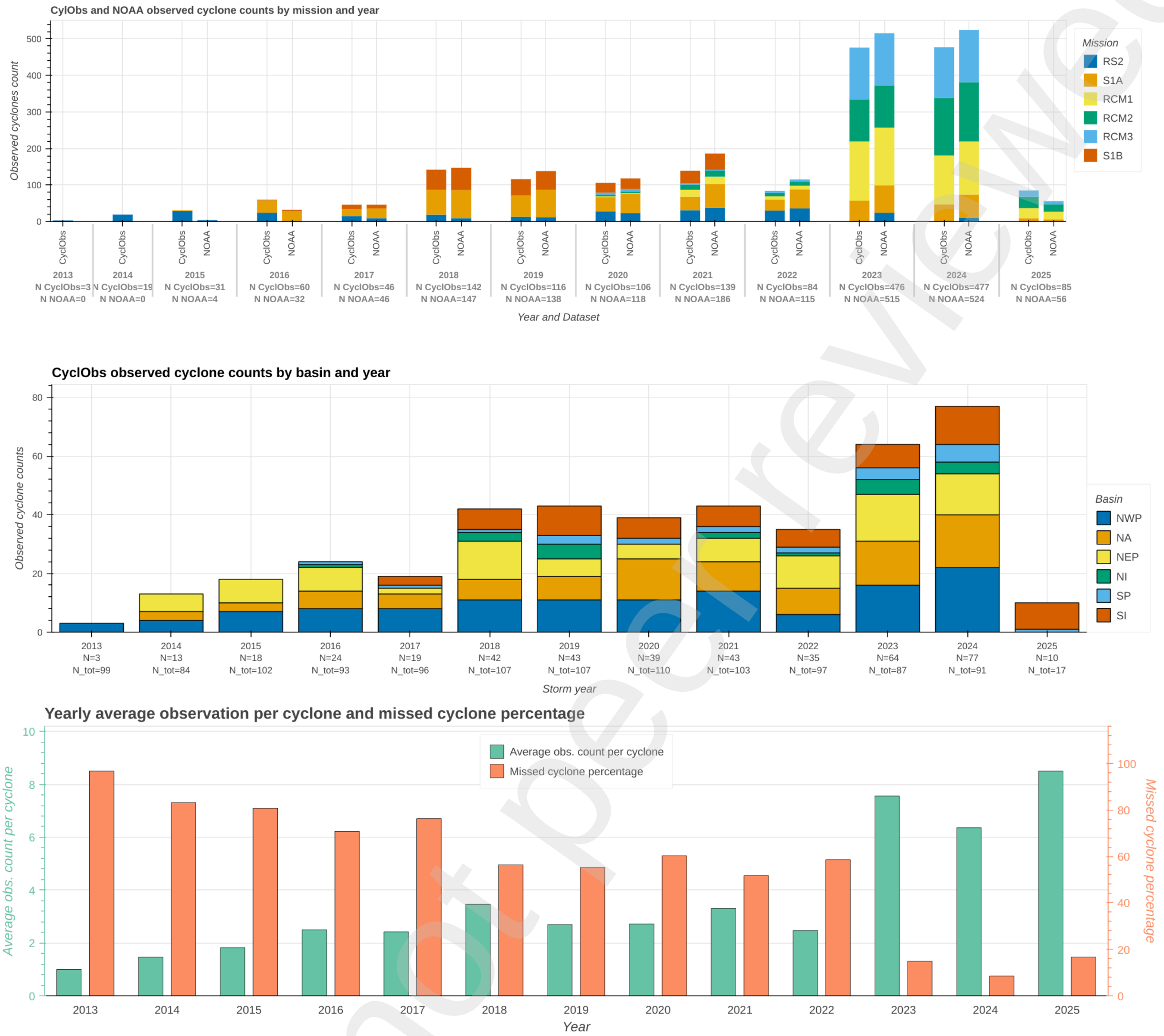

Fig. 9. Overview of the NOAA and the CyclObs database. Top panel: Distribution of TC observations as a function of storm year with respect to mission and database. Middle panel: Distribution of named TCs observed at least one time as a function of storm year

outside the acquisition swath, the coverage score is also "good". For the same coverage but with the TC eye center inside the acquisition swath, the coverage score is "very good". Beyond 70%, the score is also "very good". Overall, the analysis of the CyclObs database shows that approximately 80% of the SAR acquisitions are at least 'good,' with a large proportion of acquisitions capturing the TC eye. Comparing the sensors, we observe that Radarsat-2 acquisitions in the catalogue have the best coverage score, while Sentinel-1 B has the worst. The data policy is the main reason for this difference. Indeed because of the RS2 product cost, the data selection is very strict before ordering products to MDA. In the case of S1B, we simply select all acquisitions in the vicinity of the TC track on the Copernicus data server. The space and time criteria is relaxed to allow data not over the eye to be captured - this is interesting for ocean waves analysis. Interestingly, we also note that the performances of S1B seems to be less than S1A. This illustrates the recent improvements achieved by the Sentinel-1 planning mission team. They have managed to collect more precise information from the TC track forecast, resulting in more hits on TC eyes. Finally, this analysis suggests that the performance of the RCM acquisition methodology appears to be better than that of Sentinel-1A. However, this comparison should be put into perspective, as the Sentinel-1 acquisition strategy has evolved over time and is limited by the use of the IW mode (narrow compared to the wide swath of RCM) in coastal areas.

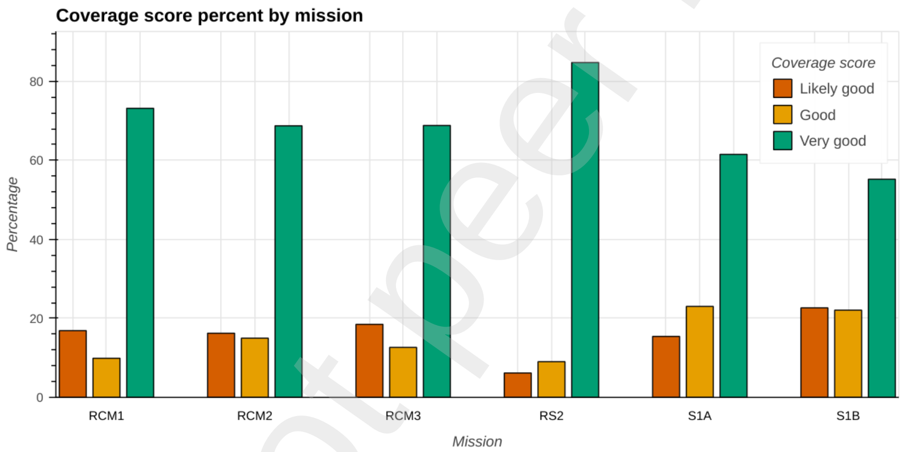

Fig. 10. SAR systems contributing to the TC monitoring with associated chance of having captured the TC center.

4. Applications

This section presents several uses of SAR acquisitions over TCs from the past decade for both operational (see section 4.1) and scientific applications (see section 4.2).

4.1. Operational centers

Operational centers have used infrared (IR) and visible (VIS) imagery from polar orbiting satellites (e.g., TIROS) since the 1960s, graduating to imagery from GEO satellites in the 1970s, then PMW imagery, all of which improves to this day (Knaff et al., 2021). SAR products were implemented and evaluated at operational centers in the late 2010s and are dramatically upgrading their capabilities. The near real time availability of SAR-based TC wind speed imagery and TC fixes allows for the widespread consideration of such information for both operational and post-season activities at all operational TC warning centers. Systematic integration of SAR-based wind speed information for operational warning and forecasting purposes and post-season reanalyzes (i.e. best tracks) has occurred at a few operational TC warning centers, and is under evaluation or informally used at several others. Below are examples of centers that have successfully integrated SAR imagery in their operations and how they have done so.

4.1.1. Joint Typhoon Warning Center

The Joint Typhoon Warning Center (JTWC) is the U.S. Military operational center responsible for TC tracking and forecasting for U.S. assets in the western North Pacific and Indian oceans and the entire Southern Hemisphere. In JTWC's vast Area Of Operations (AOR) satellite surveillance of TCs is a necessity to assess TC structure including intensity.

Operational TC structure encompasses the maximum 1-minute sustained wind, the R_{max}), and $R34$, $R50$, and $R64$ wind radii in geographic quadrants surrounding the storm (i.e. northeast, southeast, southwest and northwest quadrants). The former is referred to as "intensity" while the latter as "wind radii". The left panel of Fig. 11 shows an example of Sentinel-1A wind speed image with JTWC estimated wind radii on January 1, 2024 at 00:42 UTC over Anggrek TC (JTWC storm SH062024) with R34, R50, R64 estimates overlaid on the JTWC operational forecast system. For decades intensity has been primarily estimated from the Dvorak (1984) technique, and wind radii estimated from Ku- and C-band scatterometers. In the past decade passive radiometers and sounders have also been utilized (Knaff et al., 2021). While legacy techniques produce the information needed to provide six-hourly estimates of structure and intensity they have several well known shortcomings. In terms of intensity, the Dvorak technique has large uncertainties with weaker TCs and the most intense storms (Knaff et al., 2010). On the other hand, coverage of LEO satellites, instrument resolution and signal saturation and attenuation hamper routine wind radii estimates. Specific to this problem are the spatial resolution of radiometers and the attenuation of scatterometry often preventing confident estimation of intensity, R_{max}, R50 and R64.

Estimation of R34 has significantly improved in recent years through use of SAR, scatterometry, and radiometry surface wind analyses, and proxies from Passive MicroWave (PMW) sounders/imagers and NWP. The combined capabilities provide guidance, though not nearly enough, for six-hourly forecaster analyses required at the operational centers. The right panel of Figure 11 provides a 2023-2024 evaluation versus forecaster's estimates (i.e. final/working best tracks) of several 34-kt

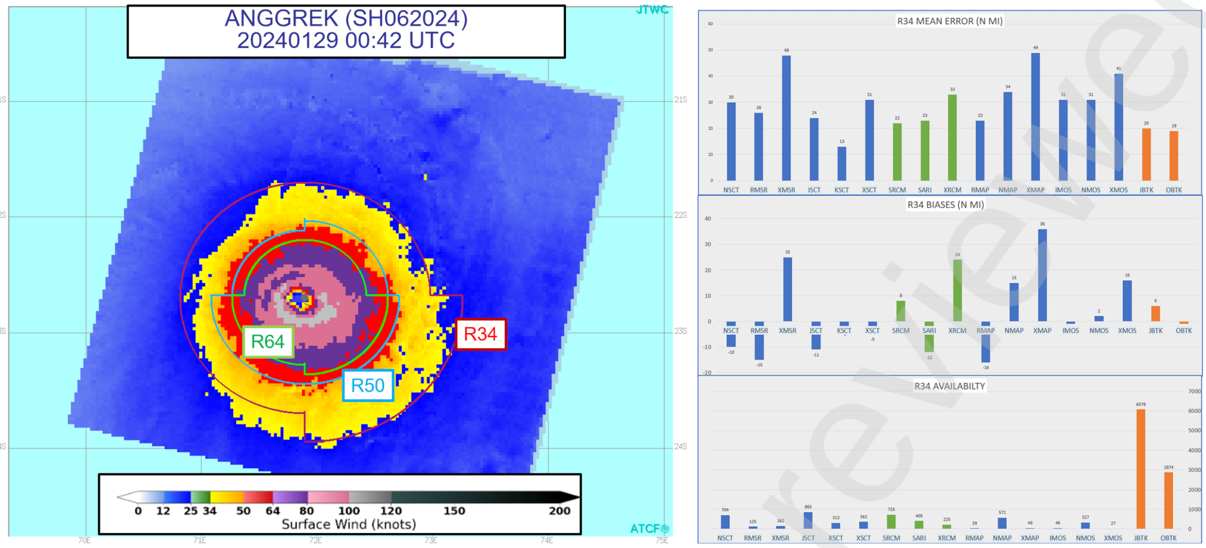

Fig. 11. (Left) Sentinel 1A wind speed image with JTWC estimated wind radii on January 1, 2024 at 00:42 UTC over Anggrek (JTWC storm SH062024) with R34, R50, R64 estimates overlaid on the JTWC operational forecast system (ATCF; (Sampson and Schrader, 2000)). (Right) Evaluation of 34-kt wind radii estimates versus the best tracks (2023-2024, through Sept 15 2024). The panels show MAEs, biases, and availability, from the top to bottom panel, respectively. The individual objective methods include: Scatterometer (Naval Research Lab; NSCT), Advanced Microwave Scanning Radiometer (Remote Sensing Systems; RMSR), AMSR (Naval Research Lab Machine Learning: XMSR), Scatterometer (Naval Research Lab Machine Learning; XSCT), Synthetic Aperture Radar (NOAA Center for Satellite Applications and Research; SRCM), Synthetic Aperture Radar (Naval Research Lab Machine Learning; XRCM), Soil Moisture Active Passive (Remote Sensing Systems; RMAP), Soil Moisture Active Passive (Naval Research Lab; NMAP), Soil Moisture Active Passive (Naval Research Lab Machine Learning; XMAP), Soil Moisture Operational Sensor (IFREMER, IMOS), Soil Moisture Operational Sensor (Naval Research Lab; NMOS), Soil Moisture Operational Sensor (Naval Research Lab Machine Learning; XMOS) The subjective methods include: Scatterometer (Joint Typhoon Warning Center Subjective; JSCT), Scatterometer (Joint Typhoon Warning Center Subjective, KSCT), Synthetic Aperture Radar (Joint Typhoon Warning Center Subjective; SARI). Finally, the two objective methods include: JBTK: Objective Best Track (Joint Typhoon Warning Center: JBTK), Objective Best Track (National Hurricane Center; OBTK)

wind radii estimation algorithms based on all available data (see caption for details). Two objective methods, JBTK and OBTK, produce equally weighted estimates from all surface wind analyses as a function of proximity to advisory time. They also use estimates from PMWs and numerical weather prediction models (NWP) are considered to fill gaps in the satellite observations, but weighted much lower than the estimates from surface wind analyses. The top panel provides mean absolute errors (MAE), the middle panel shows the biases, and the bottom panel displays the number of estimates that are available to forecasters. Despite the relatively large MAEs and biases of many of the individual methods, the objective ones show near zero bias and greatly reduced MAEs

– suggesting that combining these data produces routine R34 MAE of 20 nautical miles (1 n.mi = 1852 m) or 20% (Sampson et al., 2017, 2018), with lower uncertainty for data considered of higher fidelity (e.g., NHC subjective scatterometer estimates in their AOR).

SAR wind speeds however offer a direct instantaneous view of the winds (e.g. Fig. 11), and by using the 95th percentiles of the wind speeds in each quadrant provide high quality estimates of intensity, R50 and R64, and R_{max} (see section 3.3). JTWC relies heavily on SAR data for estimating the R_{max} and 64-kt wind radii, and when available adjust their structure estimates appropriately. These changes, because of their accuracy, tend to persist in future assessments.

Currently the creation of routine near-real-time SAR-based intensity, R_{max}, and wind radii information populate the operational "fix" databases at JTWC and forecasters use those to improve TC structure estimates and update both the working and final best track databases. SAR has enabled for the first time, detailed observation of the R_{max}, intensity and inner wind radii for all TCs. SAR-based algorithms for estimating the R_{max} (see section 3.3.2 and Avenas et al. (2023)) are now routinely applied by NOAA and available and will soon be part of the TC forecaster dialog at JTWC to provide forecasters a quality estimate of R_{max} when preparing their advisories. The availability of real-time Sentinel-1 wind speed estimates and the resulting wind speed algorithms (see section 3.3.1 and Mouche et al. (2017)) have been invaluable for assessing TC surface wind structures, and gaining experience with modern C-band cross-polarized capabilities from other SAR satellites.

4.1.2. Bureau of Meteorology

The Bureau of Meteorology is the official agency to issue TC warnings and bulletins in the Australian region between 90 and 160°E. The Bureau coordinates with other agency Regional Specialized Meteorological Centres (RSMCs) and Tropical Cyclone Warning Centres (TCWCs) under World Meteorological Organization (WMO)'s Region 5 for the east Indian Ocean and South Pacific with Fiji (Nadi RSMC), Indonesia (Jakarta TCWC), Papua New Guinea (Port Moresby TCWC) and New Zealand (Wellington TCWC). In addition to warnings for the general public and industry there are products for shipping and aviation in standard international formats, and also for input to international numerical NWPs.

These products require an analysis of the position, intensity and wind structure of a developing low pressure system or TC. The primary inputs to analysis is from the suite of geostationary and polar orbiting satellite information including visible, infrared, water vapour, microwave, scatterometry, radiometry and more recently SAR.

The operational availability of SAR high resolution winds has been enthusiastically welcomed by TC forecasters at the Bureau of Meteorology. Forecasters have appreciated efforts to increase availability, especially the addition of RCM to S1 and RS2 products, ongoing work to improve the quality through GMF upgrades, quantitative output on intensity and structure and the ease to navigate NOAA web interface. At times, there has been some degree of uncertainty regarding the appropriate weighting to be applied, especially with the introduction of RCM.

At the Bureau of Meteorology, one of the first operationally significant cases involving SAR was during TC Veronica in March 2019 (Bureau of Meteorology, 2019). Of the four SAR passes during the event was a S1A image at 10:38 UTC 24 March when Veronica was close to the north-west Australian coast. This is illustrated in Fig. 12. The maximum winds in the western sector showed values up to 95-100 kt. The satellite signature had weakened and operational estimates had reduced to 75 kt at 12:00 UTC 24 March, noting the SAR pass was not available in time. The intensity was subsequently revised to 90 kt during post analysis investigation based upon the SAR pass. Since then SAR passes have routinely been integrated into intensity analyses, although they have tended to be on the high end of the range of inputs. Forecaster trust has been challenged at times especially, although this was particularly the case in the early adoption of RCM SAR passes prior to development of GMFs specificially for RCM. Some forecasters have equated SAR winds closer to the gust value than the 10-minute wind when there have been concurrent surface observations available.

From the Bureau of Meteorological perspective, SAR provides highly reliable estimates for wind structure parameters: the extent of winds at standard thresholds of 34 kt (gales), 48 kt (storm-force) and 64 kt (hurricane-force) in addition to estimates of R_{max}.

The Bureau does not follow the intensity definition used by NOAA from both the point of view of the 1-minute wind averaging nor the spatial resolution. The highest wind speeds from NOAA web pages are higher than what would be assessed by Australian forecasters. Similarly for wind structure, the Bureau does not follow the furthest extent of winds in a quadrant for each threshold. We note the 95th percentile as an attempt to address this and having the plots available allows the forecaster to assess the appropriate extent of winds for each case. Overall, the most significant issue remains the limited availability of SAR information during an event. The infrequency of coverage and nature of being an instantaneous snapshot requires additional subjective evaluation with other information sources to determine parameters at standard analysis times. It would be helpful to forecasters if suspect wind solutions could be flagged automatically. Any further validation studies with high quality observations would be helpful to increase confidence in the output.

Forecasters would be appreciative if the timeliness of analyses could be improved.

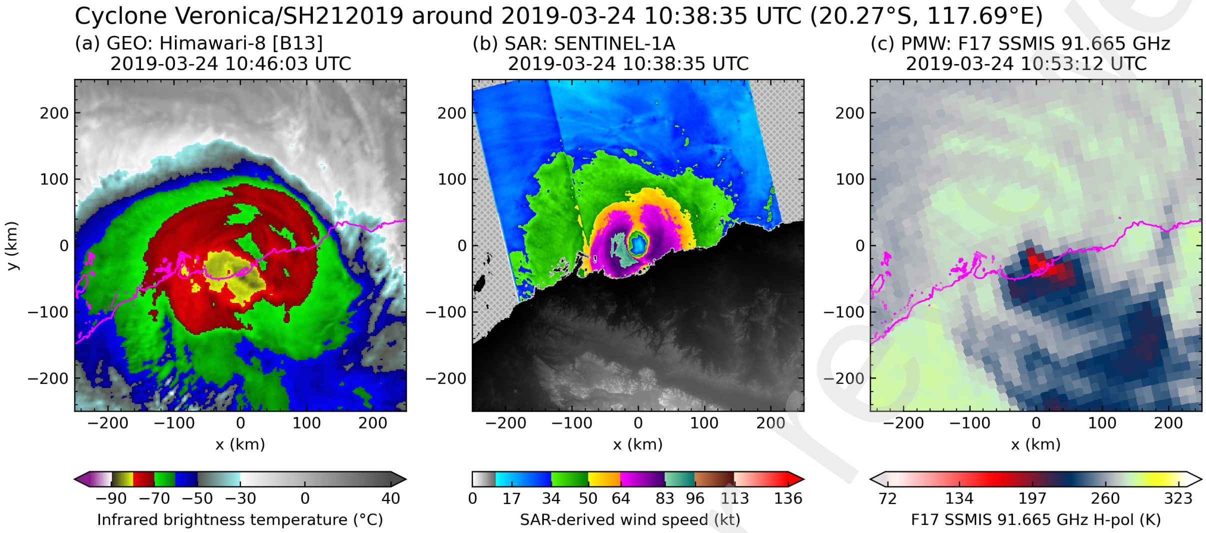

Fig. 12. TC Veronica (2019) hitting the Australian coast on March 24, observed by IR imagery at 10:46 UTC (courtesy of NOAA), by S1 SAR wind at 10:38 UTC (courtesy of NOAA) and by Special Sensor Microwave Imager / Sounder (SSMI/S) at 10:52 UTC (courtesy of NRL). Adapted from Bureau of Meteorology (2019).

4.1.3. Météo-France

Météo-France at La Réunion has been the official RSMC to issue TC warnings and bulletins in the WMO region 1 TC Committee area of responsibility since 1993. The RSMC area of responsibility is the South-Western Indian Ocean (SWIO) and extends from the African coastline east to 90°E and from the equator south to 40°S.

Unlike TC forecasters at the National Hurricane Center in Miami, TC forecasters at RSMC La Reunion do not regularly benefit from in situ or airborne TC measurements. In the SWIO, the TC intensity is defined as the maximum wind averaged over 10 min within the clockwise circulation. This has been estimated since 1982 by applying the Dvorak technique, which uses the link between the cloud configuration of a system in IR or VIS imagery and the strength of winds at the surface. Since the late 1990s, forecasters have also been using information from PMW imagers/sounders and the objective guidance associated (Herndon et al., 2012; Velden and Herndon, 2020; Velden et al., 1998; Olander and Velden, 2007) along with scatterometer data such as the currently operational ASCAT, to refine intensity estimation. On the other hand, part of the forecasting work consists in evaluating in real time structural parameters of a TC such as R_{max} and wind radii for 28, 34, 48 and 64 kt (14.4, 17.5, 24.7, 32.9 m/s, following Beaufort scale) winds, in order to assess its destructive potential (extension of destructive winds, storm surge forecast). During operations, limited time is dedicated to TC analysis. Warnings/advisories issuance (analysis and forecast of TC position, intensity and structure) is done every 6 hours at 00, 06, 12 and 18 UTC with a deadline for issuance at maximum 90 minutes after the main synoptic time (ex: TC forecast products initiated at 00 UTC should all be issued before 0130 UTC). The TC position, intensity and structure analysis at initial time of the forecast is generally refined within the hour before the synoptic time.

The exploitation of SAR data at RSMC La Réunion began in 2019, where as part of the RenovRisk measurement campaign, SAR acquisitions were specifically made on the SWIO. This data, supplemented with SAR acquisitions dating back to February 2017, allowed forecasters to assess the quality of the wind retrieval compared to the RSMC best-track data. A comparison of SAR data from the 2017-2020 period (converted into 10-min equivalent max winds) was made by Duong et al. (2021). A correlation of about 0.8 was reported between the 2 datasets.

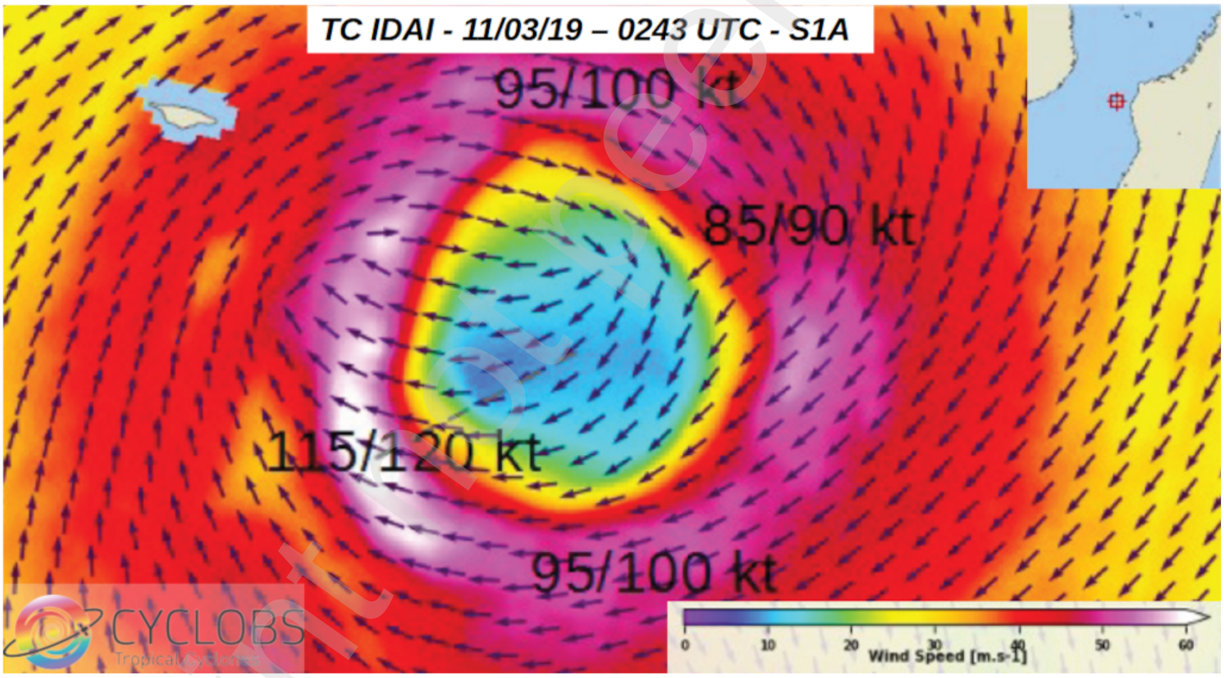

Fig. 13. One of the first SAR passes used in near real time at RSMC La Réunion during the RenovRisk Campaign for Intense TC Idai: it was the first time that a quantitative visualisation of the wind asymmetries within the eyewall of an intense TC was possible based on a space-borne platform.

Operational SAR data exploitation has been carried out since 2021 via the dedicated NOAA website (STAR-SOCD). The implementation of semi-automated diagnostics on the position, maximum intensity (95th percentile of wind profiles by quadrants) and wind radii is appreciated by forecasters for the time saved in exploiting the data. Weight given to SAR data in the analysis process is increasing over the years, whether in operational (despite the latency of product arrival, SAR data deemed reliable makes it possible to recalibrate the initial intensity estimate during the next forecast) or during the post-storm reanalysis work (best track).

In this context, the exploitation in near-real time of SAR wind data has the potential to significantly improve the confidence in the initial state of a TC for all TC warning centers located in areas with no or little in situ observations. To completely fulfill this expectation, a SAR pass every 6 hours over the TC between H-6 and H-3 (H is the synoptic time) with the wind retrievals and post-processing (position fixing, intensity and wind radii measurements) done and available to TC forecaster workstation 2 hours later (eg. H-4 or H-1), would be ideal.

Despite their invaluable contribution to the activities of the RSMC La Réunion, there remain several inherent challenges associated with the use of SAR data:

- While current products are designed to have 1-min wind equivalents, it would be desirable to have SAR products that are more directly interpretable in terms of 10-min winds (4 official TC warning agencies use 10-min average winds).

- Wind radii are very often greater than what a forecaster would have plotted by himself (limit of diagnosis at the 95th percentile which would deserve to be lowered to the 90th percentile).

- While in some cases this may only be attributed to the wind speed definition difference (1-min in SAR instead of 10-min at RSMC La Reunion), in some cases of overestimation, the validity of the SAR data can be questioned (see the case of Bheki on Fig. 14 and discussion below). However, it should be noted that this is clearly not a generality: there are cases where the SAR measurement is lower than the estimate given by the Dvorak technique (see the case of Vince on Fig. 14 and discussion below). It is certainly necessary to continue the calibration work with the most reliable in situ data possible to give further confidence to the data.

- The irregularity of TC SAR coverage is also a challenge, particularly during the genesis or early intensification phases which are generally poorly covered. This is also detrimental when a unique SAR pass in 24/36 hours shows believable stronger winds than other guidance (see the Chido case on Fig. 14 and discussion below).

Based on observations by IR imagery, SAR and Special Sensor Microwave Imager/Sounder (SSMI/S) at 91 GHz, the three challenges mentioned above and illustrated in Figure 14 are further discussed here:

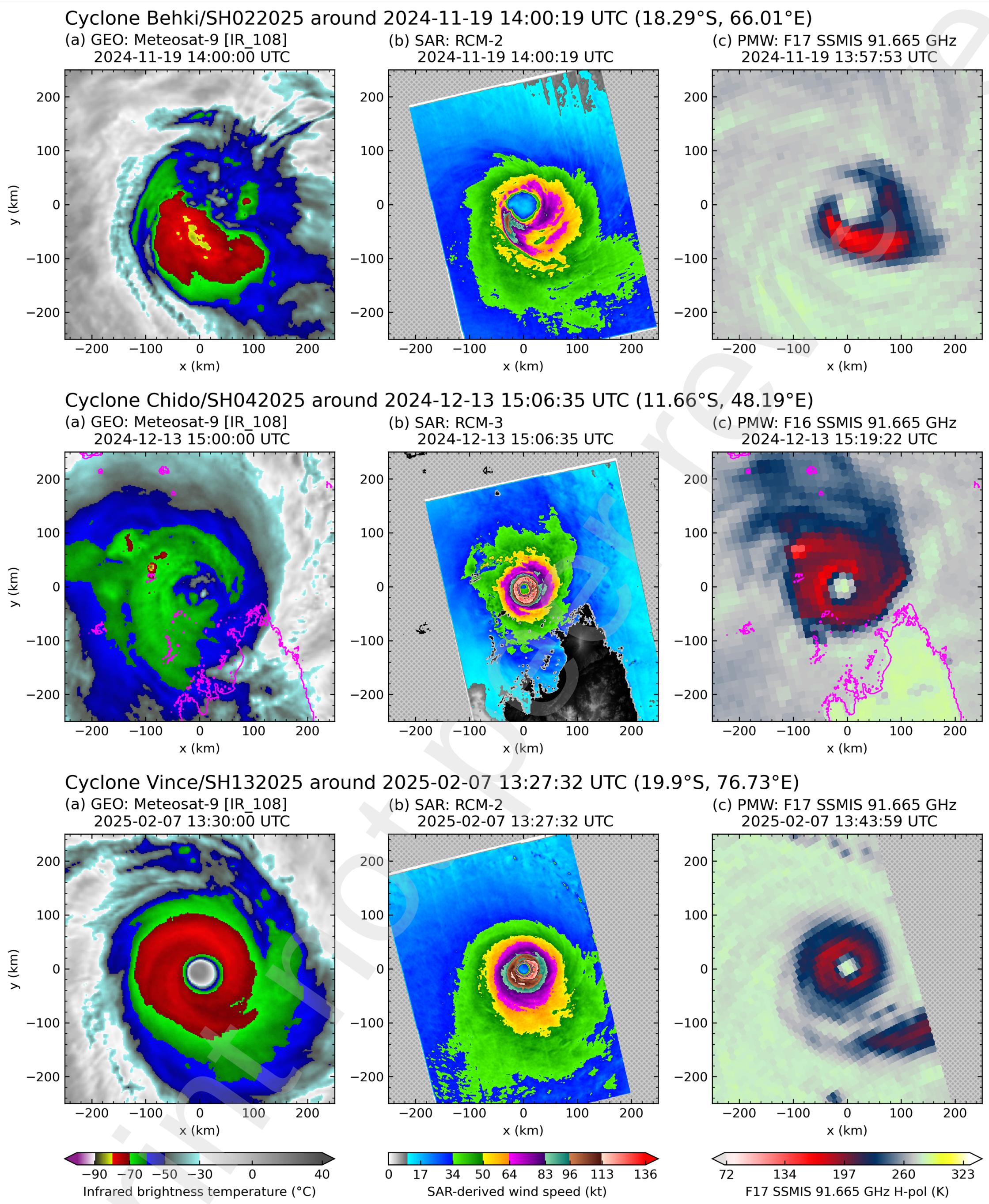

Fig. 14. 3 examples of TC observed by IR imagery (courtesy of NOAA), SAR imagery (courtesy of NOAA) and SSMI/S imagery at 91 GHz (courtesy of NRL) for TCs Bheki (top panel), Chido (middle panel) and Vince (bottom panel).

- Bheki: Top panel of Figure 14 shows observations of TC Bheki as windshear constraint induced convective asymmetries within the eyewall. SAR winds within the southern eyewall were assessed as unreliable with areas of reduced/enhanced signal in potential association with extremely deep convection (south the eye). While more research is needed to fully understand what happened in these cases, quality control flags would be beneficial if areas of suspect backscattter can be identified.

- Chido: Middle panel of Figure 14 shows observations of TC Chido about 15 hours before devastating Mayotte island. SAR and microwave data were critical in decisions to maintain Chido intensity above other satellite guidance despite a significant deterioration of the cloud pattern in IR imagery. 12 hours later (and a few hours before Chido hit Mayotte), a new SAR pass was missing to follow the evolution of the TC intensity while the geostationary satellite, and to a lesser extent the microwave signature, continued to deteriorate in the meantime.

- Vince: Bottom panel of Figure 14 shows observations of TC Vince near its peak intensity. This illustrates a case where the intensity seen in SAR winds is below subjective Dvorak estimate T-number (Dvorak, 1972) at 7.0 (140 kt 1-min winds) from three different agencies.

4.1.4. Japan Meteorological Agency

The Japan Meteorological Agency (JMA) is the official agency in Japan to issue TC warnings and information (10-min maximum wind speed $V_{\mathrm{max}10}$, R_{30} and R_{50}) wind radii in the western North Pacific and the South China Sea between 100 and 180°E. The JMA also operates the RSMC Tokyo - Typhoon Center under the WMO to provide TC information, including analyses and forecasts in the same areas of their responsibility. However, the information provided by the RSMC Tokyo - Typhoon Center represents neither official analysis/forecasts nor warnings for the areas concerned. For more details see RSMC Tokyo - Typhoon Center website[1].

Prior to the advent of SAR wind products, there were no high-resolution estimates of intense surface wind speeds from space. This situation is a serious issue for TC-related disaster mitigation, especially in the western North Pacific where there is no operational aircraft reconnaissance. Although SAR wind products are expected to greatly contribute to the estimation of TC intensity and inner-core structure with high accuracy, the consistency between the new wind products and conventional best track estimates remains to be evaluated in the context of JMA missions.

Shimada et al. (2024a) compared SAR wind speeds from RS2 and S1 missions equivalent to the 1-min sustained wind speed provided by the CyclObs database (from 2012 to 2021) with the best

[1] https://www.jma.go.jp/jma/jma-eng/jma-center/rsmc-hp-pub-eg/advisory.html

track estimates provided by the JMA ($V_{\max 10}$ and R_{30} and R_{50}). They defined the SAR-observed maximum wind speed (SAR $V_{\max}$) as the 99$^{\text{th}}$ percentile of SAR wind speeds observed within 200 km of the center. The 99$^{\text{th}}$ percentile was chosen to remove noise in the SAR wind products and instantaneous high wind speeds that are not representative of the TC vortex. Because of the inconsistency between SAR $V_{\max}$ equivalent to the 1-min sustained wind speed and JMA best track $V_{\max 10}$, an appropriate conversion method was explored, including the use of a conversion factor of 0.93 recommended by WMO (Harper et al., 2010) and the use of the Dvorak conversion tables often used to estimate the JMA $V_{\max 10}$ from the JTWC $V_{\max}$ (e.g., Mei and Xie (2016); Kawabata et al. (2023)). SAR $V_{\max 10}$ converted by the latter method was more suitable for JMA $V_{\max 10}$. This study also addresses the correction of an incidence-angle-dependent bias observed in the SAR wind products. This bias has since been corrected through a revision of the algorithm, based on an extended database of SAR data colocated with SFMR measurements. Top left panel of Fig. 15 shows a scatter plot of SAR $V_{\max 10}$ vs JMA $V_{\max 10}$. The mean absolute difference ($\Delta V_{\max 10}$) between them is 4.8 m.s^{-1}. This result suggests that with appropriate treatments, SAR winds can be used to estimate JMA $V_{\max 10}$.

The remaining negative and positive biases seen in top left panel of Fig. 15 are similar to the known intrinsic bias in the Dvorak technique. Knaff et al. (2010) noted that intensifying TCs tend to be underestimated and weakening TCs tend to be overestimated by the Dvorak technique. In fact, top left panel of Fig. 15 shows that $\Delta V_{\max 10}$ is a function of current intensity and subsequent intensity changes up to 24 h (colours). The correlation coefficient between $\Delta V_{\max 10}$ and subsequent 24-h $V_{\max 10}$ changes was –0.48. One exception for this correlation was seen in extratropical transitioning TCs. The top right panel of Fig. 15 shows that all six extratropical transitioning TCs examined have SAR $V_{\max 10}$ greater than JMA $V_{\max 10}$. This result suggests that for extratropical transitioning TCs, the best track $V_{\max 10}$ tends to be underestimated by conventional methods.

As for R_{30} and R_{50} in the JMA best track data, bottom panels of Fig. 15 shows that R_{30} is generally consistent with SAR wind speeds, whereas R_{50} is underestimated relative to SAR wind speeds. The underestimation of R_{50} may be influenced by the use of scatterometer winds (e.g., ASCAT) and AMV-derived winds (ASWinds), which have a negative bias for wind speeds above 18 m.s^{-1} (e.g., Chou et al. (2013); Nonaka and Igarashi (2019)).

In addition to TC monitoring using SAR wind products, Ikuta and Shimada (2024) conducted a data assimilation experiment by operational NWP systems for TC prediction. Given the present wealth of SAR observations, improvements of weather forecasting accuracy are expected. Already, initial conditions in NWP are currently generated by assimilating a large number of reliable

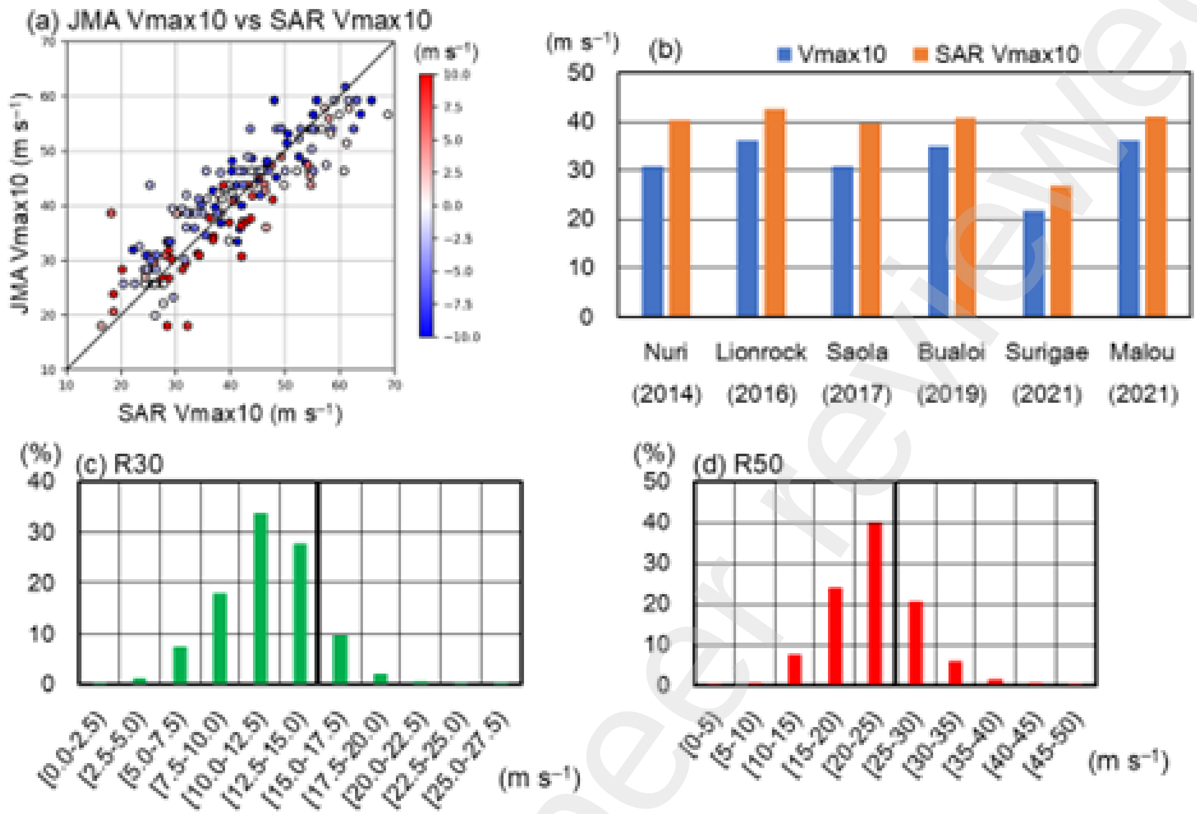

Fig. 15. Scatter plot of SAR V_{max10} versus JMA best track V_{max10} (Top left). JMA best track V_{max10} and SAR V_{max10} of extratropical transitioning TCs (Top right). Frequency histograms of SAR wind speeds on the JMA R30 (bottom left) and R50 (bottom right) circles.

medium resolution observational data. When SAR wind speeds are included, the probability density function for the observational minus background generally displays distributions with heavier tails, compared to a Gaussian distribution. This is key to not consider SAR surface winds as outliers. In a case study of Typhoon Hagibis (2019), a 4D-Var methodology using SAR ocean surface wind speed demonstrated skill in analyzing a secondary circulation within the TC, further changing the outflow of the TC in the middle troposphere. Adjustments in the lower atmosphere from SAR observations then propagate upward, and can thus significantly improve atmospheric high wind speed forecasts.

Finally, the Meteorological Research Institute (MRI) of JMA and the Japan Aerospace Exploration Agency (JAXA) have a joint project to develop L-band SAR wind products (see section 5.2.1). In this way, JMA is considering how to effectively use SAR products from various perspectives.

4.2. Sciences applications

Several examples of scientific studies that have been developed using SAR observations are highlighted below. A single instantaneous SAR acquisition can provide enough information to describe a TC surface wind field, including the R_{max}, as discussed in Section 4.2.1. Knowledge of vortex parameters, especially within the inner- and near- core, can then be used to understand the interactions between the wind forcing and the ocean. In synergy with other measurements, SAR passes can also provide more detailed observations to aid in the study of TC wave generation processes (see Section 4.2.2) and TC-induced wakes in the ocean (see Section 4.2.3). Section 4.2.4 illustrates the benefit of having both the ocean surface wind field at 1-km resolution and a higher resolution image to infer TC boundary layer properties and the TC wind vertical profile. Finally, Section 4.2.5 describes work employing high-frequency observations to study TC dynamics based on SAR wind measurements.

4.2.1. Tropical cyclones wind structure

As described in Sections 3.3 and 3.4, the constellation of existing C-band and dual-polarization SAR missions provides a unique, comprehensive, and homogeneous data set to document the inner and outer cores of TCs over all ocean basins. This certainly aligns with one of the requirements expressed during the last international workshop on TCs to get high-quality and homogeneous wind structure reference data sets (Duong et al., 2023). These acquisitions have already facilitated several studies on the TC wind structure. They have also supported initiatives to develop new algorithms for other sensors, such as those on board GEO satellites and PMW imager/sounder.

Taking advantage of the high resolution of SAR, Avenas et al. (2023) offered to statistically estimate R_{max} from an outer wind radius. The method followed and improved the framework of Chavas and Knaff (2022) and is based on both V_{max}, f and an outer wind radius as predictors, where f is the Coriolis parameter defined as $f = 2\Omega sin(\phi)$ with $\Omega = 7.292x10^{-5}\ s^{-1}$ the Earth angular velocity and ϕ the latitude of the TC center. Following Avenas et al. (2023), the smallest available wind radius R_{xx} among R_{64}, R_{50}, and R_{34} can be used as outer wind radius predictor to maximize its correlation with R_{max}. Building on the ability of SAR sensors to accurately estimate R_{max} and using triplets (V_{max}, f, and R_{xx}) as predictors, the statistical relationships found are:

$$\frac{M_{\max}}{M_{34}} = 0.531\exp\{-0.00214(V_{\max} - 17.5ms^{-1}) - 0.00314(V_{\max} - 17.5ms^{-1})(\frac{1}{2}fR_{34})\}, \quad (2)$$

$$\frac{M_{\max}}{M_{50}} = 0.626\exp\{0.00282(V_{\max} - 25.7ms^{-1}) - 0.00724(V_{\max} - 25.7ms^{-1})(\frac{1}{2}fR_{50})\}, \quad (3)$$

$$\frac{M_{\max}}{M_{64}} = 0.612\exp\{0.00946(V_{\max} - 32.9ms^{-1}) - 0.01183(V_{\max} - 32.9ms^{-1})(\frac{1}{2}fR_{64})\}. \quad (4)$$

with $M_{\max}$, M_{34}, M_{50}, and M_{64} the absolute angular momentum values at $R_{\max}$, R_{34}, R_{50}, and R_{64}, respectively. Estimates of $R_{\max}$ may then be obtained using absolute angular momentum conservation:

$$R_{\max} = \frac{V_{\max}}{f}\left(\sqrt{1 + \frac{2fM_{\max}}{V_{\max}^2}} - 1\right). \quad (5)$$

The method can be applied to any set of predictors ($V_{\max}$, f, and R_{xx}). Note, in Eqs. 2-5 and in the rest of the section the structural parameters ($V_{\max}$, $R_{\max}$, and R_{xx}) refer to estimates based on axisymmetric wind profiles. This is not fully homogeneous with the methodology that yields best-track parameter estimates, for which $V_{\max}$ in particular stems from a two-dimensional wind field analysis from TC agencies. Avenas et al. (2023) performed a least-squares regression to link an axisymmetric SAR intensity estimate to a best-track intensity estimate (their Eq. A1), while a nonzero average of the wind radii values from the four different geographical quadrants can be computed to mimic an axisymmetric R_{xx} estimate from best-track data.

Fig. 16 presents the $R_{\max}$ best-track estimates for Hurricane Kirk (2024), derived from SAR observations (magenta crosses), along with $R_{\max}$ estimates obtained by applying the statistical relationships established on SAR data (Eqs. 2-5, orange diamonds), and $R_{\max}$ from GEO (purple squares) and MWS sensors (green circles) as presented below. The SAR $R_{\max}$ estimates (magenta crosses) are mostly in agreement with the best track $R_{\max}$ estimates from NHC (solid black curve), except during the phase when the storm is the most intense, that is, between October 03 and October 06 (see blue dashed curve of the $V_{\max}$ best-track estimates). During this phase, best-track $R_{\max}$ estimates remain constant and are overestimated compared to SAR $R_{\max}$ estimates. $R_{\max}$ predictions from the SAR-based statistical relationship (orange diamonds) agree with the SAR $R_{\max}$ direct estimates, especially during the most intense phase of the TC. Before this intense phase, particularly on October 1st, some discrepancies between the SAR $R_{\max}$ estimates and the predictions can be noticed. On October 1st, the two SAR acquisitions displayed an asymmetric wind

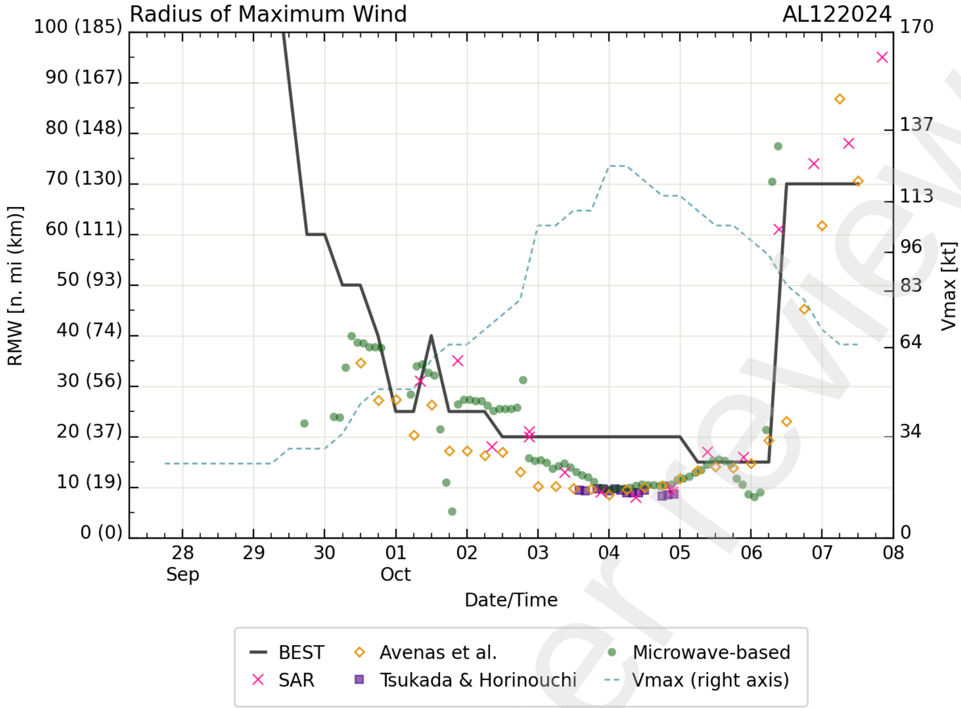

Fig. 16. $R_{\max}$ and $V_{\max}$ estimates from different data sources for Hurricane Kirk (2024). The solid black curve and dashed light blue curve represent the $R_{\max}$ and $V_{\max}$ from the NHC's best track data. The magenta crosses denote the SAR-derived $R_{\max}$. $R_{\max}$ estimates are shown as orange diamonds for Avenas et al. (2023), purple squares for Tsukada and Horinouchi (2023), and green circles for Shimada (2024a,b)

field (not shown) at dawn and dusk. This asymmetry tends to produce high axisymmetric $R_{\max}$ estimates from the SAR data. The methodology designed with an axisymmetric assumption fails to correctly predict the SAR $R_{\max}$ estimate in that case. In addition, for such cases, the asymmetric wind field implies that R_{xx} estimates do not take non-zero values for all four geographical quadrants in the best track for that day, making the quadrants-averaging procedure more uncertain and the method less efficient. On October 2nd morning (not shown), the eye is cropped and the instrument swath may miss strong wind speeds that occur further apart from the storm center. The SAR $R_{\max}$ estimate may be underestimated because of this lack of information. Thus, the consistency between the SAR $R_{\max}$ estimate and the prediction for that particular overpass may be an artifact of this measurement limitation. Overall, the wind field still looks asymmetric during this day both in the morning and evening. Again, this is a typical unfavorable situation where only one or two values for R_{xx} are defined in the track and the SAR axisymmetric $R_{\max}$ estimate might not be captured by the methodology of Avenas et al. (2023).

Indirect means of estimating the surface winds from upper-level measurements may help coping with the low spatio-temporal sampling of SAR instruments and partially fill the gaps in the resulting infrequent observations. In particular, GEO meteorological satellites offer frequent observations of VIS reflectivity or IR radiances over all ocean basins. Especially from the third-generation GEO satellites, such as Himawari-8/9 (Bessho et al., 2016), GOES-16/17/18/19 (Schmit et al., 2017), Meteosat-12 (Holmlund et al., 2021), and GEO-KOMPSAT-2A/2B (Kim et al., 2021), full-disk imagery can be obtained every 10 to 15 minutes covering the entire globe. Furthermore, the rapid-scan operation of TC is also available with a frequency of just a few minutes. Several studies already attempted to take benefit of GEO's high sampling rate to monitor the storm intensity and investigated the relationship between the sea surface wind field and IR brightness temperature field as past research has indicated (e.g.Mueller et al. (2006); Kossin et al. (2007); Knaff et al. (2014)). Building upon this, Tsukada and Horinouchi (2023) used the existing CyclObs SAR wind database to elucidate the relationship between the features observed in SAR and GEO satellite products and derive ocean surface wind properties from GEO. As an example, Fig. 17 shows the SAR-derived wind speed (Sentinel-1A) and the IR image (GOES-16) for Hurricane Franklin (2023) around 2023-08-29 10:44 UTC, just before the end of the eyewall replacement cycle. In these scenes, R_{max} identified in the SAR wind field is smaller than that in the IR image, indicating vertical slope of the eyewall. Furthermore, a weaker wind region is detected in the SAR wind field, with a warm (less convective) region evident in the IR image approximately 40 km south of the storm center. By training a regression model that fits SAR-based R_{max} using GEO-based the eye radius (R_{eye}) measurements Tsukada and Horinouchi (2023) developed a new algorithm to estimate the radius of maximum wind from GEO IR estimates of R_{eye}. In their analysis, SAR R_{max} and IR R_{eye} exhibit a strong relationship when the storm has a clear eye, determined by objective criteria in the IR image (Fig. 17). The linear regression for R_{max} follows:

$$R_{\mathrm{max}} = 3.01 + 0.60 R_{\mathrm{eye}}, \tag{6}$$

with units in km, resulting in a MAE of 1.7 km for clear-eye cases and enabled high-frequency and accurate R_{max} estimation across all ocean basins when the storm has a clear eye. Fig. 16 shows results from Hurricane Kirk (2024) where the R_{max} estimates retrieved by this methodology are consistent with the SAR R_{max} estimates for the period from October 03 afternoon to October 05. Even though R_{max} can only be estimated for a limited 36-hour window with this method (i.e., when the eye is clear), this period covers the most intense phase of the life cycle, for which best-track R_{max} estimates are limited (Combot et al., 2020a).

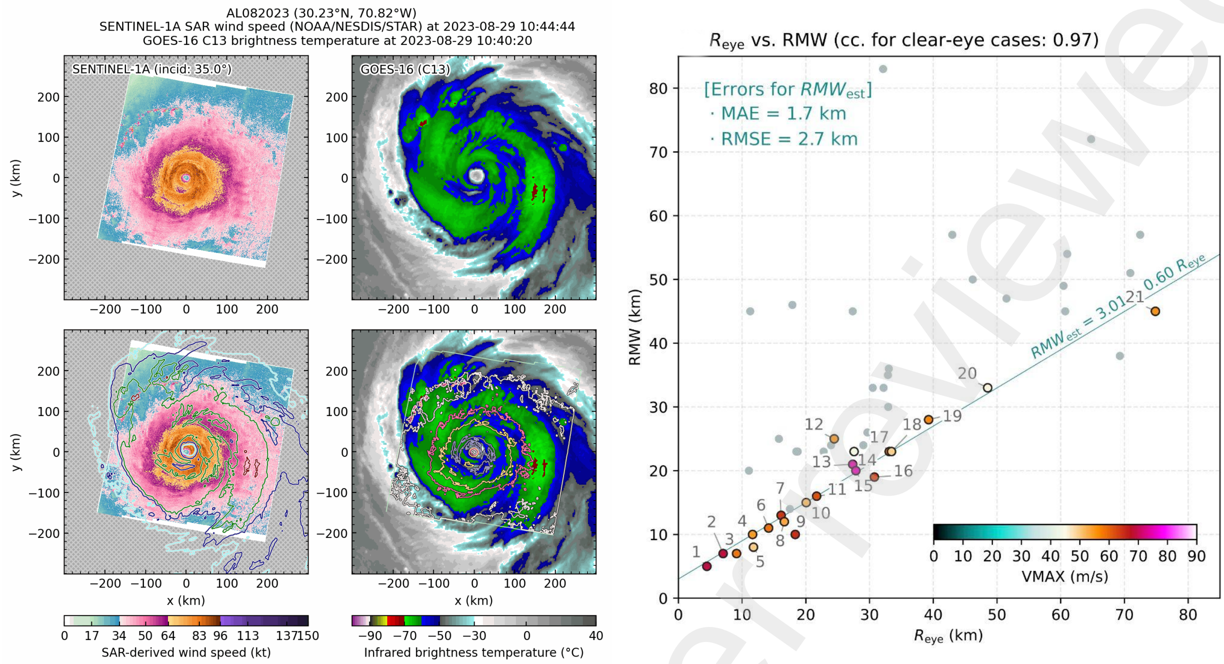

Fig. 17. (left) Sentinel-1A SAR-derived wind speed and (right) GOES-16 channel 13 IR brightness temperature for Hurricane Franklin (2023) around 2023-08-29 10:44 UTC corresponding to just before the end of the eyewall replacement cycle. The bottom panel displays their counterparts with contours. Note that the parallax correction for the IR image is not performed.

In addition to this framework, a microwave-based approach for estimating the R_{max} is currently under development (Shimada, 2024a,b). Two specific estimation methods are proposed using 89 GHz PMW satellite data, with the SAR-observed R_{max} used as ground truth. The first method uses linear regression to relate the –40 °C radius of the azimuthal mean 89 GHz brightness temperature (89TB) to the R_{max}. This method is applicable when the eyewall ring structure is well-defined. After removing cases with concentric or asymmetric eyewalls based on objective thresholds, the R_{max} can be estimated with a MAE of 2.8 km. The second method identifies the R_{max} as the radius where the azimuthally-averaged 89TB radial gradient is most negative. This method yields a MAE of 17.4 km. By combining the two methods, a 72% chance of estimation was achieved among the available PMW satellite data samples.

Overall, the microwave-based R_{max} estimates (green circles) agree with the other estimates during the most intense phase of the storm, especially from October 03 at noon to the end of October 05. Before that phase, while the microwave-based R_{max} estimates in the morning of October 01 are consistent with the SAR R_{max} estimate on that time, discrepancies are noticed in the evening of October 01 and the morning of October 02. In the evening of October 01, the strong wind field asymmetries may explain the difference. In the morning of October 02, the PMW imagery indicates that strong convection to the south of the storm has become active, which may impact the methodology of Shimada (2024a,b). Structural changes over time are exhibited by the PMW imagery at both dates, possibly increasing the uncertainty of resulting $R_{\max}$ estimates. Interestingly, the wind field in the morning of October 01 was also asymmetric, similar to the evening, but had minimal structural changes over time and a small difference between the microwave-based $R_{\max}$ estimates and that of SAR.

The three different $R_{\max}$ methods presented here are complementary and should not be used independently. Based on surface wind structure parameters (R_{xx}), predicted $R_{\max}$ values from Avenas et al. (2023) are generally consistent with the one-dimensional SAR $R_{\max}$ estimates. The relationship holds as long as $V_{\max}$ is greater than 20 m/s, thus providing means to assess the TC life cycle in its entirety. During the most intense phase of the life cycle, the relationship of Tsukada and Horinouchi (2023) will refine these estimates when the eye is clear, benefiting from the high temporal resolution of GEO sensors. Finally, the framework proposed by Shimada (2024a,b) also shows great consistency with the SAR $R_{\max}$ estimates when the eyewall is clearly defined in PMW data. Overall, $R_{\max}$ estimates from all methodologies agree well in the most intense phase of the TC (between October 03 afternoon and October 05 included). The combination of these different strategies may therefore be practical in estimating $R_{\max}$ during this phase, for which best-track estimates are limited in the absence of reconnaissance aircraft. This investigation and resulting algorithms demonstrate the benefit of building a comprehensive SAR database of TC observations.

Beyond $R_{\max}$, models to describe the variation of wind speed with respect to the distance from the TC center or the asymmetry of the wind field are also widely used for many applications such as risk assessment, wave, or storm surge modeling. The most widely models to describe the wind profile are certainly the physically-based model from Holland (1980a) and the empirical model from Willoughby et al. (2006), while the model from Olfateh et al. (2017) allows to describe the wind field asymmetry. There have been recent attempts to leverage the potential of SAR to refine or extend existing models (Zhang et al., 2014; Wang et al., 2021; Gao et al., 2021). These efforts are still limited by the number of scenes considered for the study—only tens of scenes—whereas the model proposed by Willoughby et al. (2006) relied on about 500 aircraft radial wind profile measurements, but they will certainly benefit from the now extended SAR database.

4.2.2. Tropical cyclones ocean surface waves

Strong winds varying at km scales inside TCs make wave generation processes likely very complex and still not properly understood. Inside TCs, i.e. winds higher than 17 m/s and intense inner cores, rapid wave growth is largely dominated by transfers of energy toward low frequencies. Peak wavelengths and associated energies increase until wave systems become more organized and directional, eventually outrunning the strong winds responsible for their generation.

Storm motion has long been recognized as a dominant factor responsible for generating waves in the TC's right sector (Cline, 1920; Tannehill, 1937). In this sector, with waves often remaining under high wind forcing conditions for a longer time than usual. This has been termed extended fetch, trapped fetch, or group velocity quasi-resonance. Storm motion can then make the induced wave field more asymmetric than the generating wind field. The TC size, wind field distribution and associated large directional gradients can further enhance these resulting wave field asymmetries.

Accordingly, SAR derived high resolution information related to the TC wind structure provides key drivers to anticipate the surface wave developments during these extreme varying wind forcing conditions. For instance, Kudryavtsev et al. (2015) built on the expected self-similarity aspect of wind wave growth and proposed a simplified criterion to anticipate wave enhancement with the generation of trapped abnormal waves defined as:

$$\frac{gr}{V(r)^2} = C\left(\frac{V(r)}{V_{\text{fm}}}\right)^{1/q}, \tag{7}$$

where g, r, $V(r)$, and V_{fm}, the gravity constant, radial distance, average sustained wind speed at r, and translation velocity, respectively. Constants q and C follow from the fetch-law definitions (q varies between -0.23 and -0.33, and C is about 6.5×10^4). Young (1988) proposed an equivalent fetch defined in terms of the TC parameters: translation velocity, maximum wind speed, and $R_{\max}$. In Kudryavtsev et al. (2015), this behavior is characterized by the critical fetch L_{cr}, the distance that a developing wave train travels before its group velocity equals the storm translation velocity V_{fm}. Knowing the TC's translation vector along with a SAR observation of the wind field provides precise TC structure characteristics ($R_{\max}$, $V_{\max}$, B the shape parameter of the Holland wind profile Holland (1980b)), to evaluate L_{cr} (347 meters as shown in the left panel of Fig. 18) and anticipate the role of resonance effects to increase the effective fetch and duration of the wave-growth process in the direction of the storm motion. In other words, this provides information about the wave trapping phenomenon with associated longer waves developing in the forefront of the TC. Note, the expected longest and highest waves a non-moving axisymmetric TC can develop, may also both be estimated following self-similar wind wave growth (Kudryavtsev et al., 2021; Yurovskaya et al., 2023):

$$\lambda = 2\pi \frac{V(r)^2}{g} c_\alpha^{-2} \left(\frac{rg}{V(r)^2} \right)^{-2q}, \qquad H_s = 4 \frac{V(r)^2}{g} c_e^{1/2} \left(\frac{rg}{V(r)^2} \right)^{p/2}. \tag{8}$$

With $c_\alpha = 11.5$, $c_e = 0.65 \times 10^{-6}$, $q = -0.27$ and $p = 0.87$. Accordingly, wavelengths of the longest waves generated by a non-moving axisymmetric TC increase proportionally to $V_{\max}$ and to the square root of $R_{\max}$. A translating TC, on the other hand, will modify surface wave energy and wavelengths. Changes depend on the ratio between r, the distance from the TC eye, and the local critical fetch $L_{\mathrm{cr}}(V(r), V_{\mathrm{fm}})$ (see eq. 7 in Kudryavtsev et al. (2021)). From a S1 IW acquisition over TC Surigae (2021) in the Western Pacific, both wind speed (left panel) and significant wave height (right panel, with method adapted from Stopa and Mouche (2017)) fields are estimated (Fig 18). The red circle around the TC center provides the location of the highest waves generated by a stationary TC with the same properties. On the SAR image, significant wave height seems quite homogeneous up to about 2 $R_{\max}$, while the most energetic stationary waves are located between 1 and 1.5 $R_{\max}$. The TC translation here has a strong impact on the wave growth and acts to extend the fetch effect to the outer core.

Long swell systems, emanating from the intense TC inner core region, can then disperse in different directions with different wavelengths. The waves cease to be forced by the local winds, but can experience dissipation and nonlinear interactions. Far from the generating area, swells propagate along great-circle routes, to become fingerprints of the extreme weather events (Snodgrass et al., 1966; Ardhuin et al., 2009). Gathering far-field directional wave information extracted from Sentinel-1 wave mode, CFOSAT SWIM (Hauser et al., 2020), combined with Sofar Spotter drifters (Houghton et al., 2021) and NDBC buoy network, Pouplin et al. (2024) applied back-propagation methods (Collard et al., 2009; Hell et al., 2021). Using the resulting TC-wave rose distribution (see Fig. 2 in Pouplin et al. (2024)), far-field directional waves can thus provide information about the time-evolving characteristics of a given TC ($V_{\max}$, $R_{\max}$, B, V_{fm}). With this methodology, particular events can then be traced and quantified by detecting variations of the asymmetrical directional wavelength distributions. In addition, a forward-propagation methodology may also be used as demonstrated in Fig. 19. Thus, by taking advantage of the Sentinel-1 IW

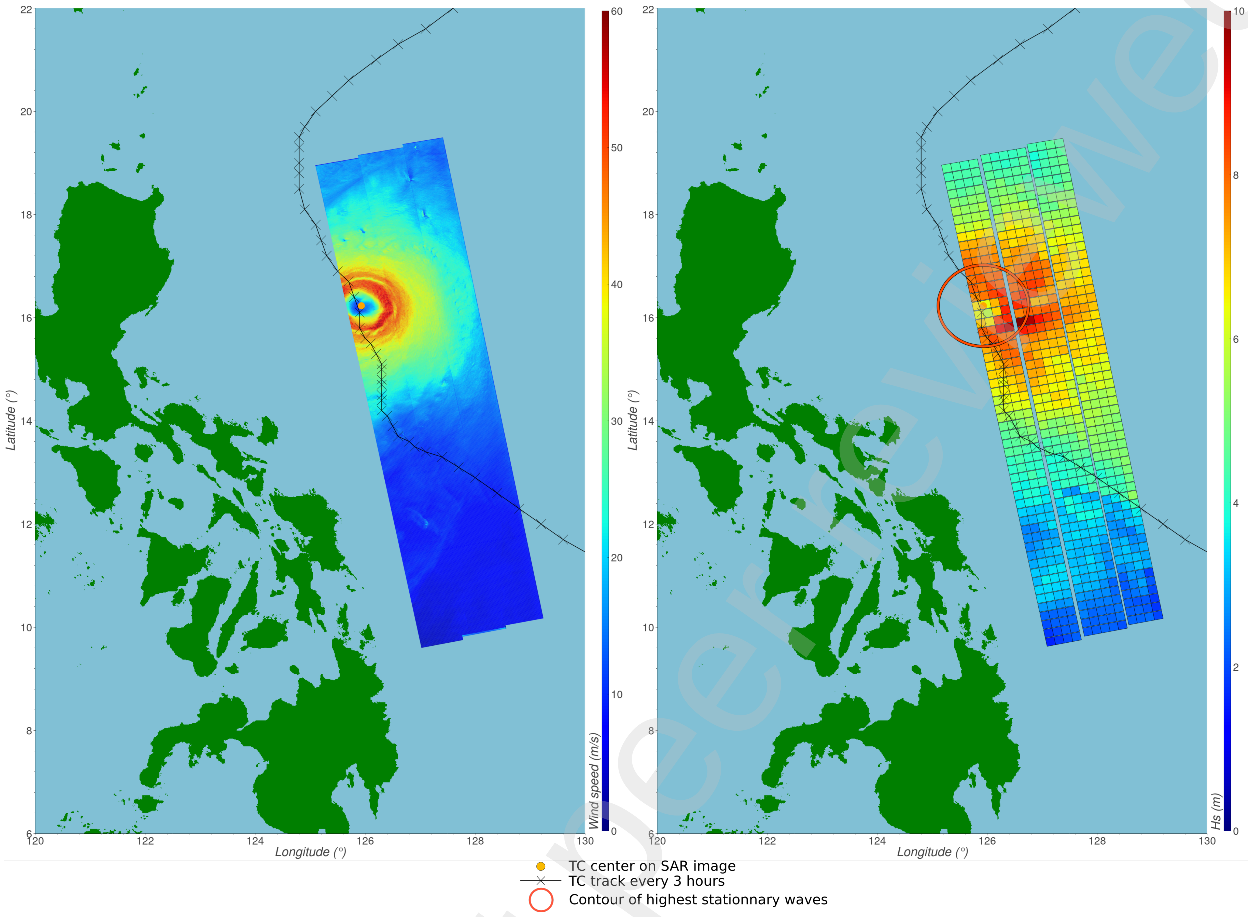

Fig. 18. (left) Sentinel-1B SAR wind speed observation for TC Surigae on 2021-04-20 at 9 AM. (right) SAR measured significant wave height. The red circle provides the location of the longest waves generated by a stationary TC. Its color follows the significant wave height color scale.

image over TC Surigae, a spectral analysis is performed to locally infer a well detected peak swell system on the right hand side of the TC. Using its direction, a ray-path is determined, along which wave packets propagate according to the group velocity determined by the estimated peak wavelength. The spatio-temporal propagation can then be evaluated, and shown to cross a descending Sentinel-1 WV swath, a SOFAR drifting buoy, and a CFOSAT SWIM ascending swath, respectively. Estimates of both wavelengths and directions from SAR are found to be consistent with these independent observations. This demonstrates the synergies between different observing systems. In particular, combined observations will lead to more precise quantification of directional spreading and dissipation properties of TC swell systems.

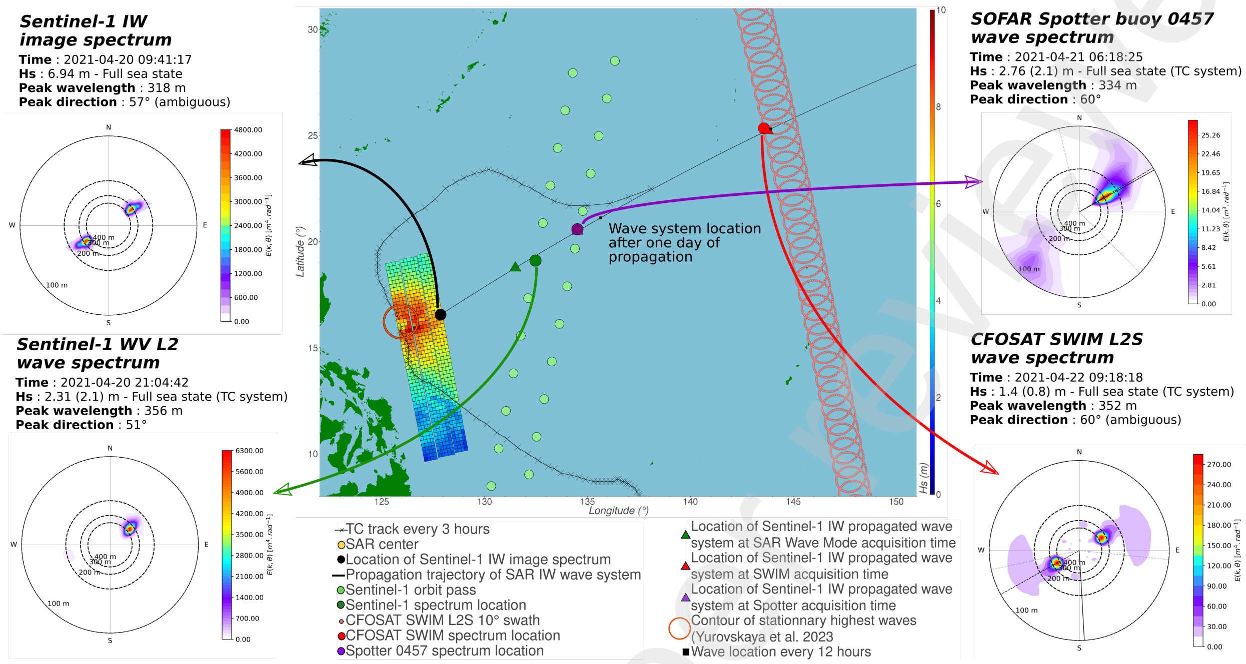

Fig. 19. Analysis of a swell system induced by TC Surigae on 2021-04-20 at 9 AM, and observed later at multiple locations during its propagation by different platforms. (Middle) Map with location of observations, significant wave height field from Sentinel-1 IW large swath, Sentinel-1 and CFOSAT orbit passes. Top left: Sentinel-1 image spectrum (black circle on map). Bottom left : Ocean wave spectrum from Sentinel-1 WV imagette Level-2 OCN Copernicus/ESA product (Chapron et al., 2001) (after 12 hours of propagation, green circle on the map). Top right : Ocean wave spectrum from SOFAR Spotter drifting buoy 0457 (Houghton et al., 2021) (after 21 hours of propagation, purple circle on the map). Bottom right : Ocean wave spectrum from CFOSAT SWIM L2S Ifremer product (Hauser et al., 2020) (after 48 hours of propagation, red circle on the map).

4.2.3. *Tropical cyclones wakes*

Numerous studies have explored the ocean's response to TC passages. In their wake, TCs generate a variety of effects that contribute to intense vertical mixing through surface stirring, shear at the base of the mixed layer, and convective cooling. These processes are typically characterized by the near-instantaneous emergence of a surface cold anomaly, which is sensitive to pre-existing temperature and salinity stratification. Known as the cold wake, this response is, in the open ocean, generally of baroclinic nature (Ginis and Sutyrin, 1995). Besides a significant drop in temperature (Bender et al., 1993; Chiang et al., 2011), a TC oceanic wake can exhibit a sea level trough of up to several tens of centimetres (Ginis, 2002; Walker et al., 2014; Kudryavtsev et al., 2019; Combot et al., 2024), and an upsurge in salinity of an order of magnitude greater than the average variability in the tropics (Sun et al., 2021; Reul et al., 2021). At the same time, a TC cold wake can also feature a large Chlorophyll-a bloom, visible through optical sensors (Lin et al., 2003; Babin et al., 2004).

However, interpreting the ocean response is not straightforward. It requires a multi-frequency and multi-modal approach to collect, assemble and capture the main environmental conditions, i.e. cyclonic forcing and pre-storm ocean stratification, into a coherent framework (Black et al., 2007; Pun et al., 2011; Reul et al., 2014). Key parameters that control TC impact on the ocean often include: $V_{\rm fm}$ (Lloyd and Vecchi, 2011) and f (Shay, 2009), which both reflect the efficiency of the mixing (D'Asaro et al., 2014) and are reported in reanalysis tracks. Stratification parameters such as the depth of the mixing layer (Price, 1981; Vincent et al., 2012; Mei et al., 2013), temperature and salinity gradients (Reul et al., 2014; Pivaev et al., 2022) or the Brunt-Vaisala frequency (N1) (Geisler, 1970; Kudryavtsev et al., 2019) require in situ measurements. Various metrics characterizing the surface wind field geometry and intensity, like $R_{\rm max}$ and $V_{\rm max}$ are also necessary (Geisler, 1970; Ginis and Sutyrin, 1995; Vincent et al., 2012; Kudryavtsev et al., 2019).

In particular, Kudryavtsev et al. (2019) proposed a scaling law for anticipating the geostrophic SSHA signature, corresponding to the dominant mode of response (i.e. baroclinic mode). This scaling law combines $V_{\rm max}$, $R_{\rm max}$, $V_{\rm fm}$ and N_1:

$$\mathrm{SSHA} = 6.9.10^{-6} V_{\rm max}^2 \left[\frac{R_{\rm max} N_1}{V_{\rm fm}}\right]^{1.041}. \tag{9}$$

To overcome the shortcomings of best track estimates of these parameters, the SAR $R_{\rm max}$ and $V_{\rm max}$ estimates were first demonstrated to be essential to anticipate the post-storm SSH anomaly (SSHA) signatures. Initially illustrated on a few TC cases (Combot et al., 2020b), these results were then verified quantitatively using a larger spatial sample of 300 SAR images from the Sentinel-1A/B and Radarsat-2 missions, generalized to all basins (Combot et al., 2024). This latest study not only explained the distribution of wake amplitudes for the first time, but above all demonstrated the importance of precise near-core description of the cyclonic forcing to explain the variability of the observed signatures. The absence of SAR implies a loss of more than 30% in the variability explained.

Fig. 20 describes this extensively-applied methodology, using the example of cyclone Mawar, captured several times (6) by the C-band SAR constellation in 2023. On 26 May 2023 at 20:52 UTC, Mawar had a $V_{\rm max}$ and $R_{\rm max}$ around 71 m.s-1 and 37.5 km, respectively as estimated from the SAR observations using the method from Mouche et al. (2019), and a translation speed of 7 m.s-1, as provided by IBTrACS (Knapp et al., 2010). For each SAR image, the pre-storm Argo vertical profiles and the post-storm altimetry observations were co-located, as illustrated in Fig. 20 (left panel). Here, Mawar moved over a stratification of 0.0133 s-1 reported by Argo float and caused a wake of the order of 28 cm as measured by the available altimeters. For this case, the scaling law (Eq. 9) prediction of a 30 cm through is again found very consistent with the observation (see Fig. 20 caption). Fig. 20 (left panel) further illustrates the recent progress in interpreting the response of the oceans (Zhang et al., 2024; Combot et al., 2024), by bridging high-resolution measurements from altimetry missions and the SAR constellation, in which the Sentinel missions have played a pioneering role (Combot et al., 2020a).

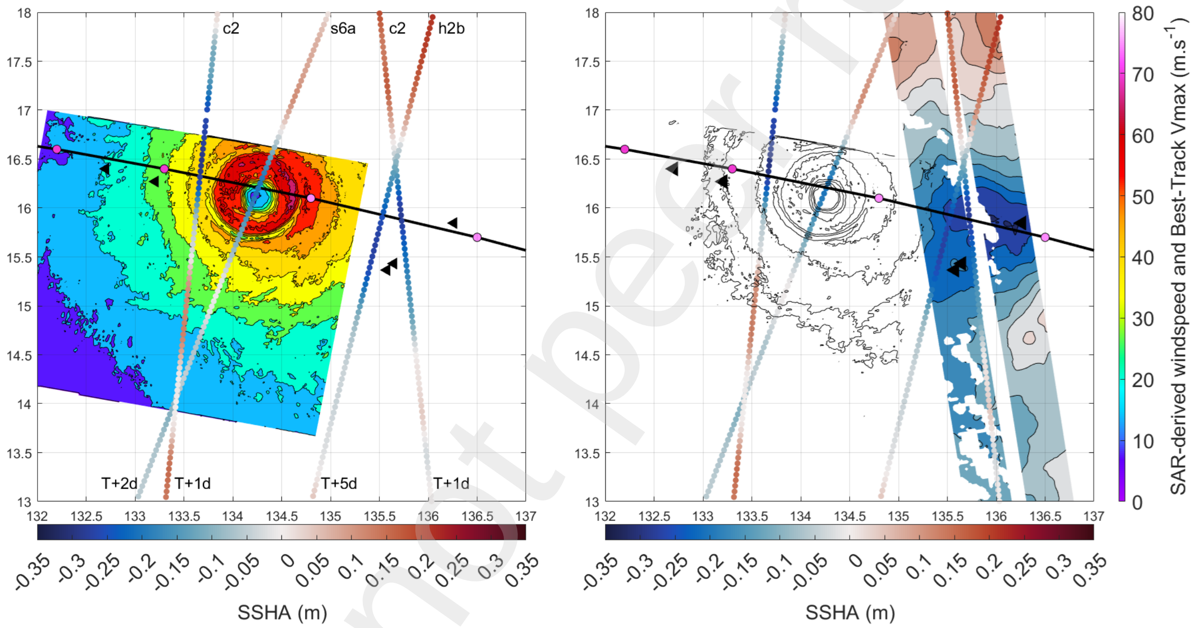

Fig. 20. (left) Illustration of the classical multi-platform framework, based on Combot et al. (2024) to analyse the TC-induced ocean response. (right) Illustration of the new capability of the surface ocean topography measurements from the 2D altimeter KaRIN of SWOT satellite. The analysis is centered around a SAR image, here a RCM acquisition of TC Mawar, for which the other observations are co-located in time and space. Black triangles depict the distribution of Argo floats in the vicinity of the R_{34} kt, over a two-week period prior to the storm. Most intense SSHA from the altimeter constellation are selected around 1 to 7 days after the TC (c2: Cryosat-2, s6A: sentinel-6a, h2b: haiyan-2b). They are derived by subtracting a pre-storm average of the daily interpolated CMEMS product from the post-storm L3 altimeter measurements, while the maximum trough associated to this case is directly assessed from the sole use of post-storm track, this operation is made for graphical purposes. The closest SWOT track for the SAR image of Mawar is displayed on the right panel. SSHA induced by the Typhoon is derived by deducting from each post-storm measurement, a two-week pre-storm average, using the 1-day repetition cycle of the satellite. Here, only the day (T+2 days after Mawar) with the maximum response (31 cm) is selected.

Today, the SAR constellation occurs within the so-called ocean altimetry golden era. Currently, up to 7 nadir-looking altimeters are operating, now augmented by the SWOT (Surface Water and Ocean Topography) 2D mapping of SSH measurements. Launched at the end of 2023, SWOT is indeed equipped with a groundbreaking new Ka-band Interferometric radar (KaRIN), capable of measuring the topography of the ocean surface over swaths about 60 km wide. The combined use of these data with SAR and Argo measurements can now uniquely allow for simultaneous highly resolved description of forcing, the vertical structure of the ocean and its response, as suggested by Fig. 20 (right panel). The same order of magnitude is observed for the wake signature, with an estimate of 31 cm, very close to the predicted value. SWOT further captures the wake geometry that can be directly connected with the vortex structure. For instance, the e-folding radius of the wake (Radius of SSHA $\min/e^1$), which circumscribes the region with the strongest sea level response, is of the order of two times the $R_{\max}$ (70 km), close to the R_+ (72km) parameter (see definition below section 4.2.5) estimated with the methodology from Avenas et al. (2024b). Those different metrics are still to be put in systematic conjunction, on a larger dataset, to bring new insights about the air/sea interactions under extremes. But SAR and SWOT observations certainly foreshadow new strategies for the cross-analysis of the structure and the dynamics of both wake and surface wind field.

4.2.4. Tropical cyclones air-sea interactions

First documented by Katsaros et al. (2000a), high-resolution TC SAR observations have characteristic streaky patterns with km-scale separation that are approximately aligned with the mean azimuthal wind. These are signatures of tropical cyclone boundary layer (TCBL) roll vortices, which play a key role in the downward flux of momentum (Morrison et al., 2005; Zhang et al., 2008). Foster (2005) developed a stratification-dependent model for the formation and nonlinear equilibration of these rolls. Basic characteristics (wavelength, orientation and strength) of these rolls depend on the mean TCBL shear profiles, which can be inferred from the SAR surface winds using a nonlinear TCBL model (Foster, 2009). The boundary conditions for Foster (2009) are the wind at or just above the TCBL top, and the SAR-derived sea-surface kinematic stresses, τ/ρ. The mean wind profiles depend sensitively on the assumed vertical profiles of the turbulent eddy viscosity, $K(z)$. This latter parameter is central to modeling local, down-gradient, turbulent fluxes and is a focus of the boundary layer parameterizations used in TC numerical models.

The wind at the top of the TCBL is assumed to be in approximate gradient wind balance, which depends primarily on the local radial gradient of the surface pressure. Foster (2017) adapted

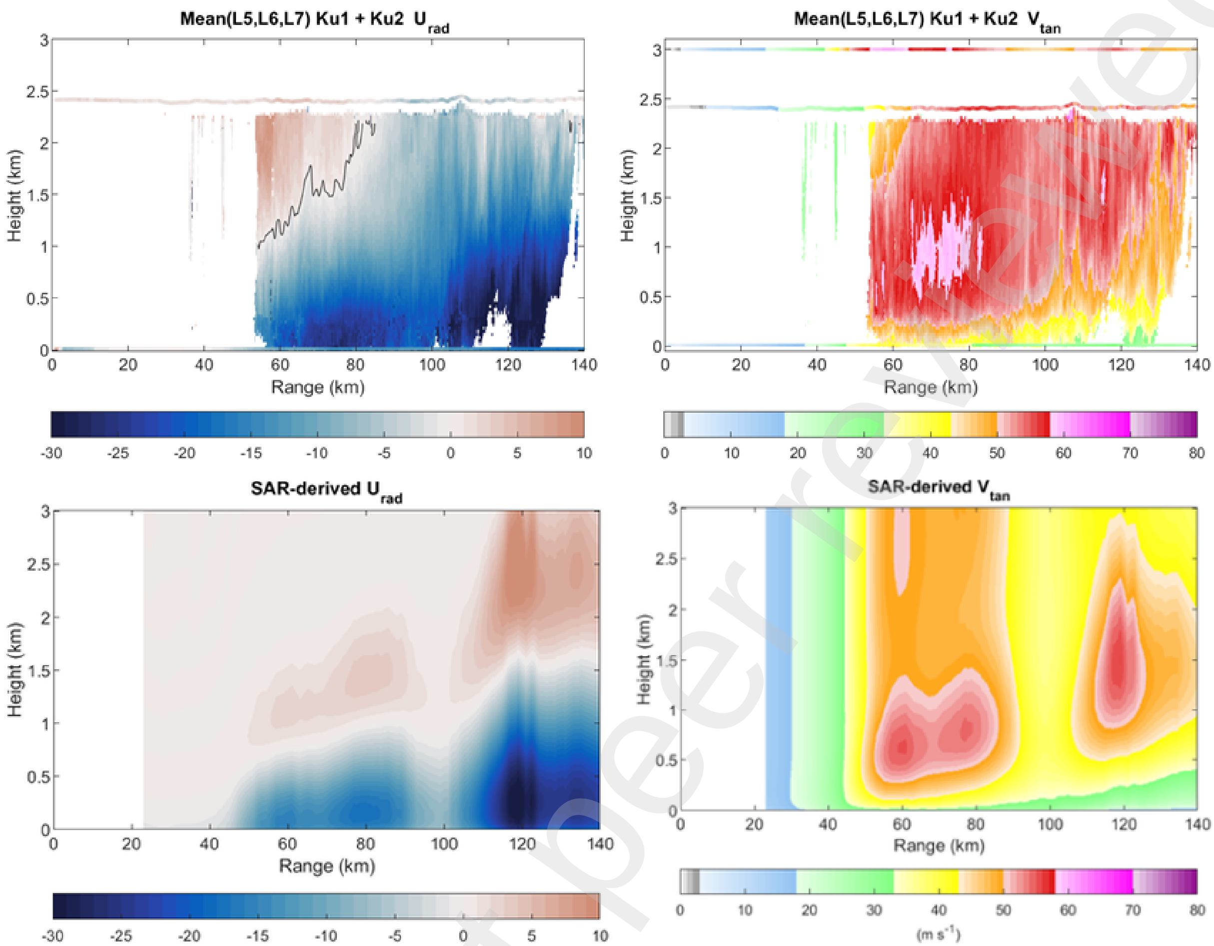

Fig. 21. Hurricane Larry on September 7, 2021. IWRAP TCBL wind profiles from P-3 radial legs closest to the SAR overpass. (top left) Radial, (top right) Azimuthal. SAR-derived TCBL winds (bottom left) Radial, (bottom right) Azimuthal.

to SAR TCBL a methodology for retrieving surface pressure patterns from swaths of satellite scatterometer wind vectors (Patoux and Brown, 2002; Patoux et al., 2003). Surface wind vectors are found by translating ECMWF forecast model surface wind directions to the SAR-estimated surface circulation center and applied to the SAR surface wind speeds. The gradient wind speed as a function of range and azimuth from the storm center, $V_g(r, \phi)$, is calculated from the derived pressure pattern (Foster, 2017). The inertial stability time scale needed to scale the height in both the TCBL mean wind and roll models and in the eddy viscosity parameterization is also calculated from the surface pressure pattern. Using a range of reasonable $K(z)$ parameterizations that scale with the surface stress, mean flow profiles are calculated at each (r, ϕ) and used to predict the SAR-derived TCBL roll orientations (Foster, 2005, 2009). Minimizing the mean difference between the predicted and observed roll directions across the SAR image then selects the best K_z parameterization.

The Ocean Surface Winds team at NOAA/NESDIS/STAR coordinated a P-3 mission with a Sentinel-1B overpass of hurricane Larry on September 7, 2021, 21:48 UTC. The NOAA Gulf-stream G-IV (G-IV) aircraft was conducting environmental soundings. The P-3 deployed 4 drop-sondes in the center and high wind regions and the G-IV dropped seven sondes that landed in the far field of the SAR image during the P-3's time on station. The P-3 also acquired flight-level (2400 m) data, derived surface pressure, and SFMR surface wind speeds. The downward looking, conical scanning Imaging Wind and Rain Airborne Profiler (IWRAP) radar (Fernandez et al., 2005) was operating on this flight. IWRAP provides high resolution vertical wind profiles within the TCBL (Sapp et al., 2022). IWRAP provides horizontal wind vectors every 150 m along the P-3 flight path with a vertical spacing of 30 m down to approximately 50 m (conditions permitting) above the sea surface. The P-3 made three radial penetrations at or near the SAR overpass time on the front-right side of the storm, and the aircraft data are mapped to the SAR image time by a constrained adjustment of the first guess storm track. The cost function is the RMS difference between SFMR and SAR wind speed in the inner core (see Fig. 6 for comparison). In this case, the SAR-derived surface pressure pattern matches the drop sonde surface pressures and pairwise pressure differences with 2 hPa RMS (not shwon). The best roll orientation RMS is found when the assumed $K(z)$ maximizes nearer to the sea surface than in standard parameterizations, which is consistent with recent studies by Chen et al. (2021).

Fig. 21 (top panel) show the IWRAP radial and azimuthal wind radius height sections along the radial penetration at the overpass time. Corresponding SAR-derived radial and azimuthal winds are sampled using the adjusted P-3 flight track as shown in Fig. 21 (bottom panel). IWRAP finds two inflow maxima between 60 and 80 km radius and one near 120 km. These features are also seen in the SAR-derived winds. IWRAP and SAR agree on an inflow minimum near 100 km, and also capture super-gradient azimuthal winds at or above the inflow maxima, between 60 and 80 km. Super-gradient winds are the result of nonlinear TCBL dynamics (Kepert and Wang, 2001) that are included in Foster (2009). Overall, the SAR-derived inflow layer is somewhat shallow, related to how quickly $K(z)$ decreases above its peak value.

IWRAP winds show evident km-scale modulation across the depth of the TCBL. The suspected TCBL roll signature is extracted from 10 km segments of radial passes that are rotated by the SAR-derived roll inflow angle, and red noise spectra estimated. Wavelet spectra are then used to identify significant local wave scales that fall into separate groupings above and below a threshold comparable to the TCBL depth. The roll signal is reconstructed using only the significant signals in the longer wavelength group. An example near r = 80 km is shown in Fig. 22 (top panel).

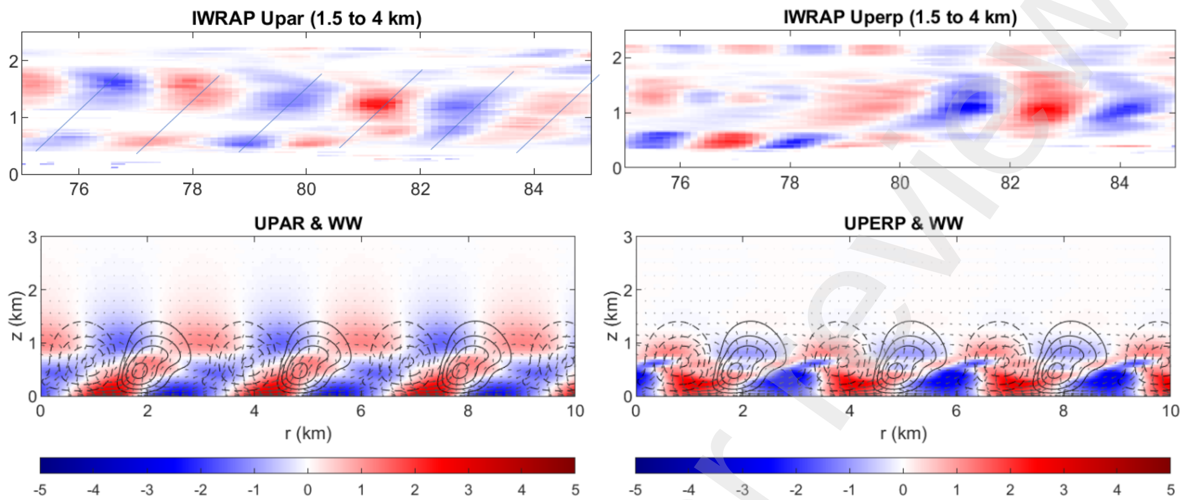

Fig. 22. TCBL roll signature extracted from IWRAP winds. (a) Upar; (b) Uperp. Calculated TCBL rolls using mean wind and eddy viscosity profiles derived from IWRAP and SAR. (c) U_{par}; (d) U_{perp}. Color scale in m s-1. Calculated vertical velocity included on bottom panel with 0.5 m s-1 contours. Vectors show calculated overturning roll circulation (U_{par}, w).

Roll velocity components are called ($U_{\mathrm{par}}, U_{\mathrm{perp}}, w$). The overturning roll circulation is (U_{par}, w) and it is in a vertical plane that is approximately oriented along the radial direction. U_{perp} is the along-roll velocity perturbation and is approximately along the azimuthal direction. Examination of U_{par} shows that the overturning roll circulation is tilted against the mean shear, which is the signature of shear-generated coherent structures. Fig. 22 (bottom panel) shows the nonlinear solution from Foster (2005). In the SAR-derived U_{par} and U_{perp} plots are the calculated vertical velocity (contours) and overturning (U_{par}, w) wind vectors. The IWRAP and SAR-derived secondary circulation magnitudes are approximately the same and at the same 5° inflow angle. The predicted and observed tilting of the rolls are comparable. Furthermore, the relative phasing between the U_{par} and U_{perp} components is the same in both IWRAP and SAR. The enhanced downward flux of azimuthal momentum induced by the rolls is evident in the U_{perp} plot. The most noticeable difference is that SAR-derived wavelength is longer than seen in IWRAP. While there is room for improvement, SAR-derived mean wind and roll circulations derived using only SAR information agree reasonably well with those measured by IWRAP.

4.2.5. *Tropical cyclones dynamics*

With Sentinel-1 SAR acquisitions more systematically collected, the wind structure of TCs (see section 4.2.1) is now more precisely estimated at different stages of their development and at high-resolution. Documenting the inner- and near-core regions where important processes take place, these unprecedented observations provide an opportunity to study the TC dynamics. In particular, few studies recently used the SAR high-resolution acquisitions to investigate the most commonly assumed physical and dynamical constraints on the wind structure. As a common thread, Fig. 23 presents the two-dimensional wind speed estimates (left panel) and corresponding wind profile (right panel) from a SAR acquisition of TC Maria on 21 Sep 2017 at 22:44 UTC, introducing parameters that are important to the TC dynamics, as discussed below.

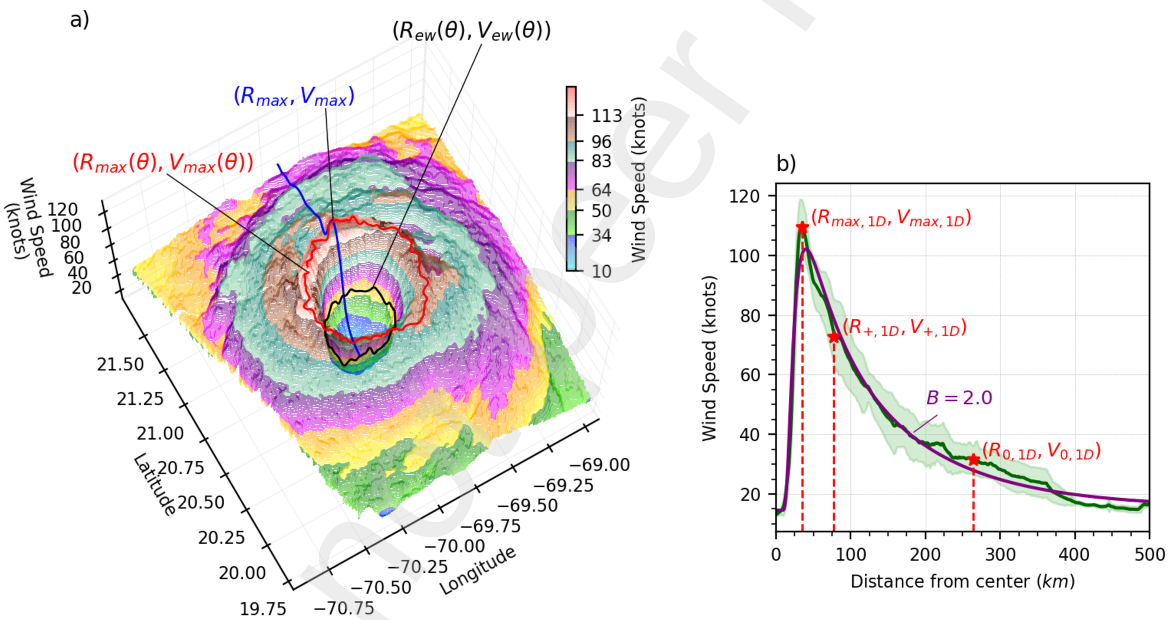

Fig. 23. Summary of SAR-measured parameters related to TC internal dynamics illustrated on the Sentinel-1A acquisition of TC Maria on 2017/09/21, 22:44:21. a) 2D wind field with asymmetric parameters as introduced by Vinour et al. (2021). 3-dimensional shading indicates the magnitude of estimated surface wind speed in knots (cf. colorbar and z-axis). Also shown are the azimuthal distributions of radius of maximum wind in red ($R_{\max}(\theta)$,$V_{\max}(\theta)$) and eyewall radius in black ($R_{\text{ew}}(\theta)$,$V_{\text{ew}}(\theta)$), and the radial profile corresponding to the maximum wind location ($R_{\max}$,$V_{\max}$) in blue. b) Corresponding azimuthal-mean wind speed profile. The mean SAR profile is indicated by the thick green line, and the green shading indicates the standard deviation. The least-squares fitted Holland profile is shown by a purple thick line, annotated with its corresponding B parameter. Dotted red vertical lines and star markers indicate characteristic radii used to describe internal dynamics and their associated wind speed: azimuthally-averaged maximum wind radius ($R_{\max,1\text{D}}$,$V_{\max,1\text{D}}$); estimated radius of large vertical velocities ($R_{+,1\text{D}}$,$V_{+,1\text{D}}$); estimated radius of vanishing outflow radial velocities ($R_{0,1\text{D}}$, $V_{0,1\text{D}}$) as introduced by Avenas et al. (2024b).

TCs are intense rotating systems, and most of their dynamics can be interpreted using angular momentum and its conservation:

$$M = rv + 0.5fr^2 = \text{cst}, \tag{10}$$

with r the distance from TC center and v the tangential component of the wind speed.

Air parcels are classically assumed to conserve their absolute angular momentum along their outflow trajectory, at least during the most intense phases of the life cycle (Shutts, 1981; Emanuel, 1986). This fundamental property links the maximum wind speeds at the top of the inflow layer to the outflow layer and allows to diagnose the TC dynamical state from SAR high-resolution measurements. Closer to the surface, angular momentum is presumably no longer conserved because of frictional effects. However, an argument of potential vorticity conservation (Riehl, 1963) may be advanced to characterize the frictional losses:

$$C_d r v^2 = \text{cst}, \tag{11}$$

where C_d is the drag coefficient. Recently, this relationship was reexamined using SAR azimuthally-averaged wind profiles (Avenas et al., 2023, 2024b), confirming its validity or at least a weak variation of C_d in Eq. 11. This further suggests that the wind decay (i.e the B Holland parameter, see right panel on Fig. 23 encodes the variations of the drag coefficient C_d. As a consequence, instantaneous knowledge of a high-resolution SAR wind profile informs on the turbulent momentum exchanges and losses occurring in the inflow layer.

Following Eq. 10, a high-resolution SAR observation allows to indirectly characterize the effective size of the system R_0, where R_0 is the radius of vanishing wind in the outflow layer. Indeed, writing the absolute angular momentum conservation from $R_{\max}$ in the inflow layer to R_0 in the outflow layer yields

$$\sqrt{2\mathcal{R}o_{\max}} = \frac{R_0}{R_{\max}}, \tag{12}$$

where the maximal Rossby number is defined as $\mathcal{R}o_{\max} = \frac{V_{\max}}{fR_{\max}}$. R_0 may thus be estimated with SAR once $R_{\max}$, $V_{\max}$, and f are known, *e.g* from azimuthally-averaged wind profiles. Under an axisymmetric assumption, Avenas et al. (2024b) then integrated the equations of conservation of momentum, mass, and energy, over a cylindrical volume constrained by the effective size R0 and the height of the system. This leads to an equation describing the integrated kinetic energy balance based on the assumption that the heat gained by the system is proportional to the vertical velocities due to Ekman pumping in the boundary layer. The study corroborated these upward motions are significant in between the center and a radius R_+ defined as

$$\omega_z(R_+) = 5f, \tag{13}$$

with $\omega_z(r) = \frac{1}{r}\frac{\partial m}{\partial r}$ the relative vorticity and $m = rv$ the relative angular momentum. Importantly, this original analysis framework of the high-resolution SAR observations allows us to jointly estimate the characteristic scales R_+ and R_0 (see the right panel of Fig. 23) - beyond the sole documentation of the TC wind structure - that were shown to be crucial for the TC kinetic energy balance. Written in terms of the shape parameter B_s and $\mathcal{R}o_{\max}$ the integrated kinetic energy balance is further reduced to

$$V_{\max}^2 = \frac{U_c^2}{3\sqrt{2}}\sqrt{B_s \mathcal{R}o_{\max}}, \tag{14}$$

where U_c is a velocity scale characterizing the vertical profiles of heating and temperature. Referring to Eq. 11 for the most intense events, the drag coefficient appears to saturate or decrease, depending on B_s, with wind speed in the region between $R_{\max}$ and R_+.

Avenas et al. (2024a) further examined the consistency of successive SAR observations and the use of an analytical model for the azimuthally-averaged wind profile evolution. Along characteristics, the angular momentum conservation simplifies to

$$\frac{\partial m}{\partial t} + u\left(\frac{\partial m}{\partial r} + fr\right) + \lambda m = 0, \tag{15}$$

with u the tangential component of the wind speed and λ a linear friction term that can be further reduced to depend on solely one scalar parameter. The radial circulation u is not known, but can be prescribed assuming a particular inflow angle distribution. Equation 15 then allows to efficiently diagnose short-term changes in the TC wind profile. Although conducted with a limited number of observations, their study showed that an instantaneous SAR acquisition and subsequent knowledge of the characteristic scale R_+ can inform on the short-term evolution of the wind structure, and can help to constrain u and λ functions, refining frameworks such as Eq. 15.

One of the limitations of these studies is that they rely on an axisymmetric assumption. Vinour et al. (2021) conducted an extensive statistical study of SAR-observed high-resolution TC symmetric and asymmetric properties. The authors introduced new SAR-derived parameters to describe the TC wind field at high resolution, including its 2D structure: the shape of the azimuthal mean profile (green profile in the right panel of Fig. 23) inside the eyewall (between the center of the TC and $R_{\max}$) and the near core (between $R_{\max}$ and $3R_{\max}$), the distribution of power spectrum energy in azimuthal distributions of the radius of the eyewall $R_{\mathrm{ew}}(\theta)$ and maximum wind radius $R_{\max}(\theta)$ (resp. black and red line in the left panel in Fig. 23). Joint measurements of both the axisymmetric structure (profile shape in the eyewall) and asymmetric variability (high wavenumbers explained variance in the eyewall and maximum wind ring) are shown to be related to the TC intensity and intensification rate, and can help to dissociate intensifying and decaying phases of the TC.

Other signatures often apparent in the SAR images are rainbands. This spiral pattern is related to the effective frictional effects occurring in the boundary layer to control its orientation departure from the tangential wind direction (Yurchak, 2007, 2024). Further investigations on how such an information can relate to Eq. 15 are yet to be done. Encouraging studies already report on the occurrence of TC rainbands derived from SAR images and examine how they could be used to characterize the TC life cycle (Zheng et al., 2024).

More generally, while we focus on the monitoring of TC through estimates of ocean surface wind speed and associated radii, other parameters that can be extracted from a SAR acquisition may be used in the future to assess the TC dynamics: wind direction and rolls orientation, the evolving rolls sizes with distance to the perturbation center, rain and the location and amplitude of convective cells, the local wave field, and possibly the local surface current.

5. Perspectives

If this first decade of Sentinel-1 data has certainly contributed efficiently to TC monitoring, allowing for scientific and operational applications, it has also highlighted several issues and opened new perspectives. First, the existing products can be strengthened and extended to other geophysical variables. Additionally, the new capabilities of future SAR missions will address some of the challenges we have identified. This section presents perspectives for algorithm development and future SAR missions.

5.1. Algorithms developments

To date, the TC wind products and associated vortex parameters delivered by NOAA and archived in the CyclObs database primarily focus on the ocean surface wind speed inferred from the signal intensity measured by Radarsat-2, Sentinel-1, and Radarsat Constellation missions. When compared to airborne Stepped Frequency Microwave Radiometer (SFMR) measurements, it has already been demonstrated how Sentinel-1 SAR measurements uniquely capture inner TC core characteristics, to often provide independent measurements of maximum wind speed and radius of maximum wind (Mouche et al., 2019; Combot et al., 2020a). These measurements are used in several operational TC forecasting centers (see section 4.1). Multiplying the number of acquisitions, a paradigm shift is taking place. It enables to cover more situations as well as to collect more and new types of concurrent data or model outputs to revisit what has been done so far. In particular, a key element is certainly the provision of these estimated surface winds with more advanced quality flags, which are essential to help non-SAR experts assess the reliability of the products. Following recommendations from the operational community, a quality flag for the wind speed is still needed. This flag should particularly include the detection of intense rainfalls.

As shown in Fig. 2 and discussed by (Mouche et al., 2019) in the case of Irma TC, the rain signature seems to be highly correlated with the most intense rainfall and to impact the backscattered signal locally. SAR high-resolution capabilities directly offer straightforward means to compare and evaluate how retrieved parameters depend on differing spatial resolution, from high O(1-3 km), medium O(10-20 km) to low O(30-60 km) spatial resolution. Remarkably, close consistency is generally found at low resolution between rain-free L-band brightness temperature measurements and the C-Band cross-polarized NRCS signals (Zhao et al., 2018). Studies can thus further dwell on such results to analyze the contrast between average NRCS measurements and NRCS texture at very high-resolution O(1-3 km), to locate areas with spurious signatures, likely associated with hydro-meteors, localized convective events and/or intense precipitations. More systematic co-locations between satellite SAR and ground-based weather Doppler radar measurements can be further accumulated, especially given the recent increase in available SAR acquisitions. Accordingly, more precise identification shall be performed to help efficiently link these observations, revisit previous studies limited in data Zhao et al. (2021) and propose advanced dedicated methods - currently limited to moderate winds - to provide accurate rain rate estimates from SAR measurements over extremes (Colin and Husson, 2025). However, as noted by Météo-France experts from the TC Centre at La Réunion, there are situations with suspect wind estimates, often observed in cases of low-intensity storms and not necessarily exhibiting significant and local change in the high-resolution texture of NRCS. These cases are still largely unexplained and may represent a challenge for flagging.

Mentioned in section 3.3.1, extensive research work is also directed to possibly extract reliable wind direction from SAR measurements. From a scientific point of view, information on the wind direction in the TC marine atmospheric boundary layer would be necessary to more accurately

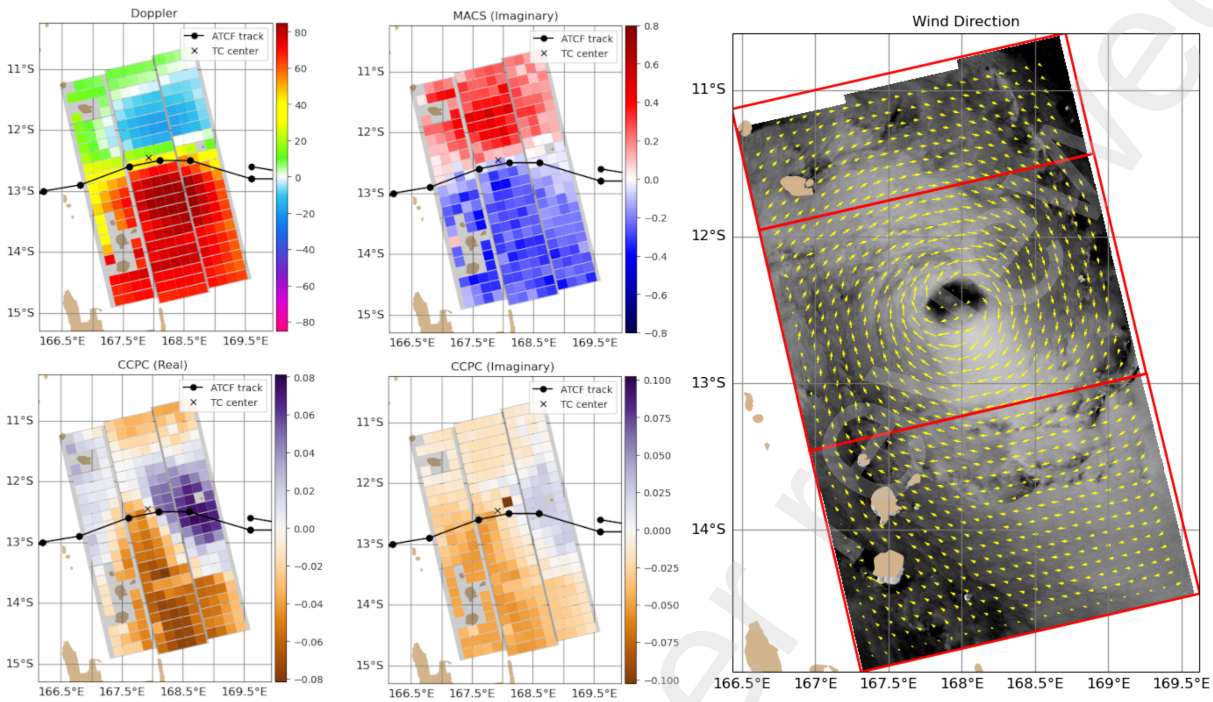

Fig. 24. Illustration of parameters not used in the operational products that could be used to further constrain the wind inversion. Application to TC Donna (2017). Left panel : Ensemble of SAR-derived radar parameters that derived from Level-1 SLC SAR data. Top left: Doppler in Hz. Top middle: Imaginary part of the MeAn Cross-Spectra. Bottom left: Real part of the co-cross-polarization coherence. Bottom middle: Imaginary part of the co-cross-polarization coherence. Right panel: SAR roughness and SAR derived wind direction combining the two polarization channels

quantify the radial advection of angular momentum, thus helping to better evaluate the system dynamics, for instance, through simple energetical equilibrium considerations (e.g. Avenas et al. (2024b)) or evolution models (e.g. Avenas et al. (2024a)). Yet, SAR only measures a single antenna NRCS field. A local wind direction estimate over a given patch, often uses the intensity signal texture, possibly at different resolution (from hundreds of meters compared to the kilometer-scales). This has been documented by Horstmann et al. (2013, 2015) in the case of TCs observed with RS2. In particular, as for the wind speed retrieval algorithm, the recent use of co- and cross-polarization channels has proven to be advantageous, particularly in the context of very intense storms and areas with long swells that can dominate signal modulation in co-polarization (Fan et al., 2020). There are still open questions regarding the characterization of textures related to ocean surface wind direction. In some local patches, estimates clearly relate to rolls, almost ubiquitously occurring in the marine atmospheric boundary layer and often detected by SAR (Foster, 2005; Morrison et al., 2005). Overall, a first version of the ocean surface wind directions directly derived from SAR measurements, maybe not over the whole TC region, may thus be estimated, providing users with this information as part of the SAR TC products. An example of SAR-derived direction obtained from texture analysis, combining both co- and cross-polarization channels, is presented in the case of TC Donna (2017) in Fig. 24 (right panel).

Moreover, a key element of the Sentinel-1 mission payload data ground segment is to systematically provide Level-1 data in Single Look Complex (SLC) in addition to the Ground Range Detected (GRD) processing level. Access to SLC data enables us to investigate the use of other radar parameters beyond just intensity to solve the inverse problem. Indeed, SAR measurements also explicitly include information on the scatterer's displacements through the so-called geophysical Dopper shift measurement (Chapron et al., 2005). Initially intended to map ocean surface current signatures, the primary driver of this frequency shift, especially under extreme conditions, is actually the sea state and wind-wave motions. Mouche et al. (2012) already investigated how this dependency could be used to further constrain the wind inversion scheme. It was shown that, when combined with the co-polarized intensity signal, it leads to better wind direction estimates in complex situations, such as atmospheric fronts or low-pressure systems. Recent studies confirm that the local sea state approximated by the wind speed remains a robust proxy to explain the Doppler measurements estimated from Sentinel-1 C-band SAR in VV polarization over TC (Yurovsky et al., 2024). In Yurovsky et al. (2024) efforts are directed to break down and discuss Doppler into different contributions from wind and TC-generated ocean waves and ocean surface current. This opens perspectives to upgrade the wind vector inversion scheme, but also to investigate the feasibility of a joint wind, waves and current retrieval. The Doppler in co-polarization (VV) measured by Sentinel-1 is presented in Fig. 24 (top left) for TC Donna (2017). As observed, the change of sign is consistent with the wind flow wrapping around the TC center (see right panel). The Doppler maximum is also found in the area of maximum NRCS (i.e. wind speed). Furthermore, Doppler information can be enriched using the image cross-spectra technique (Engen and Johnsen, 1995; Chapron et al., 2001). This technique entails a spectral analysis of two sub-images of the same scene, acquired with a short temporal baseline (typically less than 1 second). Demonstrated by Li et al. (2019) using Sentinel-1 Wave Mode data, a new parameter termed IMACS (for the Imaginary part of the MeAn Cross-Spectra) robustly trace the displacements of the wind waves, wavelengths O(20 m), traveling the range direction. IMACS estimates showed dependency to the wind speed and direction, complementary to the NRCS and close to the geophysical Doppler shifts. IMACS in co-polarization (VV) measured by Sentinel-1 is presented in Fig. 24 (top middle) for TC Donna (2017). The change of sign is consistent (anti-correlated) with the wind flow wrapping around around the TC center (see right panel) and with the Doppler (top left panel). Finally, Zhang et al. (2012) and then Longépé et al. (2022) investigated the benefit of having two simultaneous acquisitions with phase-preserving information in co- and cross-polarization through the co-cross-polarization coherence (CCPC) radar parameter computed from respectively Radarsat-2 and Sentinel-1 Level-1 SLC data. CCPC is found complementary to the signal intensity and the geophysical Doppler shift (Longépé et al., 2022). This is illustrated in the case of TC Donna (2017) in Fig. 24 (left and middle bottom panels). In short, the variation of the Doppler (or IMACS), the signal intensity and the CCPC parameters with respect to wind speed and direction are different. Having the three measurements simultaneously adds significant constraints to the cost function. When using the Doppler (or IMACS) in co-polarization and the CCPC, the equation of the cost function (Eq. 3.3.1) is augmented with two terms and the needs of an auxiliary model should decrease. In addition to providing a better estimate of both the ocean surface wind speed and direction, the minima of the cost function shall also indicate the consistency of these measurements with respect to a given wind vector solution. In the presence of non-wind signature in these radar quantities we can expect an increase of the minima that could be used to define a quality flag.

Beyond efforts to more consistently derive local wind vector and rain (or rain flag), it must be recalled here that the high-resolution observations of the sea surface with a synthetic aperture radar certainly contain more information to be quantitatively retrieved. Texture, associated to the surface wind variations, encodes information on the stability in the marine atmospheric boundary layer. Encouraging efforts have been demonstrated to relate Sentinel-1 WaVe mode data, exhibiting signatures of rolls and micro-convective cells, to stability parameters, such as the Richardson number Stopa et al. (2022) or the Obukhov length (O'Driscoll et al., 2023). Such systematic studies remain to be extended to wide swath acquisition and extreme situations. Foster (2013) analyzed the ocean surface wind divergence and wind stress curl, estimated by a wide swath Radarsat-2 acquisition over TC Katrina, to discuss possible inverse cascade mechanisms to explain the size distribution of roll-like coherent structures. Large-swath SAR acquisitions further often provide a comprehensive view of TCs, including the mesoscale spiralling circulation, along with eye characteristics, downdrafts and gust fronts of cold pools in the rain bands. In particular, Yurchak (2024), analyzing SAR images, attempted to estimate an overall effective friction by evaluating the angle between the cloud streamline and the quasi-circular isobar, possibly linking the spiral of rain properties to the storm intensity. Regarding instantaneous coincident sea state information, which also depends on local wind speed and direction as well as their space-time evolutions, the pioneering work of Schulz-Stellenfleth et al. (2007) has now been thoroughly tested. Translated to Sentinel 1 WaVe mode SLC data, the initial decomposition has been slightly augmented, leading Stopa and Mouche (2017) and Quach et al. (2021) to robustly invert image spectrum information to wave parameters. S1 wide swath images are also now more commonly analyzed, in non-extreme situations (Pleskachevsky et al., 2022). These emerging capabilities applied to TC situations shall now benefit from increased available in situ wave measurements by saildrones, drifting buoys and airplanes, to continuously improve the reference data sets to refine the transfer function between SAR and sea-state parameters. An illustration of the significant wave height retrieved from the image-cross-spectra computation on Sentinel-1 level-1 SLC data is presented in section 4.2.2 (see Fig. 18). Clearly, to fully leverage the very rich content of any individual TC SAR measurements, new methods are certainly required to accurately detect, segment, and analyze all complex features detected. Compared and possibly informed with other available information, including other satellite and in situ observations, enriched with numerical simulations, the complex features and associated local textures will certainly provide valuable insights into the intricate dynamics of TCs.

5.2. *Future SAR missions*

The planning of future SAR missions is already extensive and will contribute significantly to TC monitoring. Beyond quantity (potentially important for sampling), the new missions will also introduce capabilities that could address some of the limitations regarding data quality highlighted in this paper. This section presents the most promising SAR upcoming missions.

5.2.1. *ALOS-2 and ALOS-4*

ALOS-2 (Advanced Land Observing Satellite-2) is a Japanese satellite equipped with the Phased Array-type L-band Synthetic Aperture Radar-2 (PALSAR-2) launched on May 24, 2014. The primary mission of ALOS-2 is to monitor terrestrial areas for landslides, floods, earthquakes, volcanoes, forests, and agriculture. Recent advancements in SAR have demonstrated its capability of measuring ocean surface backscatter under TC conditions to retrieve ocean surface wind speeds with high spatial resolution and accuracy (e.g., Zhang and Uhlhorn (2012); Mouche et al. (2019). In response to recent TC-related wind disasters in Japan, JAXA and MRI launched a joint project in the summer of 2019 to develop TC ocean wind products using ALOS-2/PALSAR-2 (Isoguchi et al., 2021; Shimada et al., 2024b). PALSAR-2 has a wide scan mode, ScanSAR, with an observation swath width of 350 km, which allows for the observation of an entire TC area.

Compared to other C-band SAR satellites such as Sentinel-1, Radarsat, and the RADARSAT Constellation Mission (RCM), ALOS-2 has two advantages. One is its orbit. ALOS-2 is in a sun-synchronous sub-recurrent orbit with a local time of 12:00 in the descending pass. In contrast, C-band SAR satellites have a local sun time of 06:00 in the descending pass. Thus, the time interval between ALOS-2 and C-band SAR observations is approximately 6 hours. This interval matches the timing of TC advisories issued by operational centers. It is expected that the development of L-band SAR wind products can help increase the frequency of SAR observations up to 6-hours interval. Another advantage is that L-band SAR is expected to have less rain attenuation in the atmosphere and less ice scattering effect from the atmospheric melting layer than C-band SAR (e.g., Alpers et al. (2021)). The L-band SAR wind retrieval algorithm development followed

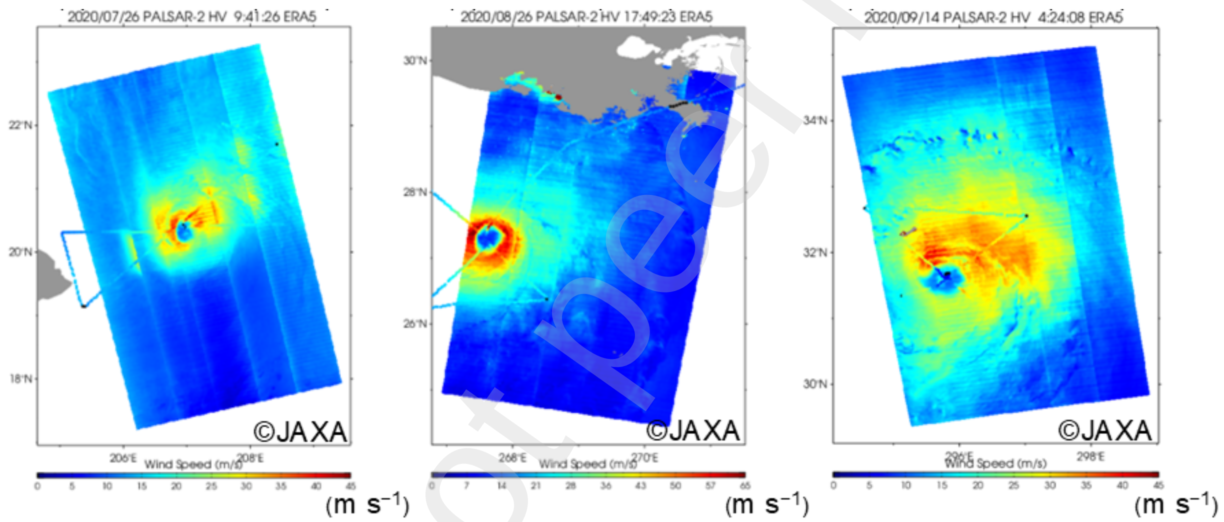

Fig. 25. ALOS-2 winds for (left) Hurricane Douglas (2020), (middle) Hurricane Laura (2020), and (right) Hurricane Paulette (2020) with SFMR winds overlaid.

a two-step procedure. First, 1,800 match-ups have been collected between PALSAR-2 cross-polarization backscattering coefficient (HV) and SFMR surface winds observed by aircraft in the North Atlantic. Then, the GMF, regressions between PALSAR-2 cross-polarization backscattering coefficient and wind speeds, have been derived from this matchup dataset by satellite incidence angles. Finally, ocean surface wind speed estimates can be retrieved using the developed GMFs. The horizontal resolution of the current ALOS wind products is 3 km. Further details are described by Isoguchi et al. (2021) and by Shimada et al. (2024b).

Fig. 25 show retrieved wind speeds for three hurricanes. It is confirmed that PALSAR-2 is capable of high wind speed retrieval up to 55 m.s^{-1} without any saturation at high wind speeds.

However, the retrieved winds have some quality issues. To this end, radiometric correction using more matchup data is required. Specifically, corrections for Radio Frequency Interference (RFI), NESZ, and Faraday rotation in the ionosphere are needed. For example, without a Faraday rotation correction, the retrieved wind speeds tend to be much higher than other observations. A correction method is being developed to obtain less biased wind speeds (see slide 9 in Shimada (2024a)).

JAXA successfully launched ALOS-4 on July 1, 2024. ALOS-4 is the successor of ALOS-2 and is equipped with PALSAR-3. The swath width of the ScanSAR mode is doubled to 700 km and can operate in dual-polarization mode. ALOS-4 is scheduled to begin observing TCs in 2025 and is expected to participate to increase the overall SAR spatio-temporal sampling of TCs..

5.2.2. *NISAR*

NISAR is a joint Earth-observing mission between U.S. NASA and the Indian Space Research Organization (ISRO). The NISAR system comprises a dual frequency, fully polarimetric radar. The NISAR mission is focused on Earth's changing ecosystems, dynamic surfaces, and ice masses providing information about biomass, natural hazards, sea level rise, and groundwater. NISAR is planned to launch in 1Q 2025 from India's Satish Dhawan Space Center.

Beside operating at dual frequency (L- and S-band), NISAR will be unique in that the system will be south (left) pointing and it will use a 12-meter diameter deployable mesh antenna. At L-Band this produces a 242-kilometer swath which will have 7-meter resolution along track (the direction of travel) and 2- to 8-m resolution cross-track (depending on the viewing mode). The incidence angle range will span 33 – 47 with a baseline NESZ of -25 dB (eoPortal, Aug 22, 2024) .

The polarimetric diversity and NESZ characteristics mean that NISAR observations will be suitable for determining TC winds. The system's regular collection pattern will include the Gulf of Mexico, the Caribbean Sea and the Bay of Bengal and additional TC observations are possible under the NISAR natural hazards / disaster response mission. An appropriate L-Band TC GMF will need to be developed for NISAR, but the procedure has already been established for ALOS-2. NISAR science data, L-band and S-band, will be freely available and open to the public under NASA's Earth Science open data policy.

5.2.3. *ROSE-L*

ROSE-L is a mission that will operate SAR at L-band and is planned to be contemporary with the C-band Sentinel-1 Next-Generation (S1 NG) mission. This coordinated approach will allow for synergistic observations and the exploitation of both L-band and C-band data from the European constellation. If the sensors provide near-simultaneous observations, we can leverage their complementary nature to strengthen the constraints applied to the inversion scheme for retrieving geophysical parameters. In contrast, If the acquisitions allow for sequential observations, we can achieve more frequent observations, which will be beneficial for characterizing the dynamics of the storms and possibly issue more accurate warning bulletins, for instance in cases of rapid intensification. As for S1 NG a WaVe mode is planned for the open ocean. This would significantly increase the sampling of the swell escaping from the storm to further study the mechanism of waves dissipation or waves interactions with inertial currents induced by the TC.

Although L-band SAR instruments are less sensitive to wind speed and direction fluctuations at medium incidence angles compared to higher frequencies, there have been encouraging studies to estimate ocean surface wind field based on ALOS PALSAR-2 measurements (see Isoguchi et al. (2021) and section 5.2.1). They suggest that L-band SAR could potentially achieve performance comparable to C-band SAR, provided that the radiometric performance, including accuracy, stability, and Noise-Equivalent Sigma Zero is adequate. Typically, the NRCS measured at L-band with PALSAR-2 ranges from -35 to -20 dB in cross-polarization for incidence angles ranging from 10 to 70 degrees. In contrast to rain effects observed at C-band that can lead to both significant increase or decrease of the backscattered signal, L-band measurements suffer mostly from signal decrease. Although generally attributed to rain-generated turbulence in the upper water layer, which reduces the sea surface roughness (see Melsheimer et al. (1998)) this is not demonstrated in the particular case of TCs. As for C-band the detection and possibly correction of the rain effect will be part of the challenges to face for providing accurate wind speed estimates.

A key difference between C- and L-band radar is the impact of Faraday rotation. When an L-band radar wave passes through the ionosphere, its polarization plane is rotated. This is an additional contribution to the depolarization effect of the signal from the ocean surface. During periods of high solar activity, the increased electron density in the ionosphere can exacerbate this effect, leading to significant contributions in cross-polarization (Freeman and Saatchi, 2004). For instance, over the ocean, PALSAR-2 measurements revealed that a Faraday rotation of about 20° can lead to cross-polarized backscatter intensity comparable to HH polarization. To accurately interpret ocean surface parameters from L-band radar data, it is thus crucial to mitigate this effect. This often involves techniques that require independent measurements of Total Electron Content (TEC) and polarimetric data and will be a challenge to maximize the benefit of the ROSE-L constellation.

5.2.4. Harmony

The ESA Earth Explorer 10 Harmony mission is conceived to serve a range of science objectives related to the cryosphere, solid-Earth, and upper oceans and air-sea interactions. The Harmony's mission concept consists of flying two C-band receive-only radar satellites in a configurable formation with Sentinel-1 D, which will be used as illuminator. Formation flying allows an in-orbit reconfiguration of the observation geometry. This in-orbit configurability is key to enable the multi-purpose nature of the mission. In addition to the radar, the two Harmony satellites will carry a thermal infrared (TIR) payload providing several simultaneous observations of the radar-swath at different viewing angles.

In the StereoSAR formation the two Harmony spacecraft will fly 350-400 kilometer ahead or behind Sentinel-1. This will result in three simultaneous observation geometries. Harmony will thus provide multi-directional observations of the sea-surface roughness to allow more precise retrieval of surface wind vectors at O(km) resolution, and directional surface wave information O(10 km). It will coincidentally provide multi-directional Doppler velocity measurements, to inform about the detected surface velocities at resolutions of a few kilometer or even, for high energetic features, at sub-kilometer resolutions. In practice, considering the linear vertically or horizontally polarized signal transmitted by Sentinel-1, the bistatic configuration is analogous to a monostatic configuration transmitting a slanted linear polarization, with the slant-angle depending on the angle of incidence. As the receive antenna will be dual-polarized, the whole system behaves as an hybrid-polarized sensor, which can be exploited to quantify contributions from different scattering mechanisms, largely augmenting the present-day capabilities using co-and cross bistatic combinations. Furthermore, it should be emphasized that the Doppler associated to the mean surface motion is polarization independent, while the Doppler, induced by the surface motions, is polarization dependent. Multi-directional spectral estimates will also be available to further constrain the surface wave directional properties, and associated multi-look derived parameters.

Finally, in cloud-free areas, the TIR sensor will provide simultaneous observations of the SST, providing a uniquely rich view of the underlying upper ocean processes. The multi-beam stereo TIR views will further allow the retrieval of cloud-top motion vectors and cloud-top height, which combined with the high resolution wind and waves data will provide unique instantaneous views of the marine atmospheric boundary layer.

6. Conclusions

From an Earth-Observation perspective, an important component of Digital Twin Ocean (DTO) developments builds on data-centric approaches, becoming essential layers to train, test and validate improved digital replicas of the real ocean-atmosphere system. At relatively modest resolutions, Machine Learning (ML) models trained on data assimilating global models, e.g. ERA-5, are currently emerging as very impressive and robust emulators of numerical weather models (Bi et al., 2023; Kochkov et al., 2024). But targeting extreme ocean-atmosphere events, especially to improve the realism of TC intensification, ensemble of weather numerical forecasts must at least be resolved at km-scale (Baker et al., 2024). Moreover, coherent structures within the TC boundary layer, like quasi-two dimensional roll vortices corresponding to localized intense variations of vertical velocities, can only be resolved using very highly resolved numerical simulation, O(100 m), typical resolution of Large Eddy Simulation (LES) models (Liu et al., 2021; Momen et al., 2021). Successfully emulating km to 100m-scale, inherently less predictable, ocean-atmosphere dynamics will then require high-quality training data sets. Sufficiently large numbers of cases are necessary in order to train and validate these AI/DL (Articifical Intelligence/Deep Learning) models. In that context, the first 10 years of the Sentinel-1 mission have been demonstrated to provide unique sources of quantitative synoptic ocean surface high-resolution information, available in the different ocean basins.

As presented in this paper, Sentinel-1's first ten years indeed fostered many activities to exploit SAR observations acquired over TCs. This is a clear heritage of the long-term effort of CSA and NOAA since Radarsat-1 (Banal et al., 2007), and findings based on Radarsat-2 dual-polarization data (Vachon and Wolfe, 2011; Zhang and Perrie, 2012a). However, ESA's efforts establishment of a dedicated TC monitoring campaign using Sentinel-1 was a turning point, providing free data to the community and defining the first generation of wind speed algorithms that take advantage of the two polarization channels available and can estimate extreme wind associated with major TCs (Mouche et al., 2019). The initial SHOC experiment concept is ongoing at ESA and has continued to improve over time ensuring more systematic TC monitoring with Sentinel-1. Thus, for the first time (e.g., 2016-2020) free SAR Level-1 data, was available to test, revise and compare retrieval algorithms. Available Level-1 data processed in both GRD and SLC has not only spurred new developments, but also enhanced comparisons with in situ observations. This has led to significant improvements in the quality of both Level-1 and Level-2 data (e.g., NESZ, GMFs).

Focusing on surface wind estimates, S1 data have been more systematically compared to airborne SFMR measurements, the multi-frequency radiometer used for TC monitoring in U.S. waters. These comparisons fully demonstrate the unique ability of SAR winds to describe the TC structure at very high resolution, including the lowest extent wind radii of 50 and 64 knots and $R_{\max}$ (Combot et al., 2020a). Efforts to precisely infer TC surface wind structures, notably TC inner-core characteristics, i.e. TC eye location and $R_{\max}$, has been robustly demonstrated. Estimating inner wind radii remains a challenge for TC forecasters due to the sparsity of surface wind analyses that can precisely depict their spatial extensions. Consistent SAR-based estimates of all the wind radii, the intensity, and the $R_{\max}$ helped revise statistical relationships (e. g. Chavas and Knaff (2022)), to more systematically predict $R_{\max}$ from outer wind radii and $V_{\max}$ (Avenas et al., 2023). Such a relationship will soon be part of the TC operational forecaster dialogue at JTWC to provide forecasters with a quality estimate of $R_{\max}$ when preparing their advisories and is already used in some JTWC forecast applications. Results from the SHOC datasets, presented to the TC forecaster community at the WMO TC meeting in 2018, led some TC operational centers to start considering SAR data during their operations to issue forecasts or refine their tracks afterward. In 2019, NOAA started operating a service to process and deliver SAR wind products (maps and fix profiles, which are now regularly used by TC centers. For instance, JTWC's operational forecast system ATCF has been fed with SAR wind data since 2019 to assist forecasters in issuing their reports (Howell et al., 2022), and operational SAR data exploitation has been carried out in RSMC la Réunion forecasting centre since 2021 via the dedicated NOAA website (STAR-SOCD). For an optimal use in RSMC la Réunion forecasting centre, ideally SAR passes would occur six-hourly between six and three hours prior to their advisory times (i.e., 00, 06, 12, 18 UTC) and be available on operational workstations within two hours.

TC SAR analysis can also often be used as a reference to derive the same structural characteristics from other types of sensors, such as IR channels from GEO satellites or PMW sounders/imagers. Combining SAR snapshots with GEO observations (Tsukada and Horinouchi, 2023; Tsukada et al., 2024) provides the possibility of more precise documentation of the evolution of TC inner core properties throughout its lifecycle, possibly including evolving vertical wind shear conditions. Moreover, SAR-derived wind speed estimates can be adjusted to any other instrument resolution, e.g. C-band scatterometers or C- and L-band microwave sensors (Zhao et al., 2018). It not only enables comparisons to refine multi-mission surface wind estimates, but also makes it possible to learn and train statistical methods to produce stochastic space-time super-resolved fields (Ni et al., 2025). Note, actual metrics to evaluate model performances are currently mainly based on the wind structure parameters as given by the best tracks (Baker et al., 2024). In this regard, TC SAR analyses provide superior estimates of TC wind structure metrics, and when available, influence best track parameters (Combot et al., 2020a).

Apart from conducting their analysis for their operational service, forecasters also provide invaluable feedback to data providers, pointing out case studies that help better understand the sensor physics (see examples in section 4.1.3). Importantly, besides Sentinel-1, other SAR missions are and will contribute to increasing acquisitions over extreme events. When SAR 's operated at other radar frequencies (e.g. ROSE-L, ALOS-4) or with augmented capacities (e.g. Harmony), these missions will provide new perspectives on the interactions between electromagnetic waves and rough ocean surfaces under extreme conditions. This will enable more precise understanding of backscattered signals, including their Doppler sensitivities and local modulations, to develop more advanced algorithms and quality flags. It can also offer means to revisit previous archived SAR measurements. The continuation of the Sentinel-1 mission with the recent launch of Sentinel-1C and the upcoming launch of Sentinel-1D, together with the Copernicus data policy, ensures on-going activities to continuously boost research efforts and new developments. This continuation will further upgrade the existing SAR database with more reliable geophysical in situ and/or re-analyzed parameters. The addition of rain flagging and wind directions are certainly the most natural ones to include, but other more challenging parameters such as rain rate or wave parameters may rapidly be added thanks to ongoing efforts.

As already mentioned, numerical simulations must be able to resolve at km to 100m-scales to improve the realism of a TC, especially during its intensification. Despite remarkable advancements (Matak and Momen, 2023; Ito et al., 2017), accurate hurricane forecasts remain challenging, likely due to inaccurate physical parameterizations to describe the complex dynamics. In this regard, the actual SAR C-band instrument constellation is the only satellite technology capable of instantaneously resolving fine-scale, wide-swath TC boundary layer (TCPBL) process data (Foster, 2017). Besides provision of high-quality training data sets, this directly shall help process understandings into advance efforts (theoretical, numerical, statistical) for improved both short-term predictions and long-term projections. Timely, recently a paradigm shift has occurred regarding the number of SAR observations jointly co-located with aircraft measurements to describe high resolution inner core TC properties. In particular, TC reconnaissance flight programs are successfully on-going and continuously upgraded with new instrument designs. Discussed in Section 4.2.4, under TC conditions, the pressure gradient force is a dominant term in the TCBL momentum budget. Using a single-columnar model, the SAR high resolution imprint of the surface wind field can then be used to estimate the surface pressure gradient field. The related wind field at the top of the boundary-layer along with the surface winds can then be used to infer vertical variations of an effective turbulent eddy viscosity associated with SAR-detected roll orientation. As more cases are examined this information should contribute to the development and/or improvement of the TCBL parameterizations used in numerical models. By relying on combined SAR observations, more targeted use-cases can and will be identified for which in situ measurements precisely document the atmosphere and ocean coupled boundary layers (e.g. IWRAP, SFMR, saildrone, ...), capturing the characteristics (horizontal and vertical, size, distribution) of coherent turbulent structures, in both ocean and atmosphere, including surface wave estimates.

Increasing and augmenting SAR observations is also key to better covering the TC life-time evolutions, opening perspectives to more precisely sample TC dynamical transitions and reveal ocean-atmosphere couplings. In particular, a number of cases corresponding to rapid intensifications possibly related to ocean feedbacks, e.g. associated with ocean interior peculiar stratification (Balaguru et al., 2020; Looney and Foltz, 2025), are and will be continuously accumulated. Discussed Section 4.2.5, the TC inner-core wind structure, especially the surface wind inflow and anisotropic decay profile of the wind intensity, will be more systematically retrieved, and tested to govern the short-time TC dynamics (Avenas et al., 2024a). Given these new opportunities to follow TC inner-core surface wind characteristics, data-driven statistical and/or physic-informed frameworks (Du et al., 2024), possibly combining multi-modal and multi-resolution observations, can thus be more robustly elaborated.

Notably, the joint analysis of TC wind structure parameters from SAR and sea surface height anomaly from altimeters shows how a TC passage impacts the mixed sea layer (Combot, 2023). This work could now be augmented by the new observing capabilities of the SAR constellation and the SWOT mission (see section 4.2.3) should be able to uniquely provide the 2D signature of the TC wake at the sea surface and its evolution throughout the TC lifecycle. Such a diagnostic is dominated by the baroclinic ocean response to a TC passage, and can thus be used to infer ocean stratification or to test the consistency of forced TC parameters with measured sea surface height anomalies.

We also illustrated the potential synergy between different observing systems to further characterize the TC-generated waves and study the generation processes (see section 4.2.2). In particular, combined observations should lead to more precise quantification of directional spreading and dissipation properties of TC swell systems. The non-linear imaging mechanism of waves with SAR is particularly complex in areas of strong sea states, but new approaches to decompose the signal can certainly help provide practical solutions. In the near future, the new generation of SAR missions, such as Harmony with various viewing angles, should contribute to disentangling the various contributions to the imaging mechanism, allowing for more physical constraints for wave retrieval.

To conclude, the first 10 years of the Sentinel-1 mission paved the way to a wide range of new scientific opportunities. They span from use-case studies combining SAR observations with other medium-resolution satellite measurements, high-resolution in situ data, high resolution space-time GEO observations, analytical models, and simulations, to the translation of growing SAR databases into ML-based approaches. This past decade has also helped refine the strategy for optimizing the number of acquisitions over TCs based on forecast tracks. It has allowed for more precise specification of requirements such as swath width, highest resolution needs, polarization diversities, noise floor and Doppler calibration. In the near future, SAR databases and joint data-driven analyses, as outlined in this paper, are expected to facilitate the development of dedicated sensor-based foundation models. Moreover, they hold the potential to significantly improve model evaluations while identifying critical processes for encoding data-driven dynamics into future digital twin innovations.

Credit authorship contribution statement

Alexis Mouche: Conceptualization. Writing - original draft for section 3.3.1 and section 3.3.2. Methodology and Formal analysis for section 1, section 3.3.1 and section 3.3.2, section 5.1, section 5.2 and section 6. Review & Editing the manuscript; Arthur Avenas: Conceptualization original draft, Methodology, Data processing, Visualization Formal analysis and Writing - Original draft for section 4.2.5, section 4.2.1 and section 5.2; Writing - Review & Editing the manuscript; Paul Chang: SFMR and IWRAP Data processing and analysis; Writing - Review & Editing for section 4.2.4; Bertrand Chapron: Conceptualization section 4.2.2. Writing - original draft for section 1, section 4.2.3, section 4.2.2, section 4.2.5 and section 6. Review & Editing the manuscript; Théo Cévaër: Data Processing and Visualization for Section 3; Clément Combot: Conceptualization, Methodology, Data processing, Formal Analysis, Visualization, Writing - Original draft and Writing - Review & Editing for section 4.2.3 and section 3, section 3.3.2 and section 3.3.2; Joe Courtney: Conceptualization, Formal analysis, Visualization, Writing - original draft, Writing - Review & Editing for section 4.1.2; Quentin Febvre: Data Analysis for section 5.1; Ralph Foster: Conceptualization, Data Processing, Formal analysis, Methodology, Visualization, Writing - original draft, Writing - Review & Editing for section 4.2.4; Antoine Grouazel: Data Analysis for section 5.1; Masahiro Hayashi: Writing - Review & Editing section 4.1.4; Takeshi Horinouchi: Writing - original draft, Writing - Review & Editing for section 4.2.1; Yasutaka Ikuta: Writing

- Review & Editing for section 4.1.4; Osamu Isoguchi: Writing - Review & Editing for section 5.2.1; Christopher Jackson: Data Processing and Analysis, Visualization, Writing - Review & Editing for section 3; Zorana Jelenak: SFMR and IWRAP Data processing and analysis; Writing - Review & Editing for section 4.2.4; John A. Knaff : Conceptualization for section 4.1. Writing - Review & Editing the manuscript; Sébastien Langlade: Conceptualization, Visualization, Writing - original draft and Writing - Review & Editing for section 4.1.3; Jean-Renaud Miadana: Data Processing and Analysis for section 5.1; Frédéric Nouguier: Data Processing and Analysis, Writing - Review & Editing for section 5.1; Masato Ohki: Writing - original draft and Writing - Review & Editing for section 5.2.1; Clément Pouplin: Writing - original draft, Data Processing and Analysis, Visualization, Writing - Review & Editing for section 4.2.2; Tyler Ruff: Data Processing and Analysis, Visualization, Writing - Review & Editing for section 3; Charles R. Sampson: Conceptualization and Writing - original draft section 4.1. Visualization section 4.1.1, Writing - Review & Editing the manuscript; Joseph Sapp : SFMR and IWRAP Data Processing and Analysis; Writing - Review & Editing for section 4.2.4; Udai Shimada: Conceptualization, Visualization, Writing - original draft, Writing - Review & Editing for section 5.2.1, section 4.1.4 and section 4.2.1; Takeo Tadono: Conceptualization, Writing - original draft, Review & Editing for section 5.2.1; Taiga Tsukada: Conceptualization, Writing - original draft, Writing - Review & Editing for section 4.2.1; Visualization section 4.2.1, section 4.1.2 and section 4.1.3; Methodology and Formal Analysis for 4.2.1; Léo Vinour: Writing - original draft, Writing - Review & Editing for section 3.3.2 and section 4.2.1. Visualization section 4.2.1. Methodology and Formal Analysis for section 3.3.2.

Declaration of Competing Interest

The authors declare no known competing financial interests or personal relationships that could have appeared to influence the work reported in this paper.

Data availability

CyclObs SAR wind products are available at https://cyclobs.ifremer.fr/app/. NOAA STAR SAR wind products are available on our website https://www.star.nesdis.noaa.gov/socd/mecb/sar/sarwinds_tropi Sentinel-1 is part of the European space component of Copernicus European program. Level-1 data are free of charge and available on the Copernicus Open Access Hub (https://scihub.copernicus.eu/).

RADARSAT-2 is a commercial mission, and Level-1 data are provided by MDAs Geospatial Services (https://mdacorporation.com/geospatial/international). Level-1 Radarsat Constellation Mission data are obtained through a partnership with CSA. The NEXRAD products are archived by the National Climatic Data Center and available through FTP (http://www.ncdc.noaa.gov/nexradinv/choosesite.jsp). Ocean vertical Argo profiles are collected by GDACS and are distributed by Ifremer: https://data-argo.ifremer.fr/geo. L3 nadir-looking SSH measurements for each altimeter were provided by CMEMS service (https://doi.org/10.48670/moi-00147). The SWOT_L3_LR_SSH product, derived from the L2 SWOT KaRIn low rate ocean data products (NASA/JPL and CNES), is produced and made freely available by AVISO and DUACS teams as part of the DESMOS Science Team project". AVISO/DUACS, 2024. SWOT Level-3 KaRIn Low Rate SSH Basic (v2.0). CNES. https://doi.org/10.24400/527896/A01-2023.017. The SWIM L2S data are provided by the Ifremer Wind and Wave Operation Center on https://cersat.ifremer.fr/fr/Projects/Recent-and-ongoing-projects/IWWOC. Spotter buoys data we used were provided by SOFAR Ocean through an academic agreement. However an archive is available at: https://www.sofarocean.com/mx/sofar-spotter-archive. Meteosat-9 data are available at: https://data.eumetsat.int/data/map/EO:EUM:DAT:MSG:HRSE IODC. Himawari-8 data are available at: https://registry.opendata.aws/noaa-himawari/. GOES-16 data are available at: https://registry.opendata.aws/noaa-goes/. SSMI/S PMW data available at: https://arthurhou.pps.eosdis.nasa.gov/. The IWRAP data used in this manuscript is available at (Sapp, 2025). The SFMR data used in this manuscript is available at https://manati.star.nesdis.noaa.gov/SFMR

Acknowledgements

CyclObs team acknowledges the support of Nuno Miranda, Muriel Pinheiro, Marie Hélène Rio, and the Sentinel-1 mission planning team at ESA, Romain Husson at CLS. A.M. contribution is partly funded by the European Space Agency (under grant 4000135998/21/i-BG for ESA Sentinel-1 Performance Center, 4000132954/20/I-NB for ESA Marine Atmosphere eXtreme Satellite Synergy (MAXSS) and 4000137982/22/I-DT for ESA SARWAVE) and by ANR (under grant ANR-10-IEED-0006-34, FEM, OROWSHI). B.C. contribution is partly funded by the European Space Agency (under grant 4000135827/21/NL–FF for Harmony Science Data Utilisation and Impact Study for Ocean, 4000132954/20/I-NB for ESA Marine Atmosphere eXtreme Satellite Synergy (MAXSS)). C.C. and L.V. are funded by the Japan Science and Technology Agency (MOONSHOT). Q.F., A.G. and F.N. are partly funded by the European Space Agency (under grant 4000137982/22/I-DT for ESA SARWAVE). R.C.F. acknowledes ONR TCRI DRI, (grant N000142012148). U.S. is partially funded through MEXT KAKENHI (Grant 23K20883 and 23K13172). Z.J. is funded under Weather and Air Quality Research Program within the NOAA/OAR/Weather Program Office under Award NO.NA23OAR4590412-01. NESDIS provides salary support for J. Knaff's efforts. C.P. is funded by ANR (under grant ANR-10-IEED-0006-34, FEM, OROWSHI). C.J., T.R. and J.S. are partly funded under Global Science and Technology Corporation (funding line ST13301CQ0050/1332KP22FNEED0042). C.R.S. is funded by ONR (Code 32). T.T. was supported by the NOAA (under grant NA19OAR4320073-T1-01), and the Office of Naval Research (under grant N00014-21-1-2112). The scientific results and conclusions, as well as any views or opinions expressed herein, are those of the authors and do not necessarily reflect those of NOAA or the Department of Commerce.

References

Alpers, W., Zhang, B., Mouche, A., Zeng, K., Chan, P.W., 2016. Rain footprints on C-band synthetic aperture radar images of the ocean - Revisited. Remote Sensing of Environment 187, 169–185. URL: https://linkinghub.elsevier.com/retrieve/pii/S003442571630387X, doi:10.1016/j.rse.2016.10.015.

Alpers, W., Zhao, Y., Mouche, A.A., Chan, P.W., 2021. A note on radar signatures of hydrometeors in the melting layer as inferred from sentinel-1 sar data acquired over the ocean. Remote Sensing of Environment 253, 112177. URL: https://www.sciencedirect.com/science/article/pii/S0034425720305502, doi:https://doi.org/10.1016/j.rse.2020.112177.

Ardhuin, F., Chapron, B., Collard, F., 2009. Observation of swell dissipation across oceans. Geophysical Research Letters 36.

Avenas, A., Chapron, B., Mouche, A., Platzer, P., L., V., 2024a. Revealing short-term dynamics of tropical cyclone wind speeds from satellite synthetic aperture radar. Sci Rep 14. doi:https://doi.org/10.1038/s41598-024-61384-w.

Avenas, A., Mouche, A., Knaff, J., Carton, X., Chapron, B., 2024b. On the tropical cyclone integrated kinetic energy balance. Geophysical Research Letters 51, e2024GL108327. URL: https://agupubs.onlinelibrary.wiley.com/doi/abs/10.1029/2024GL108327, doi:https://doi.org/10.1029/2024GL108327, arXiv:https://agupubs.onlinelibrary.wiley.com/doi/pdf/10.1029/2024GL108327. e2024GL108327 2024GL108327.

Avenas, A., Mouche, A., Tandeo, P., Piolle, J.F., Chavas, D., Fablet, R., Knaff, J., Chapron, B., 2023. Reexamining the estimation of tropical cyclone radius of maximum wind from outer size with an extensive synthetic aperture radar dataset. Monthly Weather Review 151, 3169–3189.

Babin, S.M., Carton, J.A., Dickey, T.D., Wiggert, J.D., 2004. Satellite evidence of hurricane-induced phytoplankton blooms in an oceanic desert. Journal of Geophysical Research: Oceans 109. URL: https://agupubs.onlinelibrary.wiley.com/doi/abs/10.1029/2003JC001938, doi:https://doi.org/10.1029/2003JC001938, arXiv:https://agupubs.onlinelibrary.wiley.com/doi/pdf/10.1029/2003JC001938.

Baker, A.J., Vannière, B., Vidale, P.L., 2024. On the realism of tropical cyclone intensification in global storm-resolving climate models. Geophysical Research Letters 51, e2024GL109841. URL: https://agupubs.onlinelibrary.wiley.com/doi/abs/10.1029/2024GL109841, doi:https://doi.org/10.1029/2024GL109841, arXiv:https://agupubs.onlinelibrary.wiley.com/doi/pdf/10.1029/2024GL109841. e2024GL109841 2024GL109841.

Balaguru, K., Foltz, G.R., Leung, L.R., Kaplan, J., Xu, W., Reul, N., Chapron, B., 2020. Pronounced impact of salinity on rapidly intensifying tropical cyclones. Bulletin of the American Meteorological Society 101, E1497–E1511.

Banal, S., Iris, S., Saint-Jean, R., 2007. Canadian Space Agency’s Hurricane Watch Program: Archive contents, Data Access and improved planning strategies, in: 2007 IEEE International Geoscience and Remote Sensing Symposium, IEEE. pp. 3494–3497. URL: http://ieeexplore.ieee.org/document/4423599/, doi:10.1109/IGARSS.2007.4423599.

Bender, M.A., Ginis, I., Kurihara, Y., 1993. Numerical simulations of tropical cyclone-ocean interaction with a high-resolution coupled model. Journal of Geophysical Research: Atmospheres 98, 23245–23263. URL: https://agupubs.onlinelibrary.wiley.com/doi/abs/10.1029/93JD02370, doi:https://doi.org/10.1029/93JD02370, arXiv:https://agupubs.onlinelibrary.wiley.com/doi/pdf/10.1029/93JD02370.

Bessho, K., Date, K., Hayashi, M., Ikeda, A., Imai, T., Inoue, H., Kumagai, Y., Miyakawa, T., Murata, H., Ohno, T., Okuyama, A., Oyama, R., Sasaki, Y., Shimazu, Y., Shimoji, K., Sumida, Y., Suzuki, M., Taniguchi, H., Tsuchiyama, H., Uesawa, D., Yokota, H., Yoshida, R., 2016. An introduction to himawari-8/9mdash; japanrsquo;s new-generation geostationary meteorological satellites. Journal of the Meteorological Society of Japan. Ser. II 94, 151–183. doi:10.2151/jmsj.2016-009.

Bi, K., Xie, L., Zhang, H., Chen, X., Gu, X., Tian, Q., 2023. Accurate medium-range global weather forecasting with 3d neural networks. Nature 619, 533–538. URL: https://www.nature.com/articles/s41586-023-06185-3, doi:10.1038/s41586-023-06185-3.

Black, P.G., D'Asaro, E.A., Drennan, W.M., French, J.R., Niiler, P.P., Sanford, T.B., Terrill, E.J., Walsh, E.J., Zhang, J.A., 2007. Air–sea exchange in hurricanes: Synthesis of observations from the coupled boundary layer air–sea transfer experiment. Bulletin of the American Meteorological Society 88, 357–374.

Bureau of Meteorology, 2019. Severe Tropical Cyclone Veronica. Technical Report. Bureau of Meteorology, Commonwealth of Australia. URL: http://www.bom.gov.au/cyclone/history/pdf/Veronica_Report.pdf, doi:10.4095/219617.

Chapron, B., Collard, F., Ardhuin, F., 2005. Direct measurements of ocean surface velocity from space: Interpretation and validation. Journal of Geophysical Research: Oceans 110. URL: https://agupubs.onlinelibrary.wiley.com/doi/abs/10.1029/2004JC002809, doi:https://doi.org/10.1029/2004JC002809, arXiv:https://agupubs.onlinelibrary.wiley.com/doi/pdf/10.1029/2004JC002809.

Chapron, B., Johnsen, H., Garello, R., 2001. Wave and wind retrieval from sar images of the ocean, in: Annales des telecommunications, pp. 682–699.

Chavas, D.R., Knaff, J.A., 2022. A simple model for predicting the tropical cyclone radius of maximum wind from outer size. Weather and Forecasting 37, 563–579.

Chen, X., Bryan, G.H., Zhang, J.A., Cione, J.J., Marks, F.D., 2021. A framework for simulating the tropical cyclone boundary layer using large-eddy simulation and its use in evaluating pbl parameterizations. Journal of the Atmospheric Sciences 78, 3559 – 3574. URL: https://journals.ametsoc.org/view/journals/atsc/78/11/JAS-D-20-0227.1.xml, doi:10.1175/JAS-D-20-0227.1.

Chiang, T.L., Wu, C.R., Oey, L.Y., 2011. Typhoon kai-tak: An ocean's perfect storm. Journal of Physical Oceanography 41, 221 – 233. URL: https://journals.ametsoc.org/view/journals/phoc/41/1/2010jpo4518.1.xml, doi:10.1175/2010JPO4518.1.

Chou, K.H., Wu, C.C., Lin, S.Z., 2013. Assessment of the ascat wind error characteristics by global dropwindsonde observations. Journal of Geophysical Research: Atmospheres 118, 9011–9021. URL: https://agupubs.onlinelibrary.wiley.com/doi/abs/10.1002/jgrd.50724, doi:https://doi.org/10.1002/jgrd.50724, arXiv:https://agupubs.onlinelibrary.wiley.com/doi/pdf/10.1002/jgrd.50724.

Cline, I.M., 1920. Relation of changes in storm tides on the coast of the gulf of mexico to the center and movement of hurricanes. Monthly Weather Review 48, 127 – 146. URL: https://journals.ametsoc.org/view/journals/mwre/48/3/1520-0493_1920_48_127_rocist_2_0_co_2.xml, doi:10.1175/1520-0493(1920)48<127:ROCIST>2.0.CO;2.

Colin, A., Husson, R., 2025. Rainfall regression from c-band synthetic aperture radar using multitask generative adversarial networks. Artificial Intelligence for the Earth Systems 4, e240007. URL: https://journals.ametsoc.org/view/journals/aies/4/1/AIES-D-24-0007.1.xml, doi:10.1175/AIES-D-24-0007.1.

Collard, F., Ardhuin, F., Chapron, B., 2009. Monitoring and analysis of ocean swell fields from space: New methods for routine observations. Journal of Geophysical Research: Oceans 114.

Combot, C., 2023. Mixing and sea surface anomalies in the inertial wake of tropical cyclones: processes and contribution of microwave satellite data. Ph.D. thesis. Brest.

Combot, C., Mouche, A., de Boyer Montegut, C., Chapron, B., 2024. Toward comprehensive understanding of air-sea interactions under tropical cyclones: On the importance of high resolution and multi-modal observations. Geophysical Research Letters 51, e2024GL110637. URL: https://agupubs.onlinelibrary.wiley.com/doi/abs/10.1029/2024GL110637, doi:https://doi.org/10.1029/2024GL110637, arXiv:https://agupubs.onlinelibrary.wiley.com/doi/pdf/10.1029/2024GL110637. e2024GL110637 2024GL110637.

Combot, C., Mouche, A., Knaff, J., Zhao, Y., Zhao, Y., Vinour, L., Quilfen, Y., Chapron, B., 2020a. Extensive high-resolution synthetic aperture radar (sar) data analysis of tropical cyclones: Comparisons with sfmr flights and best track. Monthly Weather Review 148, 4545–4563.

Combot, C., Quilfen, Y., Mouche, A., Gourrion, J., de Boyer Montégut, C., Chapron, B., Tournadre, J., 2020b. Space-based observations of surface signatures in the wakes of the 2018 eastern pacific tropical cyclones. Journal of Operational Oceanography 13.

D'Asaro, E., Black, P.G., Centurioni, L.R., Chang, Y.T., Chen, S.S., Foster, R.C., Graber, H.C., Harr, P., Hormann, V., Lien, R.C., Lin, I.I., Sanford, T.B., Tang, T.Y., Wu, C.C., 2014. Impact of typhoons on the ocean in the pacific. Bulletin of the American Meteorological Society 95, 1405 – 1418. URL: https://journals.ametsoc.org/view/journals/bams/95/9/bams-d-12-00104.1.xml, doi:10.1175/BAMS-D-12-00104.1.

Du, P., Parikh, M.H., Fan, X., Liu, X.Y., Wang, J.X., 2024. Conditional neural field latent diffusion model for generating spatiotemporal turbulence. Nature Communications 15.

Duong, Q.P., Langlade, S., Payan, C., Husson, R., Mouche, A., Malardel, S., 2021. C-band sar winds for tropical cyclone monitoring and forecast in the south-west indian ocean. Atmosphere 12. URL: https://www.mdpi.com/2073-4433/12/5/576, doi:10.3390/atmos12050576.

Duong, Q.P., Wimmers, A., Herndon, D., Tan, Z.M., Zhuo, J.Y., Knaff, J., Al Abdulsalam, I., Horinouchi, T., Miyata, R., Avenas, A., 2023. Objective satellite methods including ai algorithms reviewed for the tenth international workshop on tropical cyclones (iwtc-10). Tropical Cyclone Research and Review 12, 259–266.

Dvorak, V.F., 1972. A technique for the analysis and forecasting of tropical cyclone intensities from satellite pictures , NOAA Tech. Memo. NESS 36, 15 pp.

Emanuel, K.A., 1986. An air-sea interaction theory for tropical cyclones. part i: Steady-state maintenance. Journal of Atmospheric Sciences 43, 585–605.

Engen, G., Johnsen, H., 1995. Sar-ocean wave inversion using image cross spectra. IEEE Transactions on Geoscience and Remote Sensing 33, 1047–1056. doi:10.1109/36.406690.

eoPortal, Aug 22, 2024. Nisar (nasa-isro synthetic aperture radar). URL: https://directory.eoportal.org/satellite-missions/nisar. accessed: February 7, 2025.

ESA, 2005. Envisat sees whirling hurricane katrina from ocean waves to cloud tops. https://www.esa.int/About_Us/ESRIN/Envisat_sees_whirling_Hurricane_Katrina_from_ocean_waves_to_cloud_tops [Accessed on 2025/01/15].

Fan, S., Zhang, B., Mouche, A.A., Perrie, W., Zhang, J.A., Zhang, G., 2020. Estimation of wind direction in tropical cyclones using c-band dual-polarization synthetic aperture radar. IEEE Transactions on Geoscience and Remote Sensing 58, 1450–1462. doi:10.1109/TGRS.2019.2946885.

Fernandez, D., Kerr, E., Castells, A., Carswell, J., Frasier, S., Chang, P., Black, P., Marks, F., 2005. Iwrap: the imaging wind and rain airborne profiler for remote sensing of the ocean and the atmospheric boundary layer within tropical cyclones. IEEE Transactions on Geoscience and Remote Sensing 43, 1775–1787. URL: http://ieeexplore.ieee.org/document/1487635/, doi:10.1109/TGRS.2005.851640.

Foster, R., 2017. Sea-Level Pressure Retrieval from SAR Images of Tropical Cyclones. Springer Singapore, Singapore. p. 255–270. URL: http://link.springer.com/10.1007/978-981-10-2893-9_12, doi:10.1007/978-981-10-2893-9_12.

Foster, R.C., 2005. Why Rolls are Prevalent in the Hurricane Boundary Layer. Journal of the Atmospheric Sciences 62, 2647–2661. URL: https://doi.org/10.1175/JAS3475.1, doi:10.1175/JAS3475.1.

Foster, R.C., 2009. Boundary-layer similarity under an axisymmetric, gradient wind vortex. Bound.-Layer Meteor. 131, 321–344.

Foster, R.C., 2013. Signature of large aspect ratio roll vortices in synthetic aperture radar images of tropical cyclones. Oceanography 26. URL: http://dx.doi.org/10.5670/oceanog.2013.31, doi:http://dx.doi.org/10.5670/oceanog.2013.31.

Freeman, A., Saatchi, S., 2004. On the detection of faraday rotation in linearly polarized l-band sar backscatter signatures. IEEE Transactions on Geoscience and Remote Sensing 42, 1607–1616. doi:10.1109/TGRS.2004.830163.

Fu, L.L., Holt, B., 1982. Seasat views oceans and sea ice with synthetic-aperture radar. volume 81. California Institute of Technology, Jet Propulsion Laboratory.

Gao, Y., Zhang, J., Sun, J., Guan, C., 2021. Application of sar data for tropical cyclone intensity parameters retrieval and symmetric wind field model development. Remote Sensing 13. URL: https://www.mdpi.com/2072-4292/13/15/2902, doi:10.3390/rs13152902.

Geisler, J.E., 1970. Linear theory of the response of a two layer ocean to a moving hurricane‡. Geophysical Fluid Dynamics 1, 249–272. URL: http://www.tandfonline.com/doi/abs/10.1080/03091927009365774, doi:10.1080/03091927009365774.

Ginis, I., 2002. Tropical Cyclone-Ocean Interactions, in: Advances In Fluid Mechanics, pp. 83–114.

Ginis, I., Sutyrin, G., 1995. Hurricane-generated depth-averaged currents and sea surface elevation. Journal of Physical Oceanography 25, 1218 – 1242. URL: https://journals.ametsoc.org/view/journals/phoc/25/6/1520-0485_1995_025_1218_hgdaca_2_0_co_2.xml, doi:10.1175/1520-0485(1995)025<1218:HGDACA>2.0.CO;2.

Gonzalez, F., Thompson, T., Brown Jr, W., Weissman, D., 1982. Seasat wind and wave observations of northeast pacific hurricane iva, august 13, 1978. Journal of Geophysical Research: Oceans 87, 3431–3438.

Gonzalez, F.I., Beal, R.C., Brown, W.E., Deleonibus, P.S., Sherman, J. W., r., Gower, J.F., Lichy, D., Ross, D.B., Rufenach, C.L., Shuchman, R.A., 1979. Seasat synthetic aperture radar: ocean wave detection capabilities. Science (New York, N.Y.) 204, 1418–1421. URL: https://doi.org/10.1126/science.204.4400.1418.

Harper, B.A., Kepert, J., Ginger, J., 2010. Guidelines for converting between various wind averaging periods in tropical cyclone conditions. Technical Report 1555. World Meteorological Organization. URL: https://library.wmo.int/viewer/48652/download?file=wmo-td_1555_en.pdf&type=pdf&navigator=1.

Hauser, D., Tourain, C., Hermozo, L., Alraddawi, D., Aouf, L., Chapron, B., Dalphinet, A., Delaye, L., Dalila, M., Dormy, E., et al., 2020. New observations from the swim radar on-board cfosat: Instrument validation and ocean wave measurement assessment. IEEE Transactions on Geoscience and Remote Sensing 59, 5–26.

Hell, M.C., Ayet, A., Chapron, B., 2021. Swell generation under extra-tropical storms. Journal of Geophysical Research: Oceans 126, e2021JC017637.

Herndon, D.C., Velden, C., Wimmers, T., , Olander, T., Hawkins, J., 2012. Update on satellite-based consensus (satcon) approach to tc intensity estimation, in: 30th AMS Conference on Hurricanes and Tropical Meteorology.

Holland, G.J., 1980a. An Analytic Model of the Wind and Pressure Profiles in Hurricanes. Monthly Weather Review 108, 1212–1218. URL: https://doi.org/10.1175/1520-0493(1980)108<1212:AAMOTW>2.0.CO;2, doi:10.1175/1520-0493(1980)108<1212:AAMOTW>2.0.CO;2.

Holland, G.J., 1980b. An analytic model of the wind and pressure profiles in hurricanes. Monthly Weather Review 108, 1212–1218.

Holmlund, K., Grandell, J., Schmetz, J., Stuhlmann, R., Bojkov, B., Munro, R., Lekouara, M., Coppens, D., Viticchie, B., August, T., Theodore, B., Watts, P., Dobber, M., Fowler, G., Bojinski, S., Schmid, A., Salonen, K., Tjemkes, S., Aminou, D., Blythe, P., 2021. Meteosat third generation (mtg): Continuation and innovation of observations from geostationary orbit. Bulletin of the American Meteorological Society 102, E990 – E1015. URL: https://journals.ametsoc.org/view/journals/bams/102/5/BAMS-D-19-0304.1.xml, doi:10.1175/BAMS-D-19-0304.1.

Horstmann, J., Falchetti, S., Wackerman, C., Maresca, S., Caruso, M.J., Graber, H.C., 2015. Tropical Cyclone Winds Retrieved From C-Band Cross-Polarized Synthetic Aperture Radar. IEEE Transactions on Geoscience and Remote Sensing 53, 2887–2898. URL: http://ieeexplore.ieee.org/document/7001637/, doi:10.1109/TGRS.2014.2366433.

Horstmann, J., Wackerman, C., Falchetti, S., Maresca, S., 2013. Tropical Cyclone Winds Retrieved From Synthetic Aperture Radar. Oceanography 26. URL: https://tos.org/oceanography/article/tropical-cyclone-winds-retrieved-from-synthetic-aperture-radar, doi:10.5670/oceanog.2013.30.

Houghton, I., Smit, P., Clark, D., Dunning, C., Fisher, A., Nidzieko, N., Chamberlain, P., Janssen, T., 2021. Performance statistics of a real-time pacific ocean weather sensor network. Journal of Atmospheric and Oceanic Technology 38, 1047–1058.

Howell, B., Egan, S., Fine, C., 2022. Application of microwave space-based environmental monitoring (sbem) data for operational tropical cyclone intensity estimation at the joint typhoon warning center. Bulletin of the American Meteorological Society 103, E2315 – E2322. URL: https://journals.ametsoc.org/view/journals/bams/103/10/BAMS-D-21-0180.1.xml, doi:10.1175/BAMS-D-21-0180.1.

Ikuta, Y., Shimada, U., 2024. Impact of assimilation of the tropical cyclone strong winds observed by synthetic aperture radar on analyses and forecasts. Monthly Weather Review 152, 1007 – 1025. URL: https://journals.ametsoc.org/view/journals/mwre/152/4/MWR-D-23-0103.1.xml, doi:10.1175/MWR-D-23-0103.1.

Isoguchi, O., Tadono, T., Ohki, M., Shimada, U., Yamaguchi, M., Hayashi, M., Yanase, W., 2021. Hurricane ocean surface wind retrieval from alos-2 palsar-2 cross-polarized measurements, in: 2021 IEEE International Geoscience and Remote Sensing Symposium IGARSS, pp. 7291–7294. doi:10.1109/IGARSS47720.2021.9554411.

Ito, J., Oizumi, T., Niino, H., 2017. Near-surface coherent structures explored by large eddy simulation of entire tropical cyclones. Scientific Reports 7, 3798. URL: https://doi.org/10.1038/s41598-017-03848-w, doi:10.1038/s41598-017-03848-w.

Jackson, C., Ruff, T., Knaff, J., Mouche, A., Sampson, C., 2021. Chasing cyclones from space. Eos 102, –. URL: https://doi.org/10.1029/2021EO159148, doi:10.1029/2021EO159148.

Katsaros, K., Vachon, P.W., Black, P., Dodge, P., Uhlhorn, E., 2000a. Wind Fields from SAR: Could They Improve Our Understanding of Storm Dynamics? Technical Report 1. John Hopkins APL Technical Digest. doi:10.4095/219617.

Katsaros, K.B., Vachon, P.W., Black, P.G., Dodge, P.P., Uhlhorn, E.W., 2000b. Wind fields from sar: Could they improve our understanding of storm dynamics? Johns Hopkins APL Technical Digest 21, 86–93.

Kawabata, Y., Shimada, U., Yamaguchi, M., 2023. The 30-year (1987–2016) trend of strong typhoons and genesis locations found in the japan meteorological agencyapos;s dvorak reanalysis data. Journal of the Meteorological Society of Japan. Ser. II 101, 435–443. doi:10.2151/jmsj.2023-025.

Kepert, J., Wang, Y., 2001. The dynamics of boundary layer jets within the tropical cyclone core. part ii: Nonlinear enhancement. Journal of the Atmospheric Sciences 58, 2485 – 2501. URL: https://journals.ametsoc.org/view/journals/atsc/58/17/1520-0469_2001_058_2485_tdoblj_2.0.co_2.xml, doi:10.1175/1520-0469(2001)058<2485:TDOBLJ>2.0.CO;2.

Kim, D., Gu, M., Oh, T.H., Kim, E.K., Yang, H.J., 2021. Introduction of the advanced meteorological imager of geo-kompsat-2a: In-orbit tests and performance validation. Remote Sensing 13. URL: https://www.mdpi.com/2072-4292/13/7/1303, doi:10.3390/rs13071303.

Knaff, J.A., Brown, D.P., Courtney, J., Gallina, G.M., Beven, J.L., 2010. An evaluation of dvorak technique–based tropical cyclone intensity estimates. Weather and Forecasting 25, 1362 – 1379. URL: https://journals.ametsoc.org/view/journals/wefo/25/5/2010waf2222375_1.xml, doi:10.1175/2010WAF2222375.1.

Knaff, J.A., Longmore, S.P., Molenar, D.A., 2014. An Objective Satellite-Based Tropical Cyclone Size Climatology. Journal of Climate 27, 455–476. URL: http://journals.ametsoc.org/doi/abs/10.1175/JCLI-D-13-00096.1, doi:10.1175/JCLI-D-13-00096.1.

Knaff, J.A., Sampson, C.R., Kucas, M.E., Slocum, C.J., Brennan, M.J., Meissner, T., Ricciardulli, L., Mouche, A., Reul, N., Morris, M., Chirokova, G., Caroff, P., 2021. Estimating tropical cyclone surface winds: Current status, emerging technologies, historical evolution, and a look to the future. Tropical Cyclone Research and Review 10, 125–150. URL: https://www.sciencedirect.com/science/article/pii/S2225603221000266, doi:https://doi.org/10.1016/j.tcrr.2021.09.002.

Knapp, K.R., Kruk, M.C., Levinson, D.H., Diamond, H.J., Neumann, C.J., 2010. The international best track archive for climate stewardship (ibtracs) unifying tropical cyclone data. Bulletin of the American Meteorological Society 91, 363–376.

Koch, W., 2004. Directional analysis of SAR images aiming at wind direction. IEEE Transactions on Geoscience and Remote Sensing 42, 702–710. URL: http://ieeexplore.ieee.org/document/1288365/, doi:10.1109/TGRS.2003.818811.

Kochkov, D., Yuval, J., Langmore, I., Norgaard, P., Smith, J., Mooers, G., Klöwer, M., Lottes, J., Rasp, S., Düben, P., et al., 2024. Neural general circulation models for weather and climate. Nature 632, 1060–1066.

Kossin, J.P., Knaff, J.A., Berger, H.I., Herndon, D.C., Cram, T.A., Velden, C.S., Murnane, R.J., Hawkins, J.D., 2007. Estimating Hurricane Wind Structure in the Absence of Aircraft Reconnaissance. Weather and Forecasting 22, 89–101. URL: http://journals.ametsoc.org/doi/abs/10.1175/WAF985.1, doi:10.1175/WAF985.1.

Kudryavtsev, V., Golubkin, P., Chapron, B., 2015. A simplified wave enhancement criterion for moving extreme events. Journal of Geophysical Research: Oceans 120, 7538–7558. URL: https://onlinelibrary.wiley.com/doi/abs/10.1002/2015JC011284, doi:10.1002/2015JC011284.

Kudryavtsev, V., Monzikova, A., Combot, C., Chapron, B., Reul, N., Quilfen, Y., 2019. A Simplified Model for the Baroclinic and Barotropic Ocean Response to Moving Tropical Cyclones: 1. Satellite Observations. Journal of Geophysical Research: Oceans , 2018JC014746URL: https://onlinelibrary.wiley.com/doi/abs/10.1029/2018JC014746, doi:10.1029/2018JC014746.

Kudryavtsev, V., Yurovskaya, M., Chapron, B., 2021. Self-similarity of surface wave developments under tropical cyclones. Journal of Geophysical Research: Oceans 126. URL: https://onlinelibrary.wiley.com/doi/10.1029/2020JC016916, doi:10.1029/2020JC016916.

Li, H., Chapron, B., Mouche, A., Stopa, J.E., 2019. A new ocean sar cross-spectral parameter: Definition and directional property using the global sentinel-1 measurements. Journal of Geophysical Research: Oceans 124, 1566–1577. URL: https://agupubs.onlinelibrary.wiley.com/doi/abs/10.1029/2018JC014638, doi:https://doi.org/10.1029/2018JC014638, arXiv:https://agupubs.onlinelibrary.wiley.com/doi/pdf/10.1029/2018JC014638.

Lin, I., Liu, W.T., Wu, C.C., Wong, G.T.F., Hu, C., Chen, Z., Liang, W.D., Yang, Y., Liu, K.K., 2003. New evidence for enhanced ocean primary production triggered by tropical cyclone. Geophysical Research Letters 30. URL: https://agupubs.onlinelibrary.wiley.com/doi/abs/10.1029/2003GL017141, doi:https://doi.org/10.1029/2003GL017141, arXiv:https://agupubs.onlinelibrary.wiley.com/doi/pdf/10.1029/2003GL017141.

Liu, Q., Wu, L., Qin, N., Li, Y., 2021. Storm-scale and fine-scale boundary layer structures of tropical cyclones simulated with the wrf-les framework. Journal of Geophysical Research: Atmospheres 126, e2021JD035511. URL: https://agupubs.onlinelibrary.wiley.com/doi/abs/10.1029/2021JD035511, doi:https://doi.org/10.1029/2021JD035511, arXiv:https://agupubs.onlinelibrary.wiley.com/doi/pdf/10.1029/2021JD035511. e2021JD035511 2021JD035511.

Lloyd, I.D., Vecchi, G.A., 2011. Observational evidence for oceanic controls on hurricane intensity. Journal of Climate 24, 1138 – 1153. URL: https://journals.ametsoc.org/view/journals/clim/24/4/2010jcli3763.1.xml, doi:10.1175/2010JCLI3763.1.

Longépé, N., Mouche, A.A., Ferro-Famil, L., Husson, R., 2022. Co-cross-polarization coherence over the sea surface from sentinel-1 sar data: Perspectives for mission calibration and wind field retrieval. IEEE Transactions on Geoscience and Remote Sensing 60, 1–16. doi:10.1109/TGRS.2021.3055979.

Looney, L.B., Foltz, G.R., 2025. Drivers of tropical cyclone—induced ocean surface cooling. Journal of Geophysical Research: Oceans 130, e2024JC021610. URL: https://agupubs.onlinelibrary.wiley.com/doi/abs/10.1029/2024JC021610, doi:https://doi.org/10.1029/2024JC021610, arXiv:https://agupubs.onlinelibrary.wiley.com/doi/pdf/10.1029/2024JC021610. e2024JC021610 2024JC021610.

Matak, L., Momen, M., 2023. The role of vertical diffusion parameterizations in the dynamics and accuracy of simulated intensifying hurricanes. Boundary-Layer Meteorology 188, 389–418. URL: https://link.springer.com/10.1007/s10546-023-00818-w, doi:10.1007/s10546-023-00818-w.

Mei, W., Primeau, F., McWilliams, J.C., Pasquero, C., 2013. Sea surface height evidence for long-term warming effects of tropical cyclones on the ocean. Proceedings of the National Academy of Sciences 110, 15207–15210. URL: https://www.pnas.org/doi/abs/10.1073/pnas.1306753110, doi:10.1073/pnas.1306753110, arXiv:https://www.pnas.org/doi/pdf/10.1073/pnas.1306753110.

Mei, W., Xie, S.P., 2016. Intensification of landfalling typhoons over the northwest pacific since the late 1970s. Nature Geosci 9, 753–757. URL: https://doi.org/10.1038/ngeo2792.

Meissner, T., Ricciardulli, L., Wentz, F.J., 2017. Capability of the smap mission to measure ocean surface winds in storms. Bulletin of the American Meteorological Society 98, 1660–1677.

Melsheimer, C., Alpers, W., Gade, M., 1998. Investigation of multifrequency/multipolarization radar signatures of rain cells over the ocean using sir-c/x-sar data. Journal of Geophysical Research: Oceans 103, 18867–18884. URL: https://agupubs.onlinelibrary.

wiley.com/doi/abs/10.1029/98JC00779, doi:https://doi.org/10.1029/98JC00779, arXiv:https://agupubs.onlinelibrary.wiley.com/doi/pdf/10.1029/98JC00779.

Momen, M., Parlange, M.B., Giometto, M.G., 2021. Scrambling and reorientation of classical atmospheric boundary layer turbulence in hurricane winds. Geophysical Research Letters 48, e2020GL091695. URL: https://agupubs.onlinelibrary.wiley.com/doi/abs/10.1029/2020GL091695, doi:https://doi.org/10.1029/2020GL091695, arXiv:https://agupubs.onlinelibrary.wiley.com/doi/pdf/10.1029/2020GL091695. e2020GL091695 2020GL091695.

Morrison, I., Businger, S., Marks, F., Dodge, P.P., Businger, J.A., 2005. An observational case for the prevalence of roll vortices in the hurricane boundary layer. Journal of the Atmospheric Sciences 62, 2662–2673. URL: https://api.semanticscholar.org/CorpusID:18750462.

Mouche, A., Chapron, B., Knaff, J., Zhao, Y., Zhang, B., Combot, C., 2019. Copolarized and cross-polarized sar measurements for high-resolution description of major hurricane wind structures: Application to irma category 5 hurricane. Journal of Geophysical Research: Oceans 124, 3905–3922.

Mouche, A.A., Chapron, B., Zhang, B., Husson, R., 2017. Combined co-and cross-polarized sar measurements under extreme wind conditions. IEEE Transactions on Geoscience and Remote Sensing 55, 6746–6755.

Mouche, A.A., Collard, F., Chapron, B., Dagestad, K.F., Guitton, G., Johannessen, J.A., Kerbaol, V., Hansen, M.W., 2012. On the use of doppler shift for sea surface wind retrieval from sar. IEEE Transactions on Geoscience and Remote Sensing 50, 2901–2909. doi:10.1109/TGRS.2011.2174998.

Mueller, K.J., DeMaria, M., Knaff, J., Kossin, J.P., Haar, T.H.V., 2006. Objective estimation of tropical cyclone wind structure from infrared satellite data. Weather and forecasting 21, 990–1005.

Ni, W., Stoffelen, A., Ren, K., Vogelzang, J., Zhao, Y., Yang, X., Wang, W., 2025. Enhanced tropical cyclone ascat winds guided by sar-learned spatial structure functions. IEEE Transactions on Geoscience and Remote Sensing 63, 1–19. doi:10.1109/TGRS.2024.3516209.

Nonaka, K., S.N., Igarashi, Y., 2019. Utilization of Estimated Sea Surface Wind Data Based on Himawari-8/9 Low-level AMVs for Tropical Cyclone Analysis. Technical Report. RSMC Tokyo Typhoon Center Technical Review. URL: https://www.jma.go.jp/jma/jma-eng/jma-center/rsmc-hp-pub-eg/techrev/text21-3.pdf.

Olander, T.L., Velden, C.S., 2007. The Advanced Dvorak Technique: Continued Development of an Objective Scheme to Estimate Tropical Cyclone Intensity Using Geostationary Infrared Satellite Imagery. Weather and Forecasting 22, 287–298. URL: http://journals.ametsoc.org/doi/abs/10.1175/WAF975.1, doi:10.1175/WAF975.1.

Olfateh, M., Callaghan, D.P., Nielsen, P., Baldock, T.E., 2017. Tropical cyclone wind field asymmetry—development and evaluation of a new parametric model. Journal of Geophysical Research: Oceans 122, 458–469.

O'Driscoll, O., Mouche, A., Chapron, B., Kleinherenbrink, M., López-Dekker, P., 2023. Obukhov length estimation from spaceborne radars. Geophysical Research Letters 50, e2023GL104228. URL: https://agupubs.onlinelibrary.wiley.com/doi/abs/10.1029/2023GL104228, doi:https://doi.org/10.1029/2023GL104228, arXiv:https://agupubs.onlinelibrary.wiley.com/doi/pdf/10.1029/2023GL104228. e2023GL104228 2023GL104228.

Patoux, J., Brown, R.A., 2002. A gradient wind correction for surface pressure fields retrieved from scatterometer winds. Journal of Applied Meteorology 41, 133 – 143. URL: https://journals.ametsoc.org/view/journals/apme/41/2/1520-0450_2002_041_0133_agwcfs_2.0.co_2.xml, doi:10.1175/1520-0450(2002)041<0133:AGWCFS>2.0.CO;2.

Patoux, J., Foster, R.C., Brown, R.A., 2003. Global pressure fields from scatterometer winds. Journal of Applied Meteorology 42, 813–826. URL: http://journals.ametsoc.org/doi/10.1175/1520-0450(2003)042<0813:GPFFSW>2.0.CO;2, doi:10.1175/1520-0450(2003)042<0813:GPFFSW>2.0.CO;2.

Pivaev, P., Kudryavtsev, V., Reul, N., Chapron, B., 2022. Upper ocean response to tropical cyclones from observations and modelling, in: IGARSS 2022 - 2022 IEEE International Geoscience and Remote Sensing Symposium, pp. 6899–6902. doi:10.1109/IGARSS46834.2022.9884843.

Pleskachevsky, A., Tings, B., Wiehle, S., Imber, J., Jacobsen, S., 2022. Multiparametric sea state fields from synthetic aperture radar for maritime situational awareness. Remote Sensing of Environment 280, 113200. URL: https://www.sciencedirect.com/science/article/pii/S0034425722003108, doi:https://doi.org/10.1016/j.rse.2022.113200.

Pouplin, C., Mouche, A., Chapron, B., 2024. A multi-sensor approach for the characterization of tropical cyclone induced swell—application to tc larry, 2021. Geophysical Research Letters 51, e2024GL109712. URL: https://agupubs.onlinelibrary.wiley.com/doi/abs/10.1029/2024GL109712, doi:https://doi.org/10.1029/2024GL109712, arXiv:https://agupubs.onlinelibrary.wiley.com/doi/pdf/10.1029/2024GL109712. e2024GL109712 2024GL109712.

Price, J.F., 1981. Upper Ocean Response to a Hurricane. Journal of Physical Oceanography 11, 153–175. URL: https://doi.org/10.1175/1520-0485(1981)011<0153:UORTAH>2.0.CO;2, doi:10.1175/1520-0485(1981)011<0153:UORTAH>2.0.CO;2.

Pun, I.F., Chang, Y.T., Lin, I.I., Tang, T.Y., Lien, R.C., 2011. Typhoon-ocean interaction in the western north pacific: Part 2. Oceanography 24, 32–41. URL: https://doi.org/10.5670/oceanog.2011.92.

Quach, B., Glaser, Y., Stopa, J.E., Mouche, A.A., Sadowski, P., 2021. Deep learning for predicting significant wave height from synthetic aperture radar. IEEE Transactions on Geoscience and Remote Sensing 59, 1859–1867. doi:10.1109/TGRS.2020.3003839.

Rappaport, E.N., Franklin, J.L., Avila, L.A., Baig, S.R., Beven, J.L., Blake, E.S., Burr, C.A., Jiing, J.G., Juckins, C.A., Knabb, R.D., Landsea, C.W., Mainelli, M., Mayfield, M., McAdie, C.J., Pasch, R.J., Sisko, C., Stewart, S.R., Tribble, A.N., 2009. Advances and Challenges at the National Hurricane Center. Weather and Forecasting 24, 395–419. URL: http://journals.ametsoc.org/doi/abs/10.1175/2008WAF2222128.1, doi:10.1175/2008WAF2222128.1.

Reul, N., Chapron, B., Grodsky, S.A., Guimbard, S., Kudryavtsev, V., Foltz, G.R., Balaguru, K., 2021. Satellite observations of the sea surface salinity response to tropical cyclones. Geophysical Research Letters 48, e2020GL091478. URL: https://agupubs.onlinelibrary.wiley.com/doi/abs/10.1029/2020GL091478, doi:https://doi.org/10.1029/2020GL091478, arXiv:https://agupubs.onlinelibrary.wiley.com/doi/pdf/10.1029/2020GL091478. e2020GL091478 2020GL091478.

Reul, N., Chapron, B., Zabolotskikh, E., Donlon, C., Mouche, A., Tenerelli, J., Collard, F., Piolle, J.F., Fore, A., Yueh, S., et al., 2017. A new generation of tropical cyclone size measurements from space. Bulletin of the American Meteorological Society 98, 2367–2385.

Reul, N., Quilfen, Y., Chapron, B., Fournier, S., Kudryavtsev, V., Sabia, R., 2014. Multisensor observations of the amazon-orinoco river plume interactions with hurricanes. Journal of Geophysical Research: Oceans 119, 8271–8295. URL: https://agupubs.onlinelibrary.wiley.com/doi/abs/10.1002/2014JC010107, doi:https://doi.org/10.1002/2014JC010107, arXiv:https://agupubs.onlinelibrary.wiley.com/doi/pdf/10.1002/2014JC010107.

Riehl, H., 1963. Some relations between wind and thermal structure of steady state hurricanes. Journal of Atmospheric Sciences 20, 276–287.

Sampson, C.R., Fukada, E.M., Knaff, J.A., Strahl, B.R., Brennan, M.J., Marchok, T., 2017. Tropical Cyclone Gale Wind Radii Estimates for the Western North Pacific. Weather and Forecasting 32, 1029–1040. URL: http://journals.ametsoc.org/doi/10.1175/WAF-D-16-0196.1, doi:10.1175/WAF-D-16-0196.1.

Sampson, C.R., Goerss, J.S., Knaff, J.A., Strahl, B.R., Fukada, E.M., Serra, E.A., 2018. Tropical Cyclone Gale Wind Radii Estimates, Forecasts, and Error Forecasts for the Western North Pacific. Weather and Forecasting 33, 1081–1092. URL: http://journals.ametsoc.org/doi/10.1175/WAF-D-17-0153.1, doi:10.1175/WAF-D-17-0153.1.

Sampson, C.R., Schrader, A.J., 2000. The automated tropical cyclone forecasting system (version 3.2). Bulletin of the American Meteorological Society 81, 1231–1240.

Sapp, J., 2025. Iwrap 3d winds in hurricane larry (20210907) derived from the ku-band radars. URL: https://dx.doi.org/10.21227/7m27-t235, doi:10.21227/7m27-t235.

Sapp, J., Alsweiss, S., Jelenak, Z., Chang, P., Carswell, J., 2019. Stepped Frequency Microwave Radiometer Wind-Speed Retrieval Improvements. Remote Sensing 11, 214. URL: http://www.mdpi.com/2072-4292/11/3/214, doi:10.3390/rs11030214.

Sapp, J., Jelenak, Z., Chang, P., Shoup, C., Carswell, J., 2022. Processing of high-resolution hurricane ida boundary layer winds from the iwrap instrument on the noaa wp-3d aircraft, in: IGARSS 2022-2022 IEEE International Geoscience and Remote Sensing Symposium, IEEE. pp. 7286–7289.

Schmit, T.J., Griffith, P., Gunshor, M.M., Daniels, J.M., Goodman, S.J., Lebair, W.J., 2017. A closer look at the abi on the goes-r series. Bulletin of the American Meteorological Society 98, 681 – 698. URL: https://journals.ametsoc.org/view/journals/bams/98/4/bams-d-15-00230.1.xml, doi:10.1175/BAMS-D-15-00230.1.

Schulz-Stellenfleth, J., König, T., Lehner, S., 2007. An empirical approach for the retrieval of integral ocean wave parameters from synthetic aperture radar data. Journal of Geophysical Research: Oceans 112, 1–14. URL: https://agupubs.onlinelibrary.wiley.com/doi/abs/10.1029/2006JC003970, doi:10.1029/2006JC003970, arXiv:https://agupubs.onlinelibrary.wiley.com/doi/pdf/10.1029/2006JC003970.

Shay, L., 2009. Upper ocean structure: Responses to strong atmospheric forcing events, in: Steele, J.H. (Ed.), Encyclopedia of Ocean Sciences (Second Edition). second edition ed.. Academic Press, Oxford, pp. 192–210. URL: https://www.sciencedirect.com/science/article/pii/B9780123744739006287, doi:https://doi.org/10.1016/B978-012374473-9.00628-7.

Shimada, U., 2024a. Estimation of the radius of maximum wind using passive microwave satellite data, in: The Second International Workshop on Typhoon Science and Technology Research Center, Yokohama, Japan, Yokohama National University. URL: https://www.dropbox.com/scl/fo/pcxrzzx5k6i8ezbmt3zwd/AGU34p8u_0rp3JYO8vfdNi4?rlkey=dnmiimngt47qoah4hno1ptf6y&e=2&st=88kz0wgx&dl=0.

Shimada, U., 2024b. Estimation of the radius of maximum wind using passive microwave satellite data. in review, Submitted to Scientific Online Letters on the Atmosphere (SOLA) .

Shimada, U., Hayashi, M., Mouche, A., 2024a. A comparison between sar wind speeds and western north pacific tropical cyclone best track estimates. Journal of the Meteorological Society of Japan. Ser. II 102, 575–593. doi:10.2151/jmsj.2024-031.

Shimada, U., Tadono, T., Ohki, M., Sobue, S., Ikuta, Y., Hayashi, M., Kohno, N., Yanase, W., Tsujino, S., Yamaguchi, M., Isoguchi, O., 2024b. Ocean surface wind retrieval from alos-2/palsar-2 and application studies using synthetic aperture radar (sar) winds, in: ESCAP/WMO Typhoon Committee 19th Integrated Workshop, Shanghai, China. URL: https://www.typhooncommittee.org/19IWS/docs/Technical%20Presentations/2.%2020241120_ALOS2_v1.pdf.

Shutts, G., 1981. Hurricane structure and the zero potential vorticity approximation. Monthly Weather Review 109, 324–329.

Snodgrass, F., Hasselmann, K., Miller, G., Munk, W.H., Powers, W., 1966. Propagation of ocean swell across the pacific. Philosophical Transactions of the Royal Society of London. Series A, Mathematical and Physical Sciences 259, 431–497.

Stoffelen, A., Anderson, D., 1997. Scatterometer data interpretation: Measurement space and inversion. Journal of Atmospheric and Oceanic Technology 14, 1298 – 1313. URL: https://journals.ametsoc.org/view/journals/atot/14/6/1520-0426_1997_014_1298_sdimsa_2_0_co_2.xml, doi:10.1175/1520-0426(1997)014<1298:SDIMSA>2.0.CO;2.

Stopa, J.E., Mouche, A., 2017. Significant wave heights from sentinel-1 sar: Validation and applications. Journal of Geophysical Research: Oceans 122, 1827–1848. URL: https://agupubs.onlinelibrary.wiley.com/doi/abs/10.1002/2016JC012364, doi:10.1002/2016JC012364, arXiv:https://agupubs.onlinelibrary.wiley.com/doi/pdf/10.1002/2016JC012364.

Stopa, J.E., Wang, C., Vandemark, D., Foster, R., Mouche, A., Chapron, B., 2022. Automated global classification of surface layer stratification using high-resolution sea surface roughness measurements by satellite synthetic aperture radar. Geophysical Research Letters 49, e2022GL098686. URL: https://agupubs.onlinelibrary.wiley.com/doi/abs/10.1029/2022GL098686, doi:https://doi.org/10.1029/2022GL098686, arXiv:https://agupubs.onlinelibrary.wiley.com/doi/pdf/10.1029/2022GL098686. e2022GL098686 2022GL098686.

Sun, J., Vecchi, G., Soden, B., 2021. Sea surface salinity response to tropical cyclones based on satellite observations. Remote Sensing 13. URL: https://www.mdpi.com/2072-4292/13/3/420, doi:10.3390/rs13030420.

Tannehill, I., 1937. Sea swells in relation to the movement and intensity of tropical storms. The International Hydrographic Review .

Torres, R., Snoeij, P., Geudtner, D., Bibby, D., Davidson, M., Attema, E., Potin, P., Rommen, B., Floury, N., Brown, M., Traver, I.N., Deghaye, P., Duesmann, B., Rosich, B., Miranda, N., Bruno, C., L'Abbate, M., Croci, R., Pietropaolo, A., Huchler, M., Rostan, F.,

2012. GMES Sentinel-1 mission. Remote Sensing of Environment 120, 9–24. URL: https://linkinghub.elsevier.com/retrieve/pii/S0034425712000600, doi:10.1016/j.rse.2011.05.028. iSBN: 0034-4257.

Tsukada, T., Horinouchi, T., 2023. Strong relationship between eye radius and radius of maximum wind of tropical cyclones. Monthly Weather Review 151, 569–588.

Tsukada, T., Horinouchi, T., Tsujino, S., 2024. Wind distribution in the eye of tropical cyclone revealed by a novel atmospheric motion vector derivation. Journal of Geophysical Research: Atmospheres 129, e2023JD040585. URL: https://agupubs.onlinelibrary.wiley.com/doi/abs/10.1029/2023JD040585, doi:https://doi.org/10.1029/2023JD040585, arXiv:https://agupubs.onlinelibrary.wiley.com/doi/pdf/10.1029/2023JD040585. e2023JD040585 2023JD040585.

Vachon, P.W., Katsaros, K., Black, P., Dodge, P., 1999. Radarsat synthetic aperture radar measurements of some 1998 hurricanes, in: IEEE 1999 International Geoscience and Remote Sensing Symposium. IGARSS'99 (Cat. No. 99CH36293), IEEE. pp. 1631–1633.

Vachon, P.W., Wolfe, J., 2011. C-Band Cross-Polarization Wind Speed Retrieval. IEEE Geoscience and Remote Sensing Letters 8, 456–459. URL: http://ieeexplore.ieee.org/document/5638769/, doi:10.1109/LGRS.2010.2085417.

Velden, C., Herndon, D., 2020. A Consensus Approach for Estimating Tropical Cyclone Intensity from Meteorological Satellites: SATCON. Weather and Forecasting URL: https://doi.org/10.1175/WAF-D-20-0015.1, doi:10.1175/WAF-D-20-0015.1.

Velden, C.S., Olander, T.L., Zehr, R.M., 1998. Development of an objective scheme to estimate tropical cyclone intensity from digital geostationary satellite infrared imagery. Weather and Forecasting 13, 172–186.

Vincent, E.M., Lengaigne, M., Madec, G., Vialard, J., Samson, G., Jourdain, N.C., Menkes, C.E., Jullien, S., 2012. Processes setting the characteristics of sea surface cooling induced by tropical cyclones. Journal of Geophysical Research: Oceans 117, n/a–n/a. URL: http://doi.wiley.com/10.1029/2011JC007396, doi:10.1029/2011JC007396.

Vinour, L., Jullien, S., Mouche, A., Combot, C., Mangeas, M., 2021. Observations of tropical cyclone inner-core fine-scale structure, and its link to intensity variations. Journal Of The Atmospheric Sciences 78, 3651–3671. URL: https://doi.org/10.1175/JAS-D-20-0245.1, doi:10.1175/JAS-D-20-0245.1.

Walker, N.D., Leben, R.R., Pilley, C.T., Shannon, M., Herndon, D.C., Pun, I.F., Lin, I.I., Gentemann, C.L., 2014. Slow translation speed causes rapid collapse of northeast pacific hurricane kenneth over cold core eddy. Geophysical Research Letters 41, 7595–7601. URL: https://agupubs.onlinelibrary.wiley.com/doi/abs/10.1002/2014GL061584, doi:https://doi.org/10.1002/2014GL061584, arXiv:https://agupubs.onlinelibrary.wiley.com/doi/pdf/10.1002/2014GL061584.

Wang, S., Yang, X., Li, H., Ren, K., Yin, X., Hu, D., Du, Y., 2021. An improved asymmetric hurricane parametric model based on cross-polarization sar observations. IEEE Journal of Selected Topics in Applied Earth Observations and Remote Sensing 14, 1411–1422. doi:10.1109/JSTARS.2020.3043246.

Willoughby, H.E., Darling, R., Rahn, M., 2006. Parametric representation of the primary hurricane vortex. part ii: A new family of sectionally continuous profiles. Monthly weather review 134, 1102–1120.

Young, I.R., 1988. Parametric hurricane wave prediction model. Journal of Waterway, Port, Coastal, and Ocean Engineering 114, 637–652.

Yurchak, B.S., 2007. Description of cloud-rain bands in a tropical cyclone by a hyperbolic-logarithmic spiral. Russian Meteorology and Hydrology 32, 8–18.

Yurchak, B.S., 2024. Estimating the intensity of tropical cyclones from spiral signatures acquired by spaceborne sar. Remote Sensing 16. URL: https://www.mdpi.com/2072-4292/16/10/1750, doi:10.3390/rs16101750.

Yurovskaya, M., Kudryavtsev, V., Chapron, B., 2023. A self-similar description of the wave fields generated by tropical cyclones. Ocean Modelling 183, 102184.

Yurovsky, Y.Y., Kudryavtsev, V.N., Yurovskaya, M.V., Pivaev, P.D., Grodsky, S.A., 2024. Tropical cyclone signatures in sar ocean radial doppler velocity. Remote Sensing of Environment 311, 114251. URL: https://www.sciencedirect.com/science/article/pii/S0034425724002694, doi:https://doi.org/10.1016/j.rse.2024.114251.

Zhang, B., Perrie, W., 2012a. Cross-polarized synthetic aperture radar: A new potential measurement technique for hurricanes. Bulletin of the American Meteorological Society 93, 531–541.

Zhang, B., Perrie, W., 2012b. Cross-Polarized Synthetic Aperture Radar: A New Potential Measurement Technique for Hurricanes. Bulletin of the American Meteorological Society 93, 531–541. URL: http://journals.ametsoc.org/doi/abs/10.1175/BAMS-D-11-00001.1, doi:10.1175/BAMS-D-11-00001.1.

Zhang, B., Perrie, W., Vachon, P.W., Li, X., Pichel, W.G., Guo, J., He, Y., 2012. Ocean Vector Winds Retrieval From C-Band Fully Polarimetric SAR Measurements. IEEE Transactions on Geoscience and Remote Sensing 50, 4252–4261. URL: http://ieeexplore.ieee.org/document/6204086/, doi:10.1109/TGRS.2012.2194157.

Zhang, B., Wen, L., Perrie, W., Kudryavtsev, V., 2024. Sea surface height response to tropical cyclone from satellite altimeter observations and sar estimates. IEEE Transactions on Geoscience and Remote Sensing 62, 1–9. doi:10.1109/TGRS.2024.3371168.

Zhang, G., Zhang, B., Perrie, W., Xu, Q., He, Y., 2014. A hurricane tangential wind profile estimation method for c-band cross-polarization sar. IEEE Transactions on Geoscience and Remote Sensing 52, 7186–7194. doi:10.1109/TGRS.2014.2308839.

Zhang, J.A., Katsaros, K.B., Black, P.G., Lehner, S., French, J.R., Drennan, W.M., 2008. Effects of roll vortices on turbulent fluxes in the hurricane boundary layer. Boundary-Layer Meteorology 128, 173–189. URL: http://link.springer.com/10.1007/s10546-008-9281-2, doi:10.1007/s10546-008-9281-2.

Zhang, J.A., Uhlhorn, E.W., 2012. Hurricane sea surface inflow angle and an observation-based parametric model. Monthly Weather Review 140, 3587–3605.

Zhao, Y., Longépé, N., Mouche, A., Husson, R., 2021. Automated rain detection by dual-polarization sentinel-1 data. Remote Sensing 13, 3155 (19p.). URL: https://doi.org/10.3390/rs13163155, doi:10.3390/rs13163155.

Zhao, Y., Mouche, A.A., Chapron, B., Reul, N., 2018. Direct comparison between active c-band radar and passive l-band radiometer measurements: Extreme event cases. IEEE Geoscience and Remote Sensing Letters 15, 897–901. URL: https://ieeexplore.ieee.org/document/8351914/, doi:10.1109/LGRS.2018.2811712.

Zheng, G., Jiang, H., Wu, L., Li, X., Zhou, L., Wu, Q., Chen, P., Ren, L., 2024. Rainband-occurrence probability in northern hemisphere tropical cyclones by synthetic aperture radar imagery. Geophysical Research Letters 51, e2023GL107555. URL: https://agupubs.onlinelibrary.wiley.com/doi/abs/10.1029/2023GL107555, doi:https://doi.org/10.1029/2023GL107555, arXiv:https://agupubs.onlinelibrary.wiley.com/doi/pdf/10.1029/2023GL107555. e2023GL107555 2023GL107555.